Chemical modeling of methanol as an extragalactic shock tracer

Eva Juliana Méndez Robayo

Universidad Nacional de Colombia
Observatorio Astronómico Nacional
Bogotá DC, Colombia
2024

Modelamiento químico del metanol como trazador de choques extragalácticos

Eva Juliana Méndez Robayo

Universidad Nacional de Colombia
Observatorio Astronómico Nacional
Bogotá DC, Colombia
2024

Master's Thesis

Observatorio Astrónomico Nacional
Facultad de Ciencias
Universidad Nacional de Colombia

Chemical modeling of methanol as an extragalactic shock tracer

Thesis by:
Eva Juliana Méndez Robayo

Thesis presented as a partial requirement to qualify for the title of:
MSc-Astronomy

Chemical modeling of methanol as an extragalactic shock tracer

Eva Juliana Méndez Robayo

Director:
Prof. Mario Armando Higuera Garzón
Observatorio Astrónomico Nacional, Universidad Nacional de Colombia

Scientific advisor & Principal investigator:
Prof. Serena Viti
Leiden Observatory, Universiteit Leiden
Department of Physics and Astronomy, University College London

Co-director:
Dr. Ko-Yun Huang
Leiden Observatory, Universiteit Leiden

Major Subject:
Astrochemistry and Active Galactic Nuclei
Research Group:
Molecular Astrophysics Group - Universiteit Leiden and University College London
Grupo SAGAN - Universidad Nacional de Colombia

Universidad Nacional de Colombia
Observatorio Astronómico Nacional
Bogotá DC, Colombia
2024

A mis padres y sobrinos, con amor.

«The nitrogen in our DNA, the calcium in our teeth, the iron in our blood, the carbon in our apple pies were made in the interiors of collapsing stars. We are made of starstuff.»

Carl Sagan.

Acknowledgments

Above all, I thank God and my family. To my beloved parents because what I am is a reflection of them. To my brothers and beautiful nieces and nephews for their constant support and motivation. Thank you for filling my path with light, wisdom, and love.

I express my gratitude to Professor Mario Armando Higuera for his listening, words, and advice. For accompanying me from my undergraduate studies in Chemistry to build a professional path and to promote Astrochemistry in Colombia. For motivating me to face challenges with determination.

My deepest thanks to Dr. Ko-Yun Huang for believing in me and giving me the opportunity to progress on the path of research in Astronomy. For being the cornerstone in LEAPS and, above all, in this work.

I also thank Professor Serena Viti for her availability and knowledge. For helping me unveil the questions that initially made me want to study Astrochemistry.

I would like to express my sincere gratitude to all the professors at the Observatory. To Professor Giovanny Pinzón for trusting me and encouraging me to dream big. Without his support, this work would not exist. To Professor Eduard Larrañaga for his valuable contribution to optimize the analysis. To Professor José Gregorio Portilla because his courses planted seeds in me that instilled my passion for Astronomy. Thanks to them, to Professor Benjamín Calvo, and everyone else for providing constructive feedback and strengthening the progress of this project.

With immense affection, I wish to express my gratitude to my friends. To my confidants from undergrad, Laura, Diego, Lina, Paula, Ricardo, and Valeria, who have always brought smiles to my face and carried a piece of my heart in theirs. To my master's degree colleagues, Camilo, Sebastián, Jonhatan, Yul, and all my admirable fellows for coloring this journey with indelible memories. Also, I extend my thanks to Islena, whose extraordinary patience and help have transformed the Observatory.

Finally, I thank the SAGAN research group at Observatorio Astronómico Nacional de Colombia and the Molecular Astrophysics group at Leiden University for their questions, corrections, and suggestions, which have helped me grow as a person and researcher.

Agradecimientos

Ante todo agradezco a Dios y a mi familia. A mis padres porque lo que soy se debe a ellos. A mis hermanos y hermosos sobrinos por su constante apoyo y motivación. Gracias por llenar mi camino de luz, sabiduria y amor.

Agradezco al profesor Mario Armando Higuera por su escucha, palabras y consejos. Por acompañarme desde el pregrado en Química a construir un camino profesional y a impulsar la Astroquímica en Colombia. Por motivarme a enfrentar desafíos con determinación.

Mi más sincero agradecimiento a la doctora Ko-Yun Huang por creer en mi y darme la oportunidad de progresar en el camino de la investigación en Astronomia. Por ser la piedra angular en LEAPS y, sobre todo, en este trabajo.

Doy las gracias también a la profesora Serena Viti por su disposición y conocimiento. Por ayudarme a desvelar las preguntas que me hicieron en un comienzo querer estudiar Astroquímica.

Quisiera expresar mi más sincera gratitud a todos los profesores del Observatorio. Al profesor Giovanny Pinzón por confiar en mi e impulsarme a soñar en grande. Sin su apoyo este trabajo no existiría. Al profesor Eduard Larrañaga por su valiosa aportación para optimizar el análisis. Al profesor José Gregorio Portilla porque sus clases sembraron en mi simillitas que infundaron mi pasión por la Astronomía. Gracias a ellos, al profesor Benjamín Calvo, y a todos los demás por brindar comentarios constructivos y fortalecer el avance de este proyecto.

Con inmenso cariño, deseo expresar mi gratitud a mis amigos. A mis confidentes del pregrado, Laura, Diego, Lina, Paula, Ricardo y Valeria, quienes siempre han arrancado sonrisas de mi rostro y llevado un pedacito de mi corazón en el de ellos. A mis compañeros de la maestría, Camilo, Sebastián, Jonhatan, Yul, y todos mis admirables colegas, por colorear esta travesía con recuerdos imborrables. También, extiendo mi agradecimiento a Islena, cuya extraordinaria paciencia y ayuda han transformado al Observatorio.

Finalmente, agradezco al semillero SAGAN del Observatorio Astronómico Nacional de Colombia y al grupo de Astrofisica Molecular de Universiteit Leiden por sus preguntas, correcciones y sugerencias, las cuales me han ayudado a mejorar como persona e investigadora.

Abstract

Chemical modeling of methanol as an extragalactic shock tracer

The behavior of methanol (CH_3OH) in the composite galaxy NGC 1068 was analyzed to investigate its effectiveness as an extragalactic shock tracer and to study the effect of shock velocity and formation routes on the predicted interstellar abundance of CH_3OH. With a parameterized C-shock physical model, C-shock chemistry was investigated with UCLCHEM to study the chemical abundance of CH_3OH as a function of time in different locations of the Circumnuclear Disc (CND) near the Active Galactic Nuclei (AGN) and the Starburst (SB) ring of NGC 1068. It is concluded that gas-phase methanol can trace C-type shocks as its abundance increases significantly due to ice-dust grain sputtering or sublimation during shock propagation. This increase in the abundance of gaseous methanol is comparable from both low- ($\sim$10 km/s) and high- ($\sim$50 km/s) velocity shocks. Comparing our models with the multi-line molecular observations and analysis performed by Huang *et al.* (submitted) [37], we concluded that the observed CH_3OH abundance may result from C-shock influence or from thermal sublimation of ice due to protostellar core heating, as both models can account for the observed CH_3OH in the gas phase. This work also demonstrated for the first time that the primary reaction leading to the formation of methanol in interstellar ice-dust grains is the radical-molecule H-atom abstraction route under shocked-influenced environments, such as the CND of NGC 1068, from the modeling point of view. This finding is consistent with the results of Simons *et al.* (2020) [78] and Santos *et al.* (2022) [75] in dark molecular clouds. However, its dominance is dependent on the gas kinetic temperature (T_k), gas volume density (n_{H_2}), velocity of the C-shock wave (v_{shock}), and cosmic ray ionisation rate (ζ).

Keywords: Astrochemistry, Molecules, Shock waves, Active Galactic Nuclei, Quantum tunneling.

Resumen

Modelamiento químico de metanol como trazador de choques extragalácticos

Se analizó el comportamiento del metanol (CH_3OH) en la galaxia compuesta NGC 1068 para investigar su eficacia como trazador de choques extragalácticos y estudiar el efecto de la velocidad del choque y las rutas de formación sobre la abundancia interestelar prevista de CH_3OH. Con un modelo físico parametrizado de choque tipo C, se investigó la química del choque con UCLCHEM para estudiar la abundancia química de CH_3OH en función del tiempo en diferentes localizaciones del Disco Circumnuclear (CND) cerca del Núcleo Activo de Galaxia (AGN) y del anillo Starburst (SB) de NGC 1068. Se concluye que el metanol en fase gaseosa puede rastrear choques de tipo C, ya que su abundancia aumenta significativamente debido a la pulverización o sublimación de granos helados durante la propagación del choque. Este aumento en la abundancia de metanol gaseoso es comparable para choques de baja ($\sim$10 km/s) y alta velocidad ($\sim$50 km/s). Comparando nuestros modelos con las observaciones moleculares multilíneares y los análisis realizados por Huang *et al.* (remetido) [37], llegamos a la conclusión de que la abundancia observada de CH_3OH puede deberse a la influencia del choque tipo C o a la sublimación térmica del hielo debido al calentamiento del núcleo protoestelar, ya que ambos modelos pueden explicar la abundancia observada de CH_3OH en fase gaseosa. Este trabajo también mostró por primera vez que la reacción primaria que conduce a la formación de metanol en los granos de polvo interestelar es la vía de abstracción de átomos de H en entornos influenciados por choques, como el CND de NGC 1068, desde el punto de vista del modelamiento. Este hallazgo concuerda con los resultados de Simons *et al.* (2020)[68] y Santos *et al.* (2022)[75] en nubes moleculares oscuras. Sin embargo, su predominio depende de la temperatura cinética del gas (T_k), la densidad volumétrica del gas (n_{H_2}), la velocidad de la onda de choque (v_{shock}) y la tasa de ionización de rayos cósmicos (ζ).

Palabras clave: Astroquímica, Moléculas, Ondas de Choque, Núcleo Activo de Galaxia, Túnelamiento cuántico.

Contents

1. Introduction

The interstellar medium (ISM) is a dynamic environment where physical phenomena massively influence the characteristic chemical signatures of its surroundings [101]. Among these phenomena, shock waves are pressure-driven disturbances that propagate faster than the speed of sound. Shocks are produced by multiple mechanisms, including cloud-cloud collisions, stellar pulsations, supernovae, galactic super-winds, outflows, and winds of young and evolved stars [101]. Chemical reactions and processes that occur under extreme conditions caused by shock waves are referred to as shock-induced chemistry or shock chemistry. Shock chemistry has been used to appropriately understand molecular emission in regions where grain–grain collisions or sputtering (collisional removal) of ices are necessary to explain the observed abundances of molecular species. For instance, shock models have been used to understand the water emission from an outflow in the high-mass star-forming region IRAS 17233-3606 [101, 47, 46, 91].

One of the primary interests of chemical modeling is to find molecules that trace shocks, particularly those sensitive to various shock properties [36]. The above requires well-constrained chemical networks based on accurate experimental data and proper physical models with the ultimate goal of obtaining a proper interpretation. These will be extremely useful in understanding the ISM environment altogether with the observations and both physical and chemical modeling [96, 36]. In this regard, UCLCHEM, a gas-grain chemical code [36], comes in as an essential tool.

UCLCHEM [36] is a gas-grain chemistry code that solves molecular abundances in three-phase material at each time step, based on a pre-defined chemical network and physical setup. For detailed information, please refer to chapter 2.1. UCLCHEM's capabilities are enormous. In fact, one of the useful applications is the identification of molecular tracers for C-type (continuous) shocks. C-shocks are multifluid magnetohydrodynamic shock waves that typically occur in regions with the presence of a magnetic field and a low degree of fractional ionization [101, 40]. The code has been used to explain the observed HCO^+, CO, HCN, CS, HNCO, and SiO abundances in the circumnuclear disk (CND) and starburst ring (SB) of the AGN[a]-SB composite galaxy NGC 1068, with the inclusion of a parameterized C-type shock model (based on Jiménez-Serra *et al.* (2008) [41]) in the chemical modeling of Scourfield *et al.* (2020) [77], Kelly *et al.* (2017) [43], and Viti *et al.* (2014) [93]. In addition, Holdship *et al.* (2017) [36] have provided a detailed description and consequent grouping of chemical species

[a]The term "active galactic nuclei" (AGN) refers to energetic phenomena occurring in the central regions or nuclei of galaxies that cannot be solely attributed to stars [65].

according to their behavior during the propagation of a C-type shock wave. They propose the existence of two types of molecules: Shock-destroyed (NH_3-like, i.e. HNC, HS) and -tracking (H_2O-like, i.e. HCl, HCN) molecules. Both types are enhanced by shock-induced sputtering of ices. However, the former is initially enhanced by the shock but destroyed as the temperature rises, whereas the latter remains abundant throughout the propagation [36]. For the interest of this work, methanol may be a suitable and interesting candidate for shock-tracing. Models from Holdship *et al.* (2017) [36] show that CH_3OH is enhanced by the shock and traces its full extent. However, it exhibit a shock-destroyed behaviour only for a small range of conditions, such as $n_{H_2} = 10^{5-6}\ cm^{-3}$ and v_{shock} = 40-45 km/s. Therefore, CH_3OH might be particularly useful for determining shock properties.

Methanol (CH_3OH), as the simplest alcohol, is a primary aliphatic alcohol consisting of a methyl (CH_3) and an alcohol (OH) group. Under Earth's atmospheric conditions, methanol is a volatile liquid, widely used as a solvent and as an intermediate in chemical synthesis, and a conjugate acid of methoxide CH_3O^- [44, 31]. Methanol's structure (see Figure. **1-1**) is based on an asymmetric top, where the axis of the hydroxy radical (OH) is slightly inclined to the three-fold symmetry axis of the methyl, CH_3, group [21]. This asymmetry produces a torsional motion in which the CH_3 group rotates internally, relative to the OH radical, around the CH_3 symmetry axis [21]. Thus, methanol exists in two nuclear-spin states: A-type and E-type, depending on the net spin of the three protons of the methyl group. In A-type methanol, the proton spins are parallel and the nuclear spin (I) is $\frac{3}{2}$; whereas in the E-type methanol, one of the proton spins is anti-parallel and I = $\frac{1}{2}$ [21]. As a mental image, A-type and E-type methanol are analogous to ortho-NH_3 and para-NH_3 , respectively.

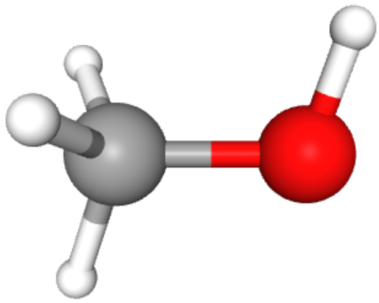

Figure 1-1.: Chemical structure model for CH_3OH as a 3-D conformer. Taken from National Center for Biotechnology Information. (2024).[64]

Gas-phase interstellar methanol, with its large number of observable transitions thanks to its spectroscopic properties, has been frequently detected using sub-millimetre and millimetre ground-based telescopes such as the Atacama Large Millimeter/Submillimeter Array (ALMA), the 30-meter telescope from the Institute for Radio Astronomy in the Millimetre Range (IRAM), the Australia Telescope Compact Array (ATCA), the Atacama Pathfinder Experiment (APEX) telescope, and others [15, 84, 97, 17, 55, 33]. Indeed, CH_3OH is significantly abundant in different astronomical environments, such as hot molecular cores [11], natural satellites [17], protoplanetary disks [97], comets [15], massive YSOs at different sta-

ges of evolution [102], AGN-host galaxies, like NGC 1068 [84, 88, 61, 98]. Its formation is also closely linked to the evolution of molecular clouds [75]. For instance, methanol has been observed with abundances relative to H_2 of 10^{-6}-10^{-7} in hot cores, 10^{-9} in dark clouds, and $< 10^{-9}$ in diffuse molecular clouds [102, 51].

The importance of interstellar methanol and its applications is vast. On one hand, methanol is potentially an important building block of more complex organic molecules (COMs) through surface and gas phase reactions [12, 22], such as CH_2OH radical, CH_3O radical, CH_3CH_2OH (ethanol), CH_3OCH_3 (dimethyl ether), CH_3CHO (methyl formate), $(CH_2OH)_2$ (ethylene glycol) and other species [101]. Mathew *et al.* (2022) [54] discussed how methanol, through its chemical transformation, could be the starting material for olefins, carbonyl compounds, amines, amino acids, peptides, polypeptide chains and complex life molecules such as RNA. On the other hand, methanol might allows us to determine or estimate various physicochemical conditions of its environment, for example: the temperature structure of hot cores [101], virial masses and column densities in warm molecular cores (WMCs), hot molecular cores, and ultra-compact HII regions [33].

1.1. Methanol formation & destruction routes

The formation of interstellar methanol is fascinating and involves a vast network of interrelated reactions. Among these, the two formation pathways of most interest are the pure gas phase and the solid state schemes.

1.1.1. Gas state

In the gas phase, protonated methanol ($CH_3OH_2^+$) can be produced by the radiative association reaction, which is primarily activated by cosmic rays or stellar radiation (Rxn. (1-1)) [101, 52].

$$CH_3^+ + H_2O \longrightarrow [CH_3OH_2^+]^* \longrightarrow CH_3OH_2^+ + h\nu, \tag{1-1}$$

In this radiative association reaction, the protonated methanol is formed in a highly exothermic reaction, $\Delta H = -2.9$ eV [52], where the collision complex, $[CH_3OH_2^+]^*$ [b], is formed in

[b] The transition state is denoted by the symbol $*$. The configuration of the molecules involved in a collision at the saddle point, which is the highest point along the path of minimum energy, is referred to as the transition state [48]. The potential-energy difference, excluding zero-point vibrational energy, between the transition state and the reactants (i.e.,CH_3^+ and H_2O) defines the classical barrier height [48].

an energetic excited state [52] and then stabilized by emitting a photon. This type of reaction typically proceeds at a relatively slow pace due to its low rate coefficients, making it less competitive compared to other ionic processes in interstellar environments. Meanwhile, Geppert *et al.* (2006) [27] argue that in more complicated systems, the radiative lifetime of the excited complex can be of the same order of magnitude as the dissociative lifetime [27], which means that the time it takes for the excited complex to fall apart (dissociative lifetime) is comparable to the time it spends in the excited state (radiative lifetime). Therefore, both processes are significant and may compete in determining the stability of the excited complex. This, in turn, affects the overall production of protonated methanol.

The protonated methanol then dissociatively recombines with electrons to form methanol (Rxn. (1-2)) [101, 27, 104]:

$$CH_3OH_2^+ + e \longrightarrow [CH_3OH_2]^* \longrightarrow CH_3OH + H. \tag{1-2}$$

Dissociative recombination reactions are characterized by the fact that an electron is first captured by the molecular ion ($CH_3OH_2^+$) to form a neutral molecule in its high electronic state ($[CH_3OH_2]^*$)[104]. If this neutral state is repulsive, i.e. the internal forces within the neutral molecule cause the component parts to repel each other, the molecule dissociates into fragments, in this case into CH_3OH and H [104]. This last reaction, at $\Delta H = -5.7$eV [27], is one of the few dissociative recombination pathways possible in the ISM due to the low kinetic energies prevailing there. This favors only exoergic (occurring with the release of energy) or very weak endoergic (occurring with the absorption of energy) reactions [27].

Numerous articles, however, had established that the dissociative recombination step cannot be efficient enough for a pure gas phase route to alone explain the observed CH_3OH abundances [102, 28]. In fact, Geppert *et al.* (2006) [27] concluded that interstellar methanol formation only through radiative association of CH_3^+ and H_2O followed by $CH_3OH_2^+$ dissociative recombination is highly unlikely.

1.1.2. Solid state

On the other hand, the processing of interstellar ices provides viable formation routes for more complex molecular species such as CH_3OH [101]. For instance, in dense and cold regions of molecular clouds, CO molecules present in the gas phase freeze out and form an apolar coating on top of icy-dusty grains [13, 14, 50, 75]. Then, methanol can be efficiently formed through the continuous hydrogenation of CO in the solid phase, with formaldehyde (H_2CO) as one of the intermediate products. The CO hydrogenation mechanism is described in reactions (1-3) to (1-6) [87, 12, 35, 99, 100, 22, 102]. In fact, in the solid phase, methanol

has been considered the second most common constituent of ice-type mantles, after H_2O in several sources, including W33A [57, 29].

$$CO + H \longrightarrow HCO, \tag{1-3}$$
$$HCO + H \longrightarrow H_2CO, \tag{1-4}$$
$$H_2CO + H \longrightarrow CH_3O, \tag{1-5}$$
$$CH_3O + H \longrightarrow CH_3OH. \tag{1-6}$$

This scheme taking place on ice is a Langmuir-Hinshelwood (L-H) mechanism, which is a surface-type reaction. When the two reacting species are chemisorbed [c] on the grain surface [6], the adsorbed species collide as they diffuse across the surface due to their mobilities [59, 81, 86]. The adsorbed species collide, react [59], and eventually form new species as the grain surface acts as a solid-state catalyst. The CO hydrogenation mechanism has been regarded as the primary route to producing methanol in dark molecular clouds. In addition, this process has been shown to effectively reproduce methanol abundances observed in translucent clouds, while pure gas phase models fail by four orders of magnitude [89].

Alternatively, recent laboratory results and Monte Carlo simulations suggested the radical-molecule H-atom abstraction route (Rxn. (1-7) [75, 2, 78]), also a L-H mechanism, as a possibly dominating (70-90 %) final step to form CH_3OH in dark molecular clouds, replacing Rxn.(1-6) in the overall CH_3OH formation mechanism [75, 2, 78].

$$CH_3O + H_2CO \longrightarrow CH_3OH + HCO. \tag{1-7}$$

The radical-molecule route is most likely to proceed by quantum tunneling at the typical low temperatures of molecular clouds. Santos *et al.* (2022) [75] described this last reaction as a radical-molecule route involving an abstraction reaction, where a H atom is transferred from H_2CO to an adjacent CH_3O. In contrast, the reaction (1-6) requires that an additional H atom diffuses through the ice and reacts with CH_3O. Finally, Santos *et al.* (2022) [75] also suggest that the total contribution of each pathway (Rxn.(1-6) or Rxn.(1-7)) is determined by the availability of H, CH_3O, and H_2CO in the ice.

It is important to identify other different reactions that can also lead to the formation of interstellar methanol. A clear example is the work of Qasim *et al.* (2018) [68], where they studied the CH_3OH formation in H_2O-rich interstellar ice analogues according to a OH-mediated H-abstraction mechanism in the reaction: $CH_4 + OH$. They found that methanol

[c] In chemical adsorption (or chemisorption), gaseous molecules adhere to the surface of the solid through strong chemical bonds as a chemical reaction occurs [48].

formation is possible through the sequential surface reaction chain: $CH_4 + OH \longrightarrow CH_3 + H_2O$ and $CH_3 + OH \longrightarrow CH_3OH$ at 10-20 K. However, the yield of CH_3OH formation via the $CH_4 + OH$ pathway is significantly lower than that of CO hydrogenation [68].

Regarding the destruction of CH_3OH, Simons *et al.* (2020) [78] present a graphical flux distribution of their network for a standard simulation with $n(CO) = 10.0\ cm^{-3}$, $n(H) = 2.5\ cm^{-3}$, and $T = 10K$. In this plot (see Figure **1-2**), the reactions (1-8) and (1-9)[78] are the only ones highlighted on the surface of interstellar dust grains. This suggests that they have the highest relative frequency and are likely among the most important reactions in their overall destruction pathway.

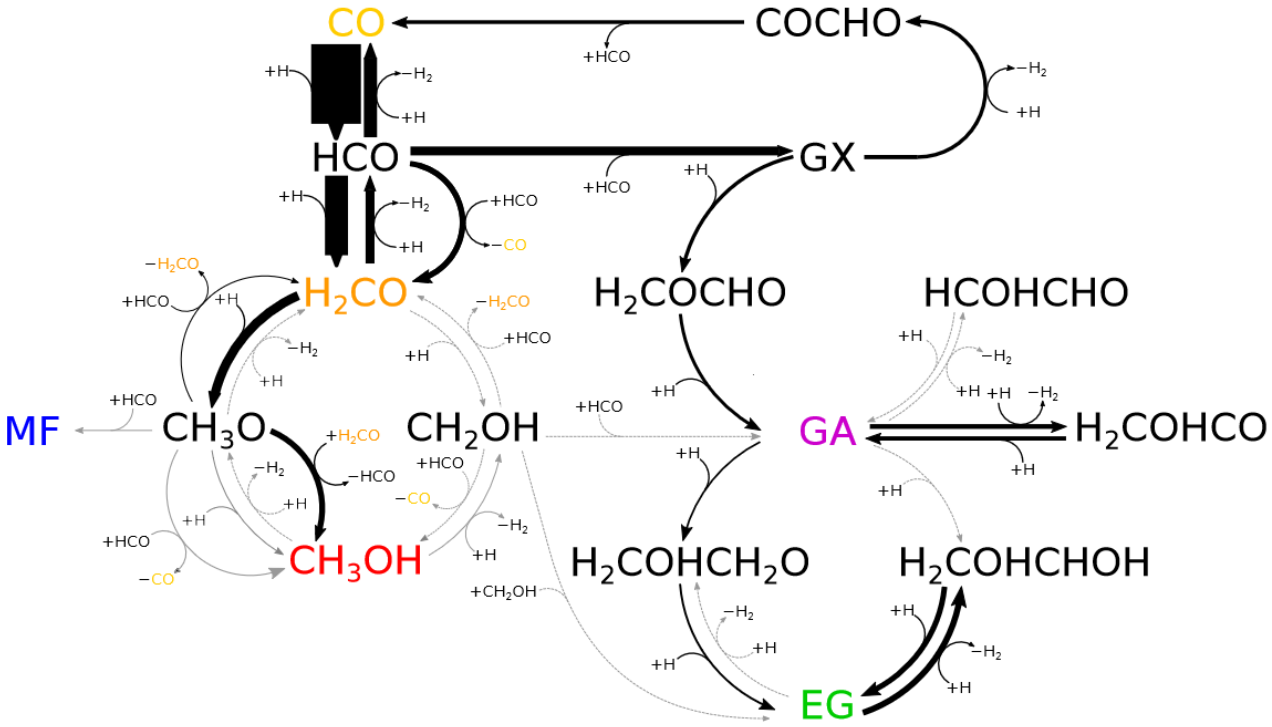

Figure 1-2.: Simons *et al.* (2020) [78] flux distribution network for a standard simulation of $n(CO) = 10.0\ cm^{-3}$, $n(H) = 2.5\ cm^{-3}$, and $T = 10K$. The thickness of the arrows indicates the relative frequency of the reaction. Gray arrows indicate reactions that are too thin. Reactions that contribute less than 0.1 % to the reaction $H + CO \longrightarrow HCO$ are represented with dashed lines. For information regarding acronyms (MF, GX, GA and EG), please consult Simons *et al.* (2020) [78].

$$CH_3OH + H \longrightarrow H_2 + CH_2OH, \tag{1-8}$$
$$CH_3OH + H \longrightarrow H_2 + CH_3O. \tag{1-9}$$

However, under intense UV field conditions, cosmic ray induced photodissociation reactions

of the granular ices are quite relevant, especially reactions (1-10) and (1-11) [26, 92, 32, 71]. As cosmic rays penetrate deeper into an interstellar cloud than ultraviolet photons [32], these reactions become significant in extreme conditions such as the present in Starburst or AGN feedback (jet-ISM interaction) scenarios, which are characterized by high energy.

$$CH_3OH + CRP \longrightarrow H_2 + H_2CO, \quad (1\text{-}10)$$
$$CH_3OH + CRP \longrightarrow OH + CH_3. \quad (1\text{-}11)$$

1.2. Methanol in NGC 1068

NGC 1068 is a nearby Seyfert 2[d] barred galaxy at D$\sim$ 14 Mpc ($H_0 = 75\ km\ s^{-1} Mpc^{-1}$) [7], with a pseudo-bulge overly-massive relative to the central black hole [45, 24]. This galaxy is considered an archetype of a composite AGN-starburst system [38], in which the interstellar medium (ISM) is affected by energetic processes such as cosmic rays, and shocks [77]. Figure **1-3** displays a composite image of NGC 1068 and its black hole-driven outflow, captured by the Hubble Space Telescope.

Interferometric observations of CO, HCO^+, HCN, and CS by Schinnerer *et al.* (2000) [76], García-Burillo *et al.* (2014, 2019), [23, 24], and Sánchez-García *et al.* (2022) [74] have shown that the molecular gas is distributed in three distinct regions: a prominent starburst (SB) ring of $\sim$1.5 kpc radius, an r$\sim$200 pc off-center circumnuclear disk (CND), and a stellar bar region of 2.6 kpc diameter. The SB ring consists of two spiral arms, each subtending an angle of 180°, at a distance of $\sim$ 1 - 1.7 kpc from the galactic centre [77]. Concerning the CND, García-Burillo *et al.* (2014) [24] and Viti *et al.* (2014) [93] found five chemically distinct regions within it: the AGN, the East Knot, the West Knot, and regions north and south of the AGN (CND-N and CND-S) [38]. Figure **1-4** shows the gas distribution in NGC 1068, as depicted in the García-Burillo *et al.* (2014) continuum emission map obtained with ALMA at 349 GHz.

In NGC 1068, molecular gas in the CND was found to be outflowing, which is viewed as a manifestation of the ongoing AGN feedback (jet-ISM interaction) that likely drives different shock chemistry signatures throughout the CND [24, 23, 93, 43, 38]. Viti *et al.* (2014) [93] found that there is a pronounced chemical differentiation across the CND and that each subregion can be characterized by a three-phase ISM component, one of which

[d] A Seyfert galaxy is a specific type of AGN, characterized by the nuclear source emitting visible-wavelength energy comparable to the combined energy emitted by all the stars in the galaxy, around $10^{11} L_\odot$. Type 2 Seyfert galaxies differ from Seyfert 1 galaxies in that only the narrow lines are present in their spectra. The emission lines, known as "narrow lines", are indicative of low-density ($n_e \sim 10^3 - 10^6\ cm^{-3}$) ionized gas. These lines have widths corresponding to velocities of several hundred kilometers per second, slightly broader than emission lines observed in non-AGNs [65].

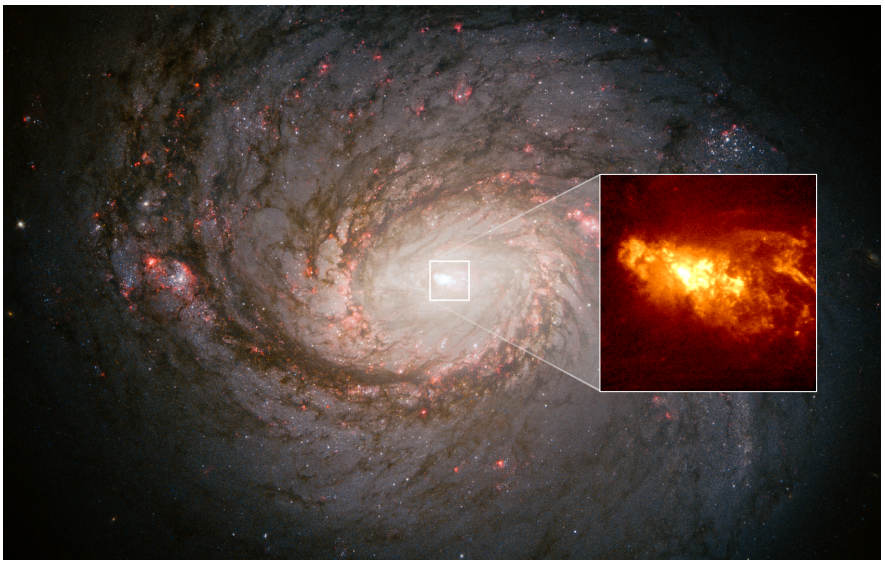

Figure 1-3.: Black-Hole-Driven Outflow From Active Galaxy NGC 1068. This image is a composite of separate exposures acquired by the instruments on the Hubble Space Telescope. Taken from HUBBLESITE [63].

involves shocked gas. Meanwhile, Scourfield *et al.* (2020) [77] suggested that shock chemistry is needed to reproduce the CS observations in the AGN and CND-S subregions, which are characterized via a high fraction of hot gas, possibly due to shock heating, by García-Burillo *et al.* (2014) [24].

Scourfield *et al.* (2020) [77] identified the chemical distinctions in the CND and the SB ring using CS as a dense gas tracer. They coupled chemical modeling using UCLCHEM [36] with the one dimensional non-LTE radiative transfer code RADEX [90]. The results suggest that the temperature and the cosmic ray ionization rate in the CND increase from east to west, and that the overall temperature is higher than in the SB ring. In addition, the AGN is the densest sub-region overall (10^6 cm^{-3}), followed by the CND (10^5 cm^{-3}) and the SB ring (10^4 cm^{-3}).

NGC 1068 is an exceptional laboratory for the study of shock chemistry. Indeed, Huang *et al.* (2022) [38] compared Kelly *et al.* (2017) [43] modeling with ALMA observations in NGC 1068 and described that HNCO and SiO could be suitable molecular shock tracers: HNCO can be sublimated from dust grains and could therefore be a useful tracer of low-velocity shocks (e.g. $v_s \sim$ 20 $km\ s^{-1}$), while SiO is enhanced by grain core sputtering of Si from higher-velocity shocks (e.g. $v_s \sim$ 50 $km\ s^{-1}$). Huang *et al.* (2022) [38] indicated that the cross-species ratio maps of velocity integrated line intensities of SiO and HNCO show a clear spatial differentiation from a high SiO/HNCO ratio in the east of the CND to a low SiO/HNCO ratio in the west of the CND; this is consistent with the trend found in Kelly *et al.* (2017) [43] using low-resolution observations. The eastern node is likely to contain highly shocked gas, while the gas in the western node may not have been heavily shocked or may

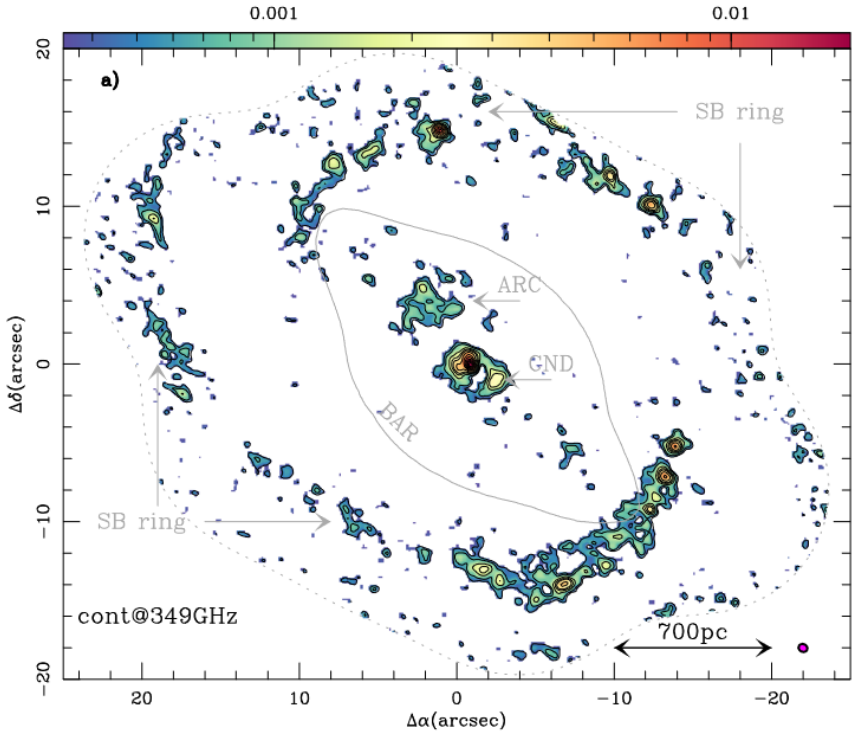

Figure 1-4.: The continuum emission map of NGC 1068 obtained with ALMA at 349 GHz. The map is shown in color scale (in $Jy\,/beam$ units as indicated) with contour levels 3σ, 5σ, 10σ, 15σ, 20σ, 30σ to 120σ in steps of 15σ, where $1\sigma = 0.14$ $mJy\,/beam$. It is highlight the CND, the bar, the bow-shock arc, and the SB ring of NGC 1068. Taken from García-Burillo *et al.* (2014)[24].

have undergone a much milder shock event.

With respect to methanol, Wang *et al.* (2014) [98] reported the detection of CH_3OH mega-masers [e] near the center of NGC 1068 at millimeter wavelengths using the 30-meter IRAM telescope. They proposed that the CH_3OH mega-maser are class I (collisionally pumped) and originate from the shock front region where the nuclear jets or outflows interact with the circumnuclear molecular clouds [98]. In addition, Tosaki *et al.* (2017) [88] showed that the giant molecular clouds (GMCs) with detectable methanol emission in the central $1'$ diameter region of NGC 1068 tend to have larger velocity widths than those with no methanol emission. This trend suggested the presence of shocks, and that shocks could be responsible for the enhancement of the observed $CH_3OH(J_K = 2_K - 1_K)/^{13}CO(J = 1 - 0)$ ratios in the disk of NGC 1068 [88].

In 2018, Nakijama *et al.* (2018) [61] conducted a molecular line survey at 3 mm toward NGC 1068 with the Nobeyama 45-meter telescope, while Qiu *et al.* (2018) [69] used the 30-meter IRAM telescope to make deep millimeter spectroscopic observations toward the

[e]Masers that are $\geq 10^6$ times more luminous than typical galactic maser sources.

center of the galaxy in question. Both works report the detection of CH_3OH, and Nakijama *et al.* (2018) [61] went further and calculated the rotational temperature (T_{rot}) and column density (N_{mol}) for this molecule with the inclusion of their previous work from 2015 [60]. The N_{mol} of CH_3OH was reported to be 1.3 times higher in the CND than in the SB ring, assuming the same T_{rot} in both regions.

Most recent, Huang *et al.* (submitted) [37] and Vroom *et al.* (in prep), via private communication, inferred gas properties (n_{H_2} and T_k) traced by CH_3OH for four regions in the CND and two regions in the SB ring of NGC 1068 using the ALMA observations. Their results suggest a higher density for the CND ($n_{H_2} \sim 10^5 - 10^6\ cm^{-3}$) than for the SB ring ($n_{H_2} \sim 10^3 - 10^4\ cm^{-3}$), which is in agreement with Scourfield *et al.* (2020) [77]. Meanwhile, for the CND T_k is below 50-100 K (poorly constrained) and for the SB ring it is unconstrained.

1.3. The goal of the current study

The present work aims to study the potential of methanol as an extragalactic shock tracer in the SB and AGN-dominated environments in the nearby composite galaxy NGC 1068, using the gas-grain chemical code UCLCHEM v.3.1 (see online documentation) [36]. We aim to address two fundamental questions: 1) Can methanol be used as a tool to trace C-shocks, and does this traceability depend on the shock's velocity or interstellar medium (ISM) conditions? 2) What is the main interstellar methanol formation route under the studied scenarios? Regarding the final question, this study explores for the first time the influence of the radical-molecule H-atom abstraction route in methanol formation under shock-influenced environments, such as NGC 1068, using a proper chemical network in the context of chemical modeling.

The above was done by computing a grid of C-shocks models with UCLCHEM [36] to determine the chemical abundance of CH_3OH as a function of time across the shock influence. We will make a careful comparison with observational results from several sub-regions of the CND and the SB ring of NGC 1068. By comparing both AGN-dominated and SB environments, this work also aspires to understand the shock's origin through molecular emission and whether it is possible to distinguish between them. To achieve the above, it is necessary to analyze the most updated formation pathways for interstellar methanol, to improve the current sputtering models, and to contrast them with recent astronomical observations. In view of the above, this thesis aims to contribute to the field of astrochemistry in extragalactic environments, which is crucial for understanding our origins and studying the physical structure and processes involved in scales from star and planet formation to galaxy evolution [12].

2. Building Chemical Models for NGC 1068

2.1. UCLCHEM: A Time-Dependent Gas-Grain Chemical Code

UCLCHEM [36] is a time-dependent gas-grain chemistry code written in modern Fortran for astrochemical modeling, which can now also be used as a Python module [a]. The code propagates the abundance of chemical species through a network of chemical reactions under different physical conditions [36]. At its core, the code solves the numerical integration of a set of ordinary differential equations (ODEs) associated with the rate of change of chemical species [16]. In other words, it sets up and solves the coupled system of ODEs that provides the fractional abundances, in units of atomic hydrogen number density, of all the species in a parcel of gas [36].

2.1.1. Physics and Chemistry Modules

UCLCHEM comprises of two sets of modules. The chemistry module focus on gas-grain chemistry, including freeze-out, self-shielding of CO and H_2 from UV radiation, thermal and non-thermal desorption, and a user-provided grain-surface-reaction network [36]. Meanwhile, the physics module controls the physical conditions of gas parcels to allow different scenarios to be modeled, such as molecular clouds, hot cores and shocks. The post-processing of hydrodynamic simulation with chemical modeling results is also possible [36].

Chemistry module

In UCLCHEM, gas-phase chemistry include two-body reactions, interactions with cosmic rays, and interactions with UV photons. Of particular interest to us, McElroy *et al.* (2013)

[a] See online documentation for more information.

[56] described the calculation of the reaction rate coefficient of a two-body reaction, as in Eq.(1-1)-(1-2), using the Arrhenius equation (Eq. (2-1)) [36, 56]:

$$R_{AB} = \alpha \left(\frac{T}{300K}\right)^{\beta} exp\left(\frac{-\gamma}{T}\right), \tag{2-1}$$

where α, β, and γ are experimentally determined rate constants [36, 56]. These rates are used to construct and solve a set of ODEs given by Eq. (2-2) [36],

$$\dot{Y}_{product} = R_{AB} Y_A Y_B n_H. \tag{2-2}$$

where Y_A is the abundance of the reactant A, Y_B is the abundance of the reactant B, $\dot{Y}_{product}$ is the rate of change of the product, and n_H is the atomic hydrogen number density [36].

Reactions via diffusion of reactants across the grain surface were added to UCLCHEM by Quénard *et al.* (2018) [70], who derived their formalism from Hasegawa *et al.* (1992) [30], Garrod & Pauly. (2011) [25], and Ruaud *et al.* (2016) [73]. Here, the rate at which two species A and B diffuse and collide at the grain surface is given by Eq. (2-3)[70],

$$k_{AB} = \kappa_{AB} \left(k^A_{hop} + k^B_{hop}\right) \frac{1}{N_{site} n_{dust}}, \tag{2-3}$$

where κ_{AB} is the probability that the reaction between species A and B will occur, k^X_{hop} is the thermal hopping rate of species X on the grain surface, $N_{site} \sim 2 \times 10^6$ [70] is the number of sites on the grain surface, and n_{dust} is the number density of dust grains.

Quénard *et al.* (2018) [70] described the κ_{AB} term as the quantum mechanical probability of tunneling through a rectangular barrier (Eq.(2-4))[70], which can be expressed as Eq.(2-5)[70].

$$\kappa_{AB} = exp\left[-\frac{2a}{\hbar}\sqrt{2\,\mu\,k_B E_A}\right], \tag{2-4}$$

$$\kappa_{AB} = exp\left[-\frac{E_A}{T_{gr}}\right], \tag{2-5}$$

where $\hbar$ is the reduced Planck constant, μ is the reduced mass, k_B is the Boltzmann constant, E_A is the activation energy in K of the reaction, T_{gr} is the grain temperature, and a is the rectangular barrier thickness. See Quénard *et al.* (2018) [70] for a detailed description of the values used for a and the considerations made by UCLCHEM for using Eq.(2-4) or Eq.(2-5) in Eq.(2-3).

The term k_{hop}^X (Eq.(2-6) [30]) defined below follows Hasegawa *et al.* (1992) [30], where t_{hop} is the hopping time between two grain-surface sites [b], E_b is the diffusion energy in K, and ν_0 is the characteristic vibrational frequency of species X.

$$k_{hop}^X = \frac{1}{t_{hop}} = \nu_0 \, exp\left(-\frac{E_b}{T_{gr}}\right), \tag{2-6}$$

Quénard *et al.* (2018) [70] considered two important points: 1) molecules and radicals can form directly at a given surface site and react in situ before moving to an adjacent site; 2) species A and B can also evaporate from the grain surface before reacting or diffusing. Chang *et al.* (2007) [10] and Garrod & Pauly *et al.* (2011) [25] introduced the combination of these effects as a reaction-diffusion competition. Indeed, Chang *et al.* (2007) [10] account for this effect by defining the probabilities of diffusion (Eq. (2-7) [10]), reaction (Eq. (2-8) [10]), and evaporation (Eq. (2-9) [10]) for species A and B.

$$p_{diff} = k_{hop}^A + k_{hop}^B, \tag{2-7}$$

$$p_{reac} = max(\nu_0^A, \nu_0^B) \times \kappa_{AB}, \tag{2-8}$$

$$p_{evap} = \nu_0^A \, exp\left(-\frac{E_D^A}{T_{gr}}\right) + \nu_0^B exp\left(-\frac{E_D^B}{T_{gr}}\right), \tag{2-9}$$

where E_D is the binding energy of the species on to the grain surface and the result of $max(\nu_0^A, \nu_0^B)$ represents the largest value of the characteristic frequencies of species A and B [25, 73, 70, 10].

[b] Grain-surface sites are equivalently local minimums of the interaction potential of species with the surface [104].

Hence, the total probability for the reaction to occur is defined by Eq.(2-10) [25, 73], which value is then used in Eq.(2-3) instead of κ_{AB}, as in Eq.(2-11)[c].

$$\kappa_{AB}^{final} = \frac{p_{reac}}{p_{reac} + p_{diff} + p_{evap}}, \tag{2-10}$$

$$k_{AB} = \frac{\kappa_{AB}^{final}\, p_{diff}}{N_{site}\, n_{dust}}, \tag{2-11}$$

These coefficients are then used to construct and solve a set of ODEs that indicate the rate at which species abundances change. For instance, the rate of change of fractional abundance of species on the surface of a grain is given by Eq.(2-12)[c].

$$\dot{Y}_{surf}(A) = -\frac{\kappa_{AB}^{final}\, p_{diff}}{N_{site}\, Y_{dust}} Y_{surf}(A) Y_{surf}(B). \tag{2-12}$$

where Y is the abundance of the reactants, $\dot{Y}$ is the rate of change of A, and Y_{dust} is the dust abundance. [c]

There is one ODE per species, which is a sum of the rates of each reaction (two-body reactions, cosmic ray interactions, UV photon interactions, freeze-out, non-thermal desorption, thermal desorption, grain surface reactions, bulk ice processes, etc.) in which the species participates [36]. The rates of each reaction are recalculated at each time step [36]. Finally, the ODE solver DVODE, adapted from Brown *et al.* (1989) [8], integrates the differential equations at the end of the time step [36]. Full description of the treatment of the grain-surface chemistry, the chemical reactive desorption formalism and the limitations of the rate equation approach use in UCLCHEM can be found in Quénard *et al.* (2018) [70].

Physical module

Several physics modules are integrated in UCLCHEM. In this section, we will discuss three particular models: Cloud, Hot Core, and C-shock, which we employed in our current study.

Cloud model

[c] See online documentation for more information.

The UCLCHEM cloud model is a physical model specifically designed to simulate the characteristics of spherical gas clouds. This module creates a one-dimensional model of a gas cloud by setting up a linear array of parcels from the cloud's center to its edge, controlling the density, temperature, and visual extinction of each parcel [36].

The cloud may collapse according to the free-fall profile as described in Eq. (2-13)[d]. This describes the rate of change in the atomic hydrogen number density, which is passed on to the integrator along with the abundances to be integrated over time. In Eq. (2-13) the density of hydrogen nuclei is represented by n_H, the initial central density by n_0, the mass of a hydrogen nucleus by m_H, and the factor used to slow the collapse by b_c [36] [d].

$$\frac{dn}{dt} = b_c \left(\frac{n_H^4}{n_0}\right)^{\frac{1}{3}} \left[24\pi\, G\, m_H\, n_0 \left(\left(\frac{n_H}{n_0}\right)^{\frac{1}{3}} - 1\right)\right]^{\frac{1}{2}}. \tag{2-13}$$

According to Holdship *et al.* (2017) [36], the free-fall model is suitable for single-point models that describe the densest part of the gas cloud, but it is fairly simplistic for modeling the collapse of prestellar cores. Therefore, users can choose other collapse modes in UCLCHEM apart from this simple approach. Priestley *et al.* (2018) [67] developed a collapse model, which parameterizes the density profile of a collapsing core as a function of time and radius. The modes in the collapse model include the Bonnor-Ebert sphere with an overdensity factor of 1.1 or 4 [1], as well as a magnetised filament that is prone to collapse [62], and a collapse due to ambipolar diffusion in a magnetised cloud [20, 19].

The collapse model is commonly used to evolve a set of self-consistent gas-grain molecular abundances based on the user-supplied network from purely elemental abundances through cloud collapse. The initial molecular abundances are set to zero while the elements are assigned to solar abundance values by default if not specified by users [36, 4]. These molecular abundances are then used as the initial values to model with a realistic astrophysical setup in stage 2, which may be a Hot Core or a C-shock phenomenon.

Hot Core model

The Hot Core model allows us to model the envelopes surrounding a forming protostar as a single point or along a one-dimensional line comprising gas parcels [36]. In this model, the temperature increases following the time and radially dependent temperature profiles (Eq.(2-14)) described by Viti *et al.* (2004) [94], and adapted in Awad *et al.* (2010) [5]. In Eq.(2-14)[94, 5] the variable r represents the distance from the current point to the center of the core, while R is the radius of the core. The remaining two constants, A, and B, are determined empirically, respectively.

[d] See online documentation for more information.

$$T = 10 + At^B \left(\frac{r}{R}\right)^{\frac{1}{2}} K. \tag{2-14}$$

When modeling the envelopes surrounding a forming protostar in UCLCHEM, the parameter entitled `max_temperature` in the Hot Core model is set to the final gas kinetic temperature achieved due to protostellar core heating. This temperature will be referred to as T_{HC} from now on. Please note that in Hot Core models, the dynamic gas kinetic temperature, $T_k\,(t)$, evolves over the course of the model as it approaches T_{HC}.

UCLCHEM also allows for the specification of the initial gas density in H nuclei per cm^{-3}, denoted as n_H, for all gas parcels using the `initialDens` parameter. However, for the purpose of contrasting chemical modeling with astronomical spectroscopic observations, it is essential to note that observationally, we can only infer the gas density in H_2 per cm^{-3}, n_{H_2}. To enhance clarity for readers, we will consistently use n_{H_2} to denote gas volume density in both modeling and observational contexts as $n_{H_2} \sim 2n_H$.

This approximation is justified, as in cold molecular regions such as the CND and SB-ring of NGC 1068, nearly all hydrogen exists in the form of H_2. Consequently, n_{H_2} can be used interchangeably with n_H unless there is extreme H_2 dissociation, which, as reported in Huang *et al.* (submitted) [37], and Vroom *et al.* (in prep), is not observed. Therefore, in an order of magnitude sense, it is acceptable to approximate n_H with n_{H_2}.

In Hot Core models, in contrast to C-shock models, the gas volume density remains constant throughout the entire protostellar core heating, maintaining the same initial value set up in the `initialDens` parameter. Therefore, $n_{H_2}\,(t) = n_{H_2\,(init)}$.

C-Shock model

UCLCHEM implements a version of the parameterized C-shock from Jiménez-Serra *et al.* (2008) [41] to depict the changes in shocked gas properties over time. The physical profile of the gas is then used as input in the chemical module to describe the time-dependent evolution of the molecular abundances in low- and high-velocity continuous shocks.

The physical shock structure is approximated by analytical equations for the temperature of fluids (T), particle density (n), and the velocity of the ions and neutrals, v_i and v_n, respectively [40].

The velocity of the ion and neutral fluids in the frame co-moving with the pre-shock gas, $v_{n,i}$, is approximated by Eq. (2-15)[41], while the velocity in the frame co-moving with the shocked gas, $v^*_{n,i}$, by Eq. (2-16) [41]. In these equations, z represents the spatial coordinate along shock propagation, v_s denotes the velocity of the shock, and v_0 is an additional velocity needed to avoid infinite compression of the far downstream gas. z_0 represents the distance

at which the ion and neutral fluids start to decouple. The z_n/z_i ratio provides a measure of the relative influence of ions and neutral particles on the fluid dynamics, as these parameters characterize the distance at which the ion-neutral interaction becomes important. Moreover, the variables z_0, z_i, and z_n serve as input parameters that control the velocity decoupling between the ions and the neutrals [41].

$$v_{n,i} = (v_s - v_0) - \frac{(v_s - v_0)}{cosh\left[(z - z_0)/z_{n,i}\right]}, \tag{2-15}$$

$$v^*_{n,i} = v_0 + \frac{(v_s - v_0)}{cosh\left[(z - z_0)/z_{n,i}\right]}. \tag{2-16}$$

The particle density of the neutral fluid, n_n, in the reference frame moving alongside the gas before it is shocked is given by Eq.(2-17)[41]. While n_n in the frame moving with the shocked gas is given by Eq.(2-18) [41]. The initial H_2 density of the ambient cloud is represented by n_0.

$$n_n = \frac{n_0\ v_s}{v_s - v_n}, \tag{2-17}$$

$$n_n = n_0\ v_s/v^*_n. \tag{2-18}$$

The temperatures of the ionic and neutral fluids, T_i and T_n, are estimated using the equations (2-19)[41] and (2-20)[41], respectively. These expressions are the same regardless of whether they are for a pre-shock or shocked gas co-moving frame. T_0 represents the initial temperature of the ambient cloud. The constant b_T is an integer used to fit the delay of the heating of the neutrals at specific stages. a_T and z_T are parameters related to the maximum value of T_n and the distance at which it reaches its maximum value. Both, a_T and z_T, are derived by assuming values for b_T [41].

$$T_i = T_n + \left(\frac{m\ v_d^2}{3k}\right), \tag{2-19}$$

$$T_n = T_0 + \frac{\left[a_T(z - z_0)\right]^{b_T}}{exp\left[(z - z_0)/z_T\right] - 1}. \tag{2-20}$$

When setting up a C-shock wave model in UCLCHEM, from a practical standpoint, the user defines the initial gas kinetic temperature, $T_{k,init}$, as the temperature outside the shock influence using the `initialTemp` parameter. This initial kinetic temperature, $T_{k,init}$, is effectively the final kinetic temperature, $T_{k,fin}$, as the gas is programmed to return to this value once the shock wave dissipates. Throughout the shock propagation, the dynamic gas kinetic temperature, $T_k\,(t)$, undergoes changes following the physics modeled in the system, akin to Hot Core Models. On the other hand, in C-shock models, the dynamic gas volume density, $n_{H_2}\,(t)$, increases from the initially set value, $n_{H_2\,(init)}$, due to shock compression. Therefore, $n_{H_2}\,(t) \neq n_{H_2\,(init)}$.

It should be noted that sputtering influences the release of chemical species into the gas phase from the surface of a dust grain through grain-grain collisions or desorption events (thermal or non-thermal). UCLCHEM's C-shock model utilizes the sputtering process described by Jiménez-Serra *et al.* (2008) [41]. In brief, the code initially calculates the average energy imparted to the grains from a collision between the shocked gas and the grains. This estimate is then combined with the collision rate and average yield for a specific energy to determine the sputtering rate. Finally, integration over time is performed [e].

2.1.2. MakeRates

UCLCHEM is advantegeous with the ability to solve a user-supplied chemical network. It uses a pre-processing Python script, MakeRates, to combine a gas phase reaction database with a user-supplied species list and additional reactions into the main code to run UCLCHEM [36]. To implement the radical-molecule route (Rxn.(1-7)) in the UCLCHEM network, we introduce a reaction list in the Makerates subdirectory (see online documentation), considering the reaction network given in Table **2-1**.

In UCLCHEM, gas phase chemistry uses the UMIST12 database, which lists the reactants and products with up to three rate constants (α, β, γ) for thousands of gas phase reactions. For instance, McElroy *et al.* (2013) [56] described the calculation of the reaction rate coefficient using α, β, and γ, for a two-body reaction following a type-Arrhenius formula as shown in Eq.(2-1) [56]. In reactions via the L-H mechanism, α is the branching ratio and γ is the energy barrier (in K) to the reaction. In this work network, we use the branching ratios proposed by Simons *et al.* (2020) [78] and the barrier energies reported in UMIST RATE2012 [56] and KIDA DATABASE [95] for the hydrogenation scheme and Álvarez-Barcia *et al.* (2018) [2] for the radical-molecule reaction.

[e] For detailed information on UCLCHEM's approach to C-shocks, sputtering and its limitations, consult the online documentation and Jiménez-Serra *et al.* (2008) [41].

Table 2-1.: Methanol formation reaction rate constants.

Reactions	Current			Default		
	α	β	γ	α	β	γ
$CH_3^+ + H_2O \longrightarrow CH_3OH_2^+ + h\nu$	2E-12[a]	0.0	0.0	2E-12[a]	0.0	0.0
$CH_3OH_2^+ + e \longrightarrow CH_3OH + H$	2.67E-8[b]	-0.59[b]	0.0	2.67E-8[b]	-0.59[b]	0.0
$H + CO \longrightarrow HCO$	1.0[e]	0.0	2500[d]	1.0[d]	0.0	2500[d]
$H + HCO \longrightarrow H_2CO$	0.417[e]	0.0	0.0	0.5	0.0	0.0
$H + HCO \longrightarrow CO + H_2$	0.583[e]	0.0	0.0	0.5	0.0	0.0
$H + H_2CO \longrightarrow CH_2OH$	7.27E-5[e]	0.0	5400[c]	0.33[c]	0.0	5400[c]
$H + H_2CO \longrightarrow CH_3O$	0.33[e]	0.0	2200[c]	0.33[c]	0.0	2200[c]
$H + H_2CO \longrightarrow HCO + H_2$	0.33[e]	0.0	1740[c]	0.33[c]	0.0	1740[c]
$H + CH_2OH \longrightarrow CH_3OH$	0.6[e]	0.0	0.0	1.0	0.0	0.0
$H + CH_3O \longrightarrow CH_3OH$	0.3[e]	0.0	0.0	1.0	0.0	0.0
$CH_3O + H_2CO \longrightarrow CH_3OH + HCO$	0.4[e]	0.0	2670[f]	-	-	-

[a] [52], [b] [27], [c] [72], [d] [95], [e] [78], [f] [2].

2.2. Modeling the Shock Chemistry for NGC 1068

This study uses the inferred gas properties from Huang *et al.* (submitted) [37], Vroom et al. (in prep), and Scourfield *et al.* (2020) [77] to model the physical scenario. Whilst, we use the branching ratios proposed by Simons *et al.* (2020) [78] and the barrier energies reported in UMIST RATE2012 [56], KIDA DATABASE [95] and Álvarez-Barcia *et al.* (2018) [2] for implementing the radical-molecule route into the UCLCHEM network aside from the traditional CO hydrogenation and pure gas-phase scheme reactions. Coupling the above with a detailed comparison of the shocked gas profiles built-up from the HNCO and SiO observations in Huang *et al.* (2022)[38], we are able to study the influence of molecular shocks induced by AGN feedback and formation pathways (processing of interstellar ices and pure gas phase mechanisms) on the observed interstellar methanol abundances, and to construct a more comprehensive picture of the shock history in these extragalactic environments.

In order to model the physical structure trace by CH_3OH, we used the inferred gas properties from Huang *et al.* (submitted) [37], and Vroom *et al.* (in prep) for five regions in the CND and two regions in the SB ring of NGC 1068. Specifically, $n_{H_2\,(init)}$ and $T_{k,init}$ in the CND and $n_{H_2\,(init)}$ in the SB ring. In addition, the cosmic ray ionization rate (CRIR, [ζ]) values were taken from the CS observations of NGC 1068 presented by Scourfield *et al.* (2020) [77].

Table **2-2** summarizes the physical conditions used to model the shock chemistry in the CND and SB Ring regions of NGC 1068. Tables **A-1**) and **A-2**) provide a complete list of all the models run individually for the CND and SB Ring, respectively.

The chemical modeling consists of two stages ordered in time sequence: The first is a gas infall model, which sets the proper initial molecular abundances for stage-2 evolution. In the second stage, we then evolve the chemistry with physical models that are of our science interest— for the current study, we modeled considering two scenarios: C-type shocks and Hot Cores, with the latter to represent non-shock cases.

The stage-1 gas in-fall was performed in a 10 pc radius cloud starting at a initial gas kinetic temperature of $T_{k,init} = 10$ K, a initial gas volume density of $n_{H_2\,(init)} = 10\ cm^{-3}$, and with a standard cosmic ray ionization rate (CRIR) for molecular hydrogen of ζ_0 (ζ_0= 5x10^{-17} s^{-1} [77]). We kept T_k constant while varying the final n_{H_2} due to the collapsing cloud. This increase of gas volume density stops when the specified n_{H_2} is reached. We consider two final gas volume densities ($n_{H_2} = 10^5$ and 10^6 cm^{-3}) for the CND cases and two values ($n_{H_2} = 10^3$ to 10^4 cm^{-3}) for the SB-ring cases (see Table **2-2**). The cloud was allowed to evolve for $\sim 10^7$ years as the specified n_{H_2} is reached.

For the CND, we modeled the C-type shocks with varying $T_{k,in}$, which is set as the initial and final gas kinetic temperature when the gas is outside the shock influence, from 10 to 100 K. In addition, we varied the CRIR from $\zeta = \zeta_0$ to $\zeta = 10\zeta_0$, and the shock velocity (v_{shock}) from 10 to 50 km/s. The chosen range for v_{shock} to establish a full range of speeds that allow us to distinguish between a low-velocity shock (10 km/s as representative value) and a high-velocity shock (50 km/s as representative value). In high-speed shocks, sputtering of the Si grain-core occurs, which is the main physical difference between the two models. Meanwhile, the non-shock model was simulated by heating up the cloud (composed of one gas parcel) to a final gas kinetic temperature, defined as the Hot Core temperature T_{HC}, of $T_{HC} = 50 - 100$ K, by considering a $10M\odot$ star embedded in the ISM without freeze-out reactions. For both shock and non-shock scenarios, the cloud was allowed to evolve for 10^7 years with an additional visual extinction at the cloud edge, A_ν, of 10 mag (see Tables **2-2** and **A-1**).

In the case of the SB-ring, we modeled the C-type shocks by varying the $T_{k,initial}$ from 10 to 100 K, the CRIR from $\zeta = \zeta_0$ to $\zeta = 100\zeta_0$, and v_{shock} from 10 to 50 km/s; while, the non-shock model was performed by heating the cloud (also composed of one gas parcel) to $T_{HC} = 50 - 100$ K, and considering a $10M\odot$ star with an ISM with non-freeze-out reactions. As well, in both scenarios, the cloud was allowed to evolve for 10^7 years with an additional visual extinction at the cloud edge, A_v, of 10 mag (see Tables **2-2** and **A-2**).

On the basis of the continuous CO hydrogenation in forming CH_3OH, the present study also includes the H-atom abstraction reaction in the final step for the formation of CH_3OH, as described by Santos *et al.* (2022) [75] and Simons *et al.* (2020) [78]. From this point forward, we will refer to the hydrogenation-only scheme as the "default" scheme, and the "current" scheme will refer to the scheme in which the radical-molecule H-atom abstraction route is also incoporated in the chemical modeling. In addition, UCLCHEM employs a specific notation to differentiate between various species. Ice formation is based on a three-phase model that takes into account the gas, grain surface, and grain bulk. Both the surface and bulk of the

grain contribute to ice formation. Henceforth, the term 'ice phase' will refer to the combined contribution of the grain surface and bulk. The surface and bulk of interstellar ice- dust grains will be analyzed separately.

Currently, UCLCHEM does not differentiate between the behavior of Type A and Type E methanol regarding any physical and chemical processes. Thus, the model treats both forms of methanol as indistinguishable.

Table 2-2.: CND and SB Ring physical conditions

Variable	CND	SB-Ring
Gas temperature, $T_{k,init}$ (or T_{HC}) $[K]$	10.0, 50.0, 100.0	10.0, 50.0, 100.0
Gas density, $n_{H_2\,(init)}$ $[cm^{-3}]$	$10^5, 10^6$	$10^3, 10^4$
CRIR, ζ $[\zeta_0]$	1.0, 10.0	1.0, 10.0, 100.0
Extinction, A_v $[mag]$	10.0	10.0
C-shock velocity, v_{shock} $[km/s]$	10.0, 50.0	10.0, 50.0
Physical model	Shock or non-shocked scenario	Shock or non-shocked scenario
Network	Current or default	Current or default

2.3. Benchmarking

To establish a reference point, we compared the gas-phase methanol (CH_3OH) with three reference molecules: hydrogen (H_2), water (H_2O), and carbon monoxide (CO) using the simplest model (Model 1 in Table **A-1**). The objective was to analyze whether the newly added H-abstraction reaction affects the abundance evolution of common species that are not direct precursors or products in methanol formation. In addition, we contrasted the formation and destruction pathways of methanol in the default and current schemes, taking into account both the gas and solid phases, including grain-surface and bulk. To accomplish this, we employed the analysis tool in UCLCHEM "uclchem.analysis.analysis()", which identifies the most significant changes in methanol abundances associated with formation and destruction reactions at each time step.

In order to reduce computational expenses, this model was executed without integrating the freeze-out rate as an input. This approximation is legitimate, since the time frame for freeze-out prominently exceeds the evolution timescale investigated by current study.

Model 1: Hot Core

Model 1 in the table **A-1** is a non-shock model characterized by $n_{H_2\,(init)} = 10^5\ cm^{-3}$, a standard CRIR ($\zeta_0$), and a T_{HC}=50 K. To test the element abundance conservation of

each model in Table A-1, we used the "check element conservation" function in UCLCHEM, which returns the change in the total abundance of an element as a percentage of the original. In Model 1, both schemes have the same conservation: $< 0.01\,\%$ for H, N, C and O, which indicates that the total abundance is properly conserved throughout the evolution in the model.

Figures 2-1 and 2-2 are both associated with Model 1, with specifications listed in Table A-1. Figure 2-1 has brown, orange, and light blue lines corresponding to H_2O, H_2, and CO, respectively. At the same time, the dark blue lines show the CH_3OH evolution considering the current (solid) and the default (dashed) schemes. $T_k\,(t)$ is represented by the dotted grey line, and $n_{H_2\,(init)}$ is represented by the dotted red line. As can be seen, the Hot Core model is characterized by an increase in gas kinetic temperature while the gas volume density remains constant.

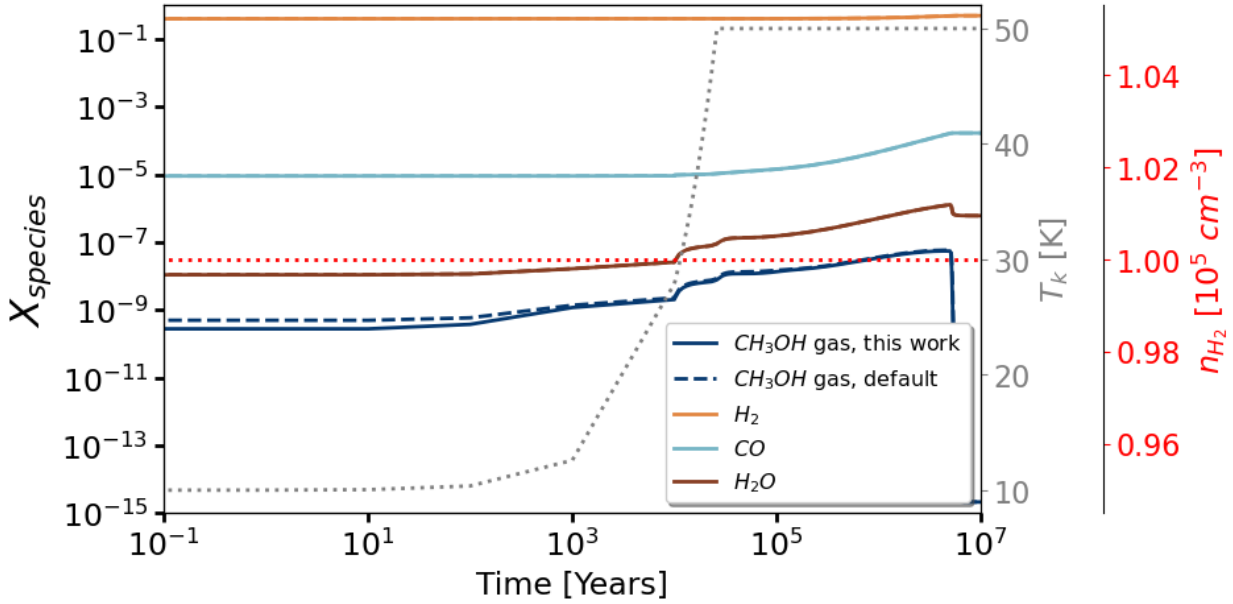

Figure 2-1.: Chemical abundances of H_2 (orange), H_2O (brown), CO (light blue), and CH_3OH (dark blue) in the gas phase over time for Model 1. The dashed and solid lines correspond to the default and current schemes, respectively. Gas kinetic temperature evolution, $T_k\,(t)$, is depicted by the dotted grey line, while $n_{H_2\,(init)}$ is illustrated by the dotted red line.

With increasing $T_k\,(t)$, the abundance of gas-phase hydrogen remains nearly constant over time, while the abundances of CO, H_2O, and CH_3OH increase slightly. As expected, the newly added H-abstraction reaction does not significantly affect, at least in a first-order sense, the abundance evolution of H_2, CO, and H_2O. This implies that their abundance is unaffected by the scheme employed. However, the abundance of gas-phase methanol is slightly larger ($\geq 10^{-10}$) in the default scheme, with a small increase (approximately 10^{-9}) in the default gas phase (dashed blue line) up to 10^4 years.

Figure 2-2 specifically depicts the evolution of methanol abundance in its three phases over time. Solid lines represent the evolution considering the current scheme, while the dashed lines represent the default setting. Blue, green, and purple correspond to methanol in the gas phase, on the surface, and in the bulk of the grain, respectively.

Similar to what's noted earlier, the abundance of methanol across its gas, surface, and bulk phases is slightly larger in the default scheme compared to the current one. There is no significant difference in the formation and destruction reactions for gas and grain-surface phase methanol in both schemes at each time step. However, the most significant difference between the two schemes is shown in the formation scheme of bulk methanol. Specifically, in the current scheme, the H-abstraction reaction (1-7) is the primary method for methanol formation. Conversely, in the default scheme, the CH_3O hydrogenation reaction dominates throughout the entire evolution. In the next chapter, a more comprehensive analysis of the CH_3OH formation and destruction pathways will be presented, elucidating how each scheme influences the evolution of methanol abundance over its three phases in the context of the associated physical scenario.

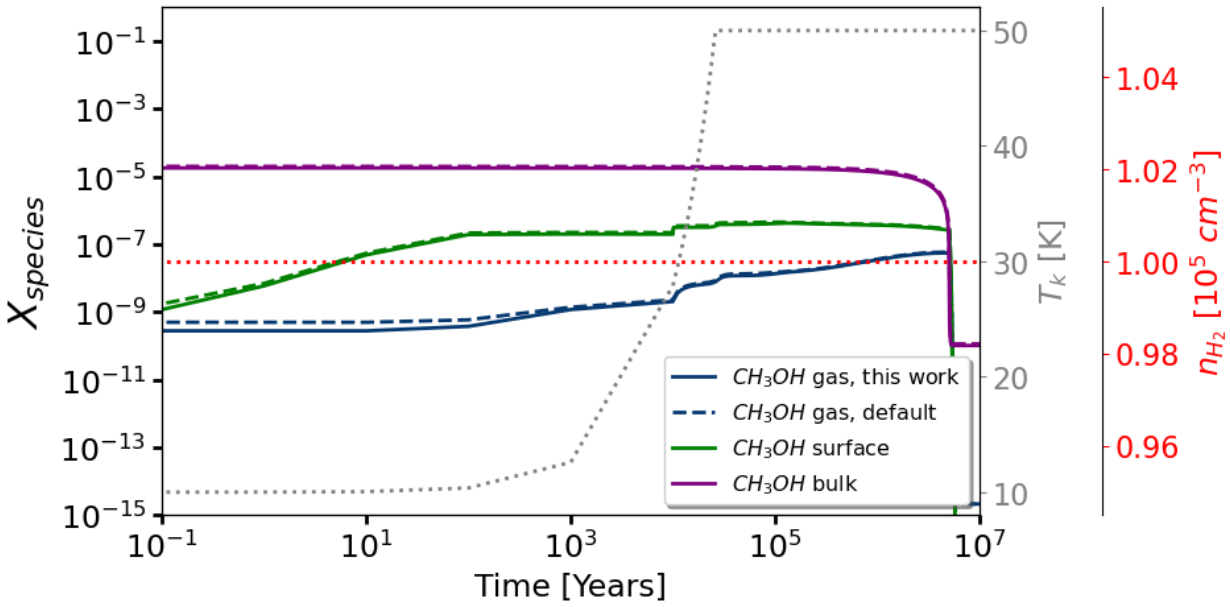

Figure 2-2.: Chemical abundances of CH_3OH in gas (dark blue), surface (green) and bulk (purple) phases over time for Model 1. The dashed and solid lines correspond to the default and current schemes, respectively. Gas temperature evolution, $T_k\,(t)$, is depicted by the dotted grey line, while $n_{H_2\,(init)}$ is illustrated by the dotted red line.

3. Results & Analysis

3.1. Methanol as a C-shock tracer

We analyzed the 80 physical models (160 if we consider that each model was run with both the default and the current scheme) listed in Table **2-2** [a]. If the reader wishes to consult set up for individual numbered cases discussed in-text, please refer to Tables **A-1** and **A-2**. The purpose of this analysis is to study the chemistry at different shock velocities and in non-shock environments, and its effects on the abundance of methanol in the gaseous and solid phases. Additionally, we examined the conservation of element abundance in these models. The abundance of H, N, C, and O remained below 5 % regardless of the scheme used.

The molecular transitions observed in Huang *et al.* (submitted) [37], and Vroom *et al.* (in prep), stem from gas-phase material, including CH_3OH. Consequently, the analyses presented in Section 3.1.1 pertain exclusively to gas-phase abundances. To facilitate a meaningful comparison with observational results (refer to Section 3.1.3), it is essential to focus on gas-phase abundances in the modeling approach.

3.1.1. Gas-phase CH_3OH abundance and its dependence on v_{shock}

In Hot Core Models

The analysis of gas-phase CH_3OH in Hot Core models, as our non-shock scenarios, can yield understanding in CH_3OH behavior in non-shock conditions. Figures **3-1** to **3-3** show a comparison of the gaseous methanol abundance over time in Hot Core models with different T_{HC} and CRIR. Each Figure contains four cases of initial gas volume density ($n_{H_2\,(init)}$): $10^3 cm^{-3}$ in purple, $10^4 cm^{-3}$ in blue, $10^5 cm^{-3}$ in green and $10^6 cm^{-3}$ in yellow. The difference among Figures **3-1** to **3-3** is regarding T_{HC} and CRIR (ζ), with each - 50K and $1\zeta_0$ in Fig **3-1**, 50K and $10\zeta_0$ in Fig **3-2**, and 100K and $10\zeta_0$ in Fig **3-3**. According to Figure **3-1**, gaseous CH_3OH abundance increases as the initial gas volume density ($n_{H_2\,(init)}$) between models increases. However, at relatively low initial densities ($n_{H_2\,(init)} = 10^3\ cm^{-3}$), such as

[a] We want to note that we were unable to fully analyze Models 29 and 30 in Table **A-1** due to an error in updating the chemistry.

those found in the SB-ring, the increase is almost imperceptible. $n_{H_2\,(init)}$ is the crucial factor affecting gaseous CH_3OH abundance, although a higher CRIR also seems to play a role in gas-phase CH_3OH destruction (refer to Figure **3-2**). In addition, increasing T_{HC} across models results in even more pronounced abundance growth at higher $n_{H_2\,(init)}$, up to two magnitudes (refer to Figure **3-3** in contrast to **3-2**).

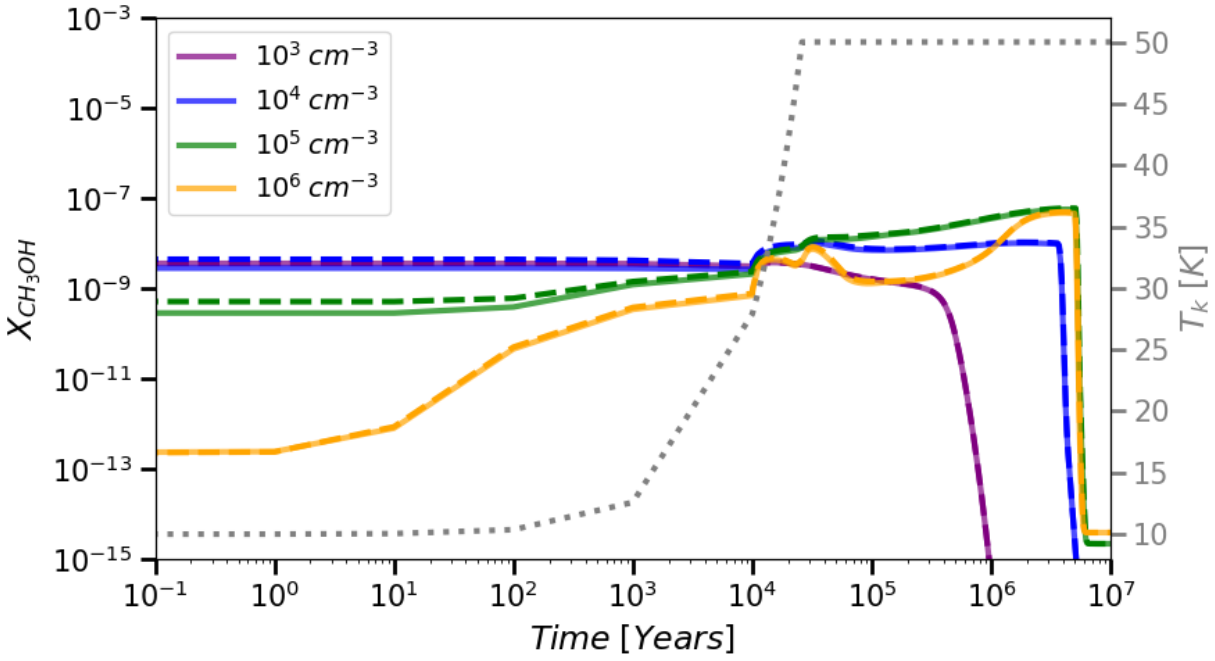

Figure 3-1.: Comparison of the gaseous methanol abundance at different $n_{H_2\,(init)}$ ($10^3\,cm^{-3}$ in purple, $10^4\ cm^{-3}$ in blue, $10^5\ cm^{-3}$ in green and $10^6\ cm^{-3}$ in yellow) over time in Hot Core models with T_{HC}=50 K and $\zeta = \zeta_0$. The dashed and solid lines correspond to the default and current schemes, respectively. The gas temperature evolution, $T_k\,(t)$, is shown by the dashed gray line.

Before $T_k\,(t)$ increases over time, gas-phase methanol formation is mainly due to CH_3O hydrogenation and subsequent chemical desorption (Rxn.(3-1)[78, 58]), with an important contribution from CH_2OH hydrogenation (Rxn.(3-2)[78, 58]) in the models at $n_{H_2\,(init)} = 10^3 cm^{-3}$. The destruction of CH_3OH occurs primarily via ion-neutral Rxn.(3-3)[79], but high CRIR makes cosmic ray-induced photoreaction in Rxn. (3-4)[95] dominant over Rxn.(3-3). For the models with $n_{H_2\,(init)} = 10^6\ cm^{-3}$, the destruction of CH_3OH is primarily due to ion-neutral Rxn.(3-5)[66].

$$H_{(s)} + CH_3O_{(s)} \longrightarrow CH_3OH_{(g)}, \tag{3-1}$$

$$H_{(s)} + CH_2OH_{(s)} \longrightarrow CH_3OH_{(g)}. \tag{3-2}$$

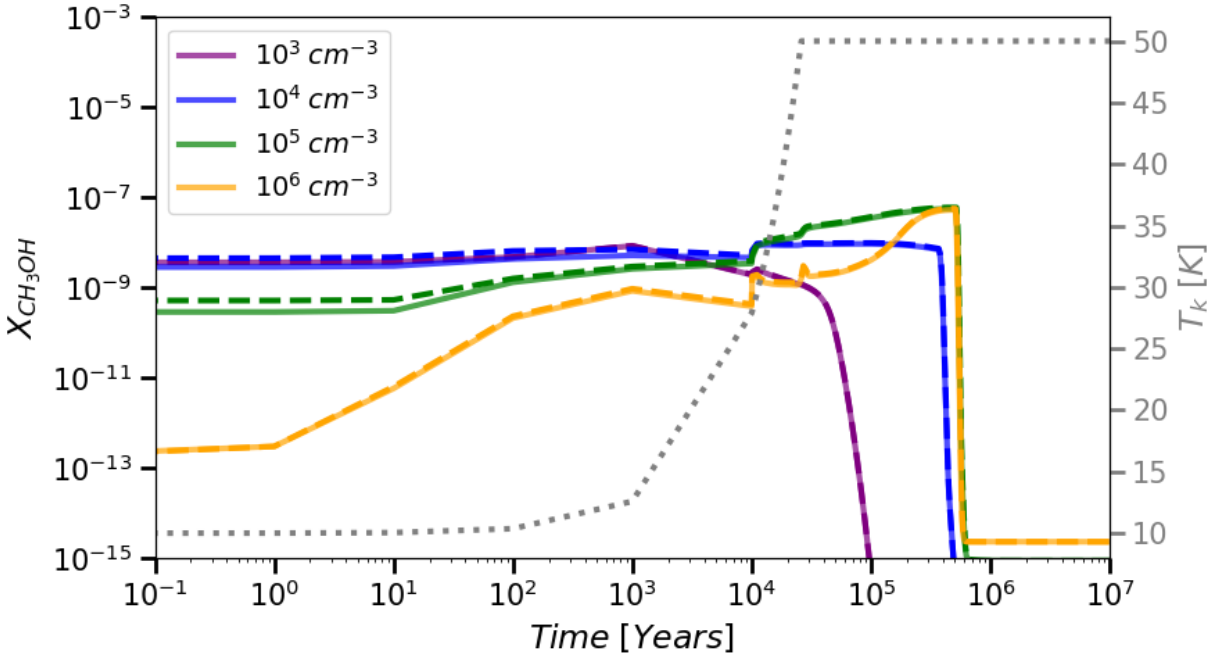

Figure 3-2.: Comparison of the gaseous methanol abundance at different $n_{H_2\,(init)}$ ($10^3\,cm^{-3}$ in purple, $10^4\ cm^{-3}$ in blue, $10^5\ cm^{-3}$ in green and $10^6\ cm^{-3}$ in yellow) over time in Hot Core models with T_{HC}=50 K and $\zeta = 10\zeta_0$. The dashed and solid lines correspond to the default and current schemes, respectively. The gas temperature evolution, $T_k\,(t)$, is shown by the dashed gray line.

$$C^+ + CH_3OH \longrightarrow HCO + CH_3{}^+, \tag{3-3}$$
$$CH_3OH + CRPHOT \longrightarrow H_2CO + H_2, \tag{3-4}$$
$$He^+ + CH_3OH \longrightarrow OH + CH_3{}^+ + He. \tag{3-5}$$

As the gas kinetic temperature increases due to heating from the protostellar core, the hydrogenation of CH_3O at the grain surface is generally replaced by the same hydrogenation occurring in the bulk (innermost layers) of the grain, or by multiple reactions such as the hydrogenation of CH_2OH in Rxn.(3-2), ion-neutral in Rxn. (3-6)[83], and protonated methyl alcohol ($CH_3OH_2{}^+$) recombination in Rxn. (3-7)[27]. The difference between each case is attributed to T_{HC}, with CH_3O_{bulk} hydrogenation dominating in models at T_{HC}=50 K, while the other reactions dominate in models at T_{HC}=100 K. For models with $n_{H_2\,(init)} = 10^3\,cm^{-3}$, the generality is fulfilled, except that at $\zeta = 10-100\zeta_0$, UV-radiation desorption takes place. On the other hand, an increase in $T_k\,(t)$ results in destruction caused by ion-neutral Rxns (3-3) and (3-8)[80], and potential CH_3OH condensation once the temperature stabilizes.

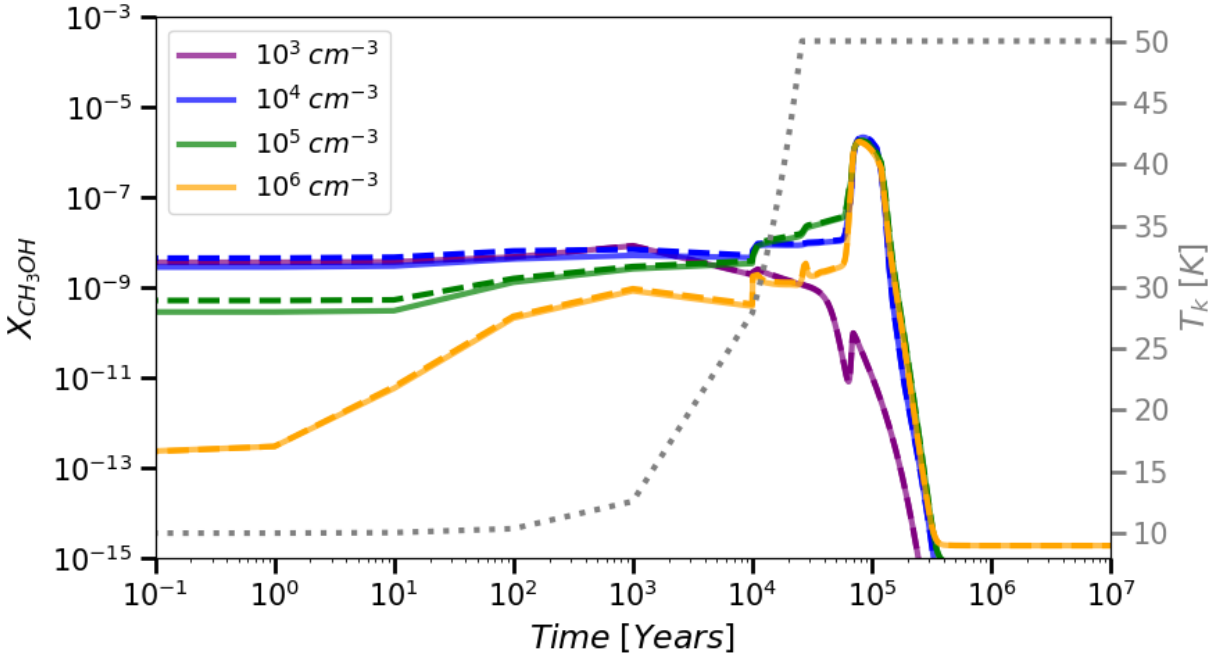

Figure 3-3.: Comparison of the gaseous methanol abundance at different $n_{H_{2\,(init)}}$ ($10^3\,cm^{-3}$ in purple, $10^4\ cm^{-3}$ in blue, $10^5\ cm^{-3}$ in green and $10^6\ cm^{-3}$ in yellow) over time in Hot Core models with T_{HC}=100 K and $\zeta = 10\zeta_0$. The dashed and solid lines correspond to the default and current schemes, respectively. The gas temperature evolution, $T_k\,(t)$, is shown by the dashed gray line.

$$H_3^+ + CH_3CHO \longrightarrow CH_3^+ + CH_3OH, \tag{3-6}$$
$$CH_3OH_2^+ + e^- \longrightarrow CH_3OH + H. \tag{3-7}$$

$$H^+ + CH_3OH \longrightarrow H_3CO^+ + H_2. \tag{3-8}$$

Figures 3-1 to 3-3 demonstrate that the abundance of gaseous methanol varies between the default and current schemes. Although the behavior observed in the studied gas phases is similar, the default scheme predicts in general a higher abundance of gas-phase methanol ($\sim 10^{-10}$). The reactions at each step of the models are nearly identical for both schemes. However, the current scheme has a significantly higher incidence of CH_2OH hydrogenation due to the change in branching ratios. The difference in abundances is attributed to the reaction network displayed in the solid phase (grain-surface and grain-bulk) rather than in the gas phase. This will be analyzed in Section 3.2.

In C-shock Models

Contrasting to the analysis in the non-shock models, to evaluate the potential of methanol as a shock tracer, we conducted a thorough analysis of C-shock models under varying physical conditions and velocities as summarized in Table. **2-2**. For the C-shock models, we divide the chemical analysis into three segments according to the epoch of shock propagation. The pre-shock epoch corresponds to the time in which the initial $T_k\,(t)$ remains low and is the same as $T_{k,init}$. The beginning of the shock is determined by the rise of $T_k\,(t)$ due to shock heating, and the end of the shock is determined by its decrease until it reaches the cold temperature again. The post-shock epoch is then the segment in which $T_k\,(t)$ returns to the initial temperature, $T_{k,ini}$, of the model and remains constant over time.

Our results clearly indicate that methanol serves as a reliable tracer due to its abundance enhancement during shock wave propagation. As an example, Figure **3-4** contrasts a non-shock scenario (from Hot Core model), a low velocity C-shock model (v_{shock}=10 km/s), and a high velocity C-shock model (v_{shock}=50 km/s) with $n_{H_2\,(init)} = 10^5\,cm^{-3}$, $T_{k,init}$=50 K, and $\zeta = \zeta_0$. Comparing the three models regarding shock condition in this Figure, it is evident that the gaseous methanol abundance increases significantly by four orders of magnitude as the shock wave propagates, regardless of the velocity of the wave. The amount of gaseous methanol increases while the solid-state methanol, whether on the surface or in the bulk, decreases significantly. In other words, the increase in gaseous methanol happens as the ice-dust grain sputters or sublimates due to the shock. Thus, it can be inferred that methanol exhibits sensitivity to C-type shock waves under the given conditions.

However, there are some interesting cases that should be highlighted. At low inital gas density of $n_{H_2\,(init)} = 10^3\,cm^{-3}$, shock velocity evidently affects the methanol abundance as the increase at v_{shock} =10 km/s is slightly higher than at v_{shock} =50 km/s, as shown in Figure **3-5**. Another intriguing case arises at an $T_{k,init}$=100 K and $n_{H_2\,(init)} = 10^4\,cm^{-3}$ (Figure **3-6**), where the sublimation process in the hot core leads to a comparable rise in abundance by the end of evolution as in both shock models.

Figure **3-7** present a comparison of methanol abundance over time as a function of inital gas volume density at $n_{H_2\,(init)} = 10^3\,cm^{-3}$ (dark green), $n_{H_2\,(init)} = 10^4\,cm^{-3}$ (yellow), $n_{H_2\,(init)} = 10^5\,cm^{-3}$ (light blue) and $n_{H_2\,(init)} = 10^6\,cm^{-3}$ (dark blue) in low-velocity C-shock models with $T_{k,init}$=10 K and $\zeta = \zeta_0$. In Figure **3-7** is clear that the gaseous methanol abundance enhancement resulting from shock wave propagation is most apparent at high $n_{H_2\,(init)}$, such as $n_{H_2\,(init)} = 10^6\,cm^{-3}$, where the increase in abundance is more significant and stable than in cases of lower $n_{H_2\,(init)}$, such as $n_{H_2\,(init)} = 10^3\,cm^{-3}$. For example, for a model with $n_{H_2\,(init)} = 10^6\,cm^{-3}$, the increase is in the order of 6 orders of magnitude compared to the 2 orders of magnitude increase in the $n_{H_2\,(init)} = 10^3\,cm^{-3}$ case.

Figures **3-8** and **3-9** depict a comparison of methanol abundance over time, illustrating the relationship with both CRIR and $T_{k,init}$. Higher gas volume densities enhance the effective-

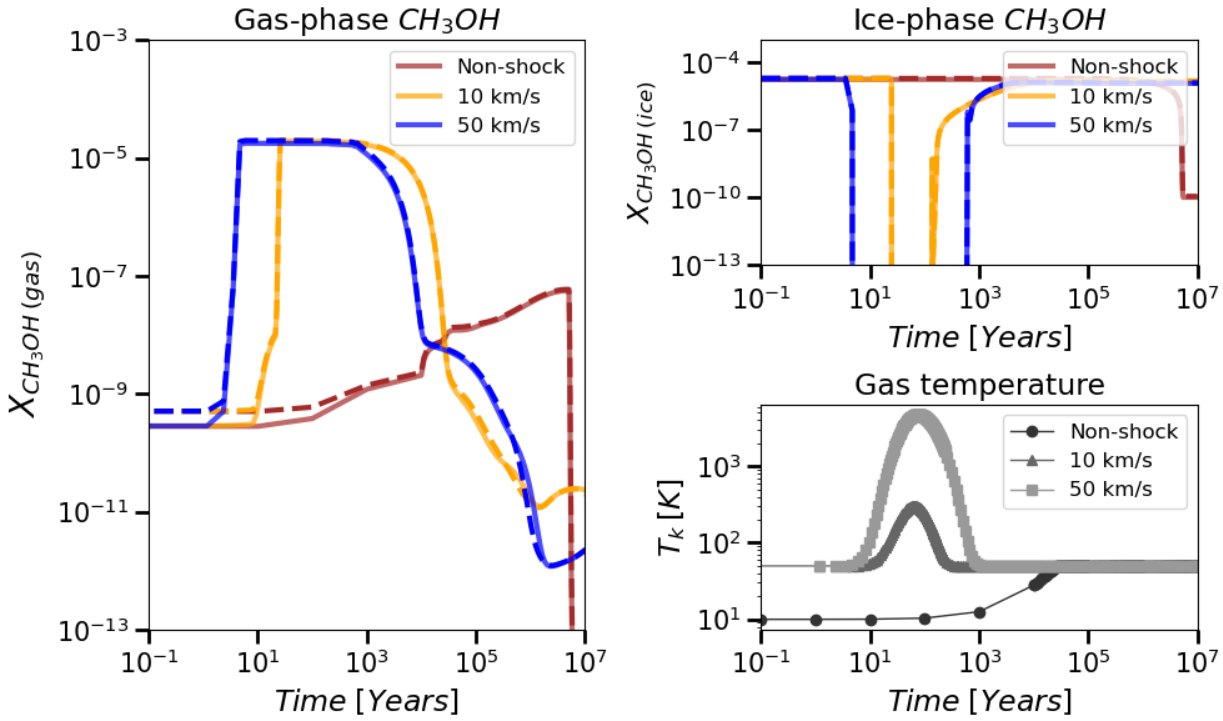

Figure 3-4.: Comparison of methanol abundance over time as a function of shock wave velocity in non-shock (red), low-velocity (blue), and high-velocity C-shock (yellow) models with $n_{H_2\,(init)} = 10^5\ cm^{-3}$, $T_{k,init}$=50 K, and $\zeta = \zeta_0$. The dashed and solid lines correspond to the default and current schemes, respectively. The left panel shows the gas-phase methanol abundance, while the top right panel displays the ice-phase (grain surface + bulk) methanol abundance. The gas temperature evolution, $T_k\,(t)$, of each model is illustrated by the gray lines in the bottom right panel.

ness of mitigating cosmic ray destruction. For instance, when ionization occurs in models with $n_{H_2\,(init)} = 10^3\,cm^{-3}$ and high CRIR ($\zeta = 10 - 100\zeta_0$), gaseous methanol initially enhances but in the maximum $T_k\,(t)$, it shows a considerable decline in abundance as the shock wave proceeds (Figure 3-8). In these specific conditions, the impact associated with different low initial gas temperatures, $T_{k,init}$, is more noticeable. At low initial $T_{k,init}$, methanol is destroyed by the shock but reforms shortly after. In contrast, methanol abundance does not rebound in cases of high $T_{k,init}$. When analyzing the difference associated with the $T_{k,init}$ in Figure 3-9, it is obvious that the abundance of gaseous methanol is higher during both the pre- and post-shock epochs with higher $T_{k,init}$. In contrast, the solid-state CH_3OH abundance increases as the gas phase decreases in abundance due to condensation, as expected in a lower temperature ($T_{k,init}$) environment.

In our models, CH_3OH abundance behavior is highly time variable over the course of shock propagation, thus we will divide the full evolution course into three epochs: pre-/during-

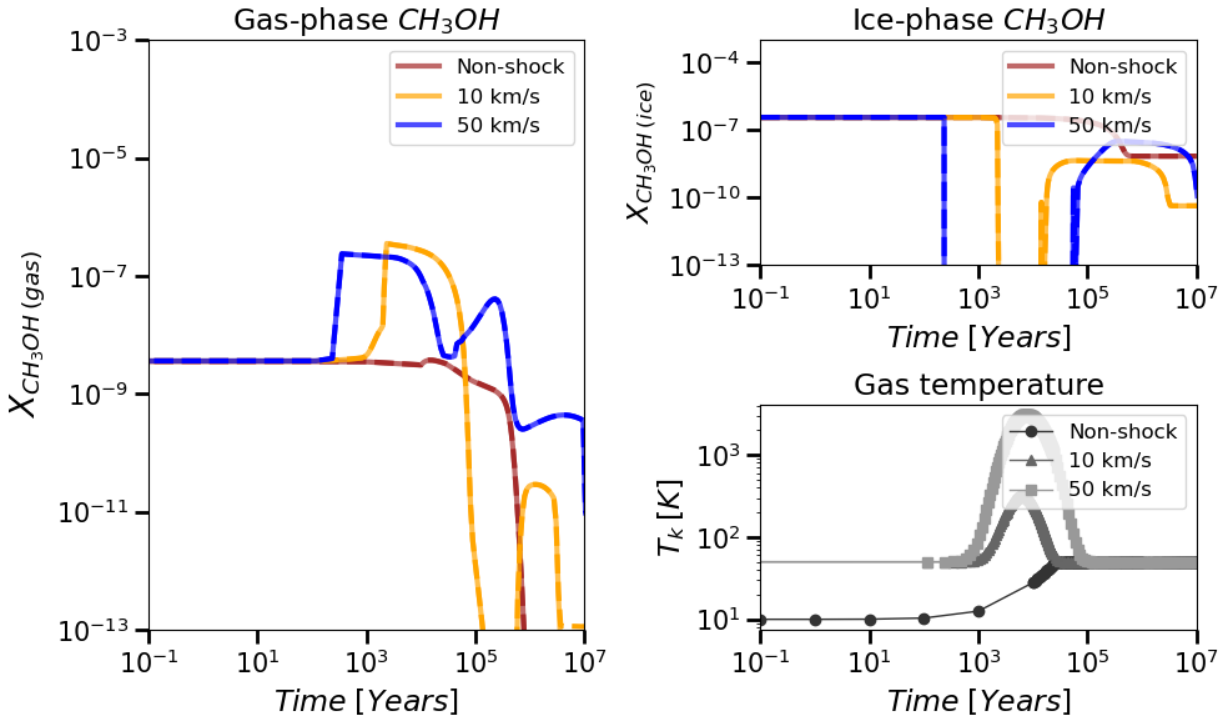

Figure 3-5.: Comparison of methanol abundance over time as a function of shock wave velocity in non-shock (red), low-velocity (blue), and high-velocity C-shock (yellow) models with $n_{H_2\,(init)} = 10^3\ cm^{-3}$, $T_{k,in}$=50 K, and $\zeta = \zeta_0$. The dashed and solid lines correspond to the default and current schemes, respectively. The left panel shows the gas-phase methanol abundance, while the top right panel displays the ice-phase (grain surface + bulk) methanol abundance. The gas temperature evolution, $T_k\,(t)$, of each model is illustrated by the gray lines in the bottom right panel.

/post- shock. Hereafter, we will analyze each epoch for gas-phase methanol.

Pre- and Post- shock epochs The formation of gas-phase methanol during both the pre- and post-shock epochs is primarily attributed to the hydrogenation of CH_3O, as depicted in Rxn.(3-1). However, at elevated $T_k\,(t)$, the hydrogenation of CH_2OH and sublimation, particularly in cases with $n_{H_2\,(init)} = 10^3\ cm^{-3}$, also contribute to the formation process. These pathways for methanol formation remain unaffected by the shock wave velocity, except for the CH_2OH hydrogenation at $T_{k,init}$=100 K, which becomes notably more pronounced at v_{shock}=50 km/s. It is noteworthy that the radical-molecule H-atom abstraction route, Rxn.(3-9)[78, 58], occurs at $n_{H_2\,(init)} = 10^6\ cm^{-3}$, $\zeta = 1\zeta_0$, and $T_{k,init}$=100 K during the pre-shock epoch.

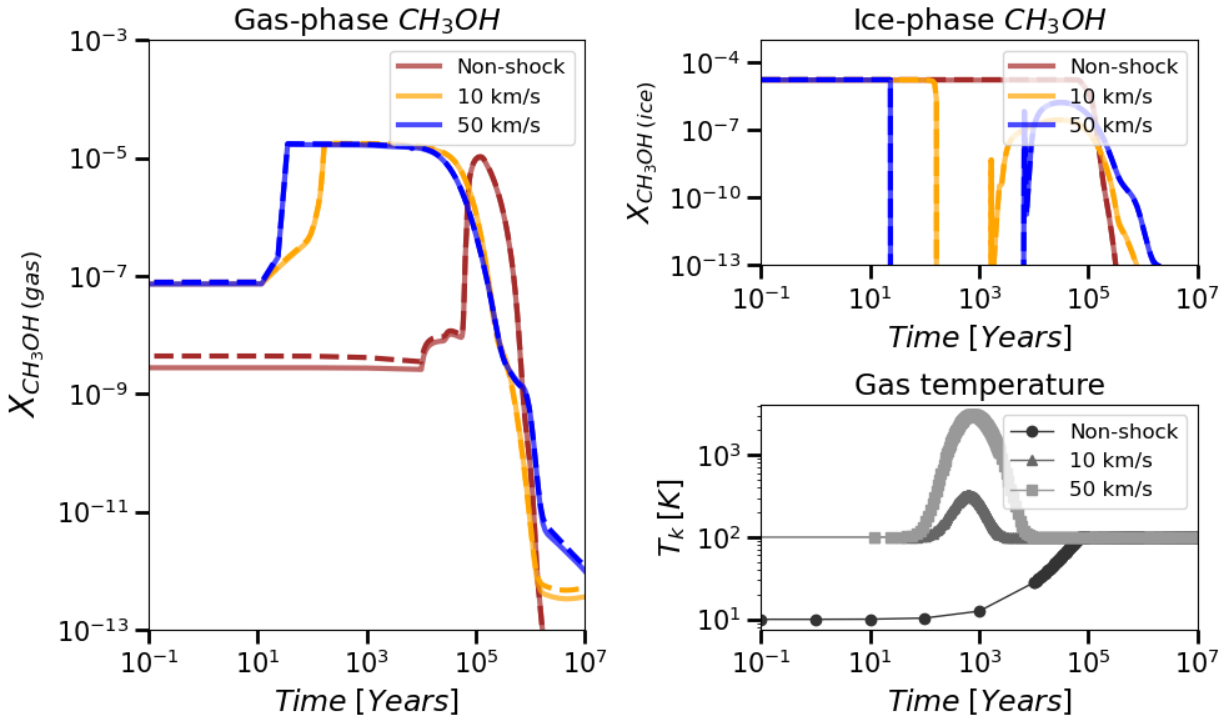

Figure 3-6.: Comparison of methanol abundance over time as a function of shock wave velocity in non-shock (red), low-velocity (blue), and high-velocity C-shock (yellow) models with $n_{H_2\,(init)} = 10^4\,cm^{-3}$, $T_{k,init}$=100 K, and $\zeta = \zeta_0$. The dashed and solid lines correspond to the default and current schemes, respectively. The left panel shows the gas-phase methanol abundance, while the top right panel displays the ice-phase (grain surface + bulk) methanol abundance. The gas temperature evolution, $T_k\,(t)$, of each model is illustrated by the gray lines in the bottom right panel.

$$H_2CO_{(s)} + CH_3O_{(s)} \longrightarrow CH_3OH_{(g)} + H_{(g)}. \tag{3-9}$$

In contrast, Rxn.(3-3) predominantly leads to the destruction process for both velocities, resulting in HCO and CH_3^+ formation in the pre-shock epoch. However, in certain situations, other reactions may take precedence. For instance, using high CRIR and low gas densities ($\zeta = 100\zeta_0$ and $n_{H_2\,(init)} = 10^3 - 10^4\,cm^{-3}$) generally leads to the formation of H_2CO and H_2 from Rxn.(3-4), whereas Rxn.(3-5) causes CH_3^+, OH and He formation at $n_{H_2\,(init)} = 10^6\,cm^{-3}$. These reactions are the same to those mentioned above for the non-shock models. Furthermore, the post-shock epoch is influenced by a multitude of reactions, including those highlighted in the pre-shock epoch, along with condensation and ion-neutral reactions, as illustrated in Rxn.(3-10)[3] and Rxn.(3-11)[85]. Notably, the significance of the latter two reactions becomes more pronounced at elevated $n_{H_2\,(init)}$.

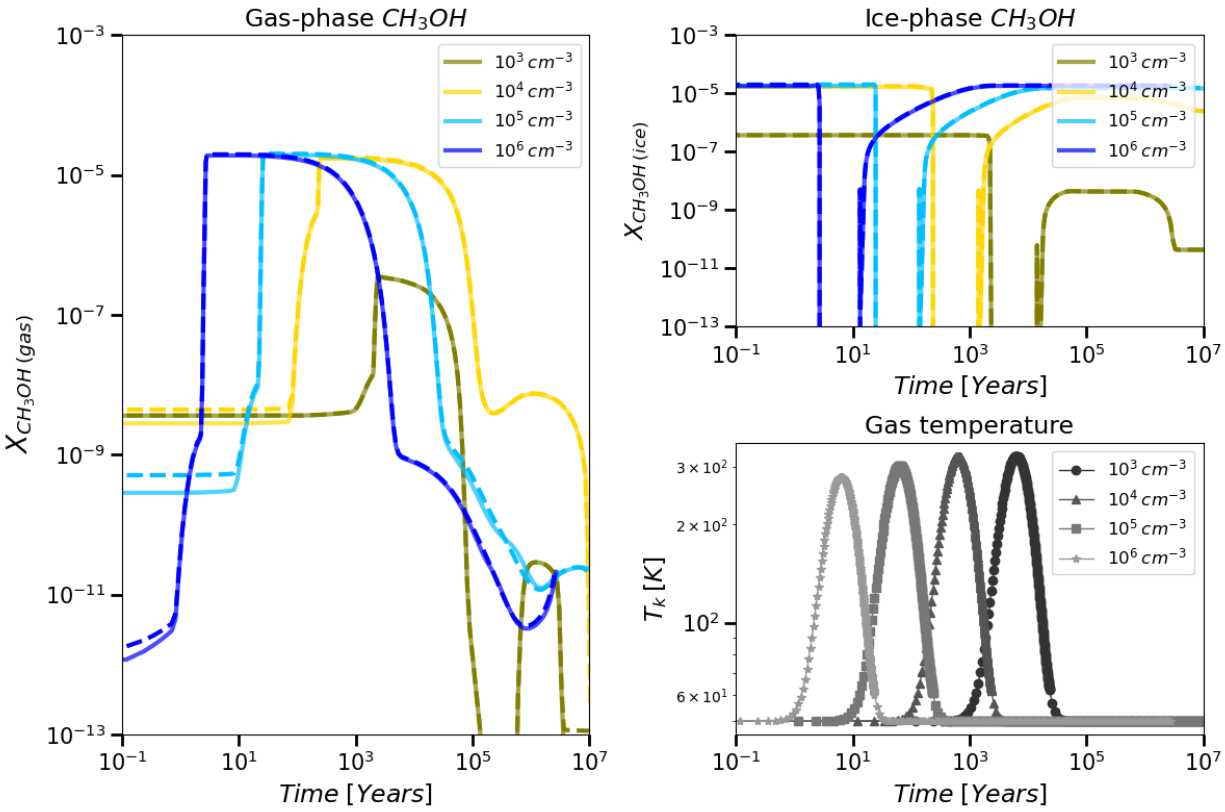

Figure 3-7.: Comparison of methanol abundance over time as a function of initial gas volume density at $n_{H_2\,(init)} = 10^3\,cm^{-3}$ (dark green), $n_{H_2\,(init)} = 10^4\,cm^{-3}$ (yellow), $n_{H_2\,(init)} = 10^5\,cm^{-3}$ (light blue) and $n_{H_2\,(init)} = 10^6\,cm^{-3}$ (dark blue) in low-velocity C-shock models with $T_{k,init}$=10 K and $\zeta = \zeta_0$. The dashed and solid lines correspond to the default and current schemes, respectively. The left panel shows the gas-phase methanol abundance, while the top right panel displays the ice-phase (grain surface + bulk) methanol abundance. The gas temperature evolution, $T_k\,(t)$, of each model is illustrated by the gray lines in the bottom right panel.

$$H_3O^+ + CH_3OH \longrightarrow CH_3OH_2{}^+ + H_2O, \tag{3-10}$$

$$HCO^+ + CH_3OH \longrightarrow CH_3OH_2{}^+ + CO. \tag{3-11}$$

During Shock Influence As gas kinetic temperature, $T_k\,(t)$, and gas volume density, $n_{H_2\,(t)}$, rise within the shock, the formation and destruction reactions that were previously highlighted in the pre-shock epoch change throughout the wave propagation. It is crucial to consider these new reactions as they become significant under the evolving conditions in the shocked environment.

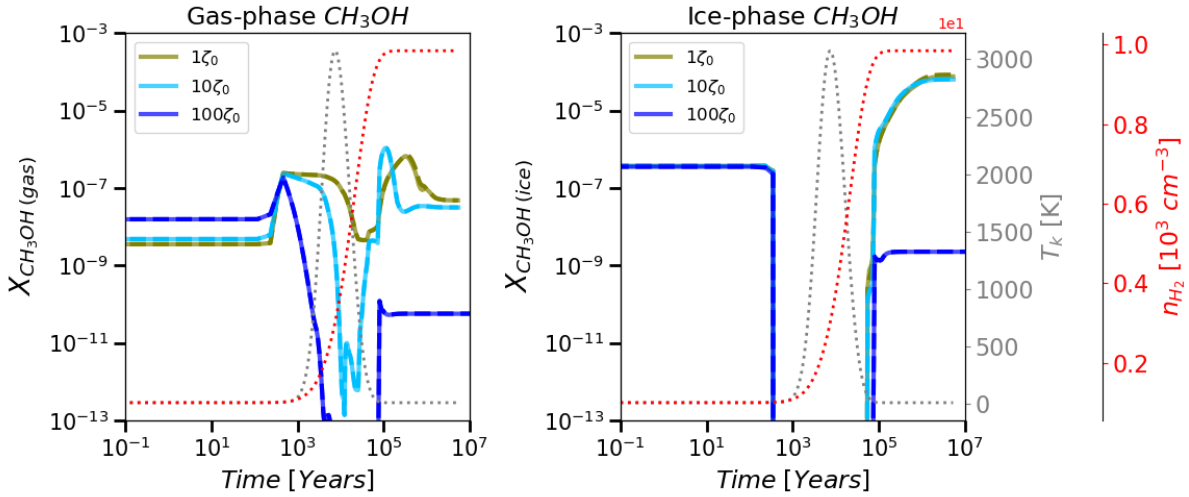

Figure 3-8.: Comparison of methanol abundance over time as a function of CRIR at $\zeta = \zeta_0$ (dark green), $\zeta = 10\zeta_0$ (light blue) and $\zeta = 100\zeta_0$ (dark blue) in high-velocity C-shock models with $n_{H_{2\,(init)}} = 10^3\ cm^{-3}$ and $T_{k,init}$=10 K. The dashed and solid lines correspond to the default and current schemes, respectively. The evolution of $T_k\ (t)$ is depicted by the gray dotted line, while the evolution of $n_{H_2}\ (t)$ is represented by the red dotted line.

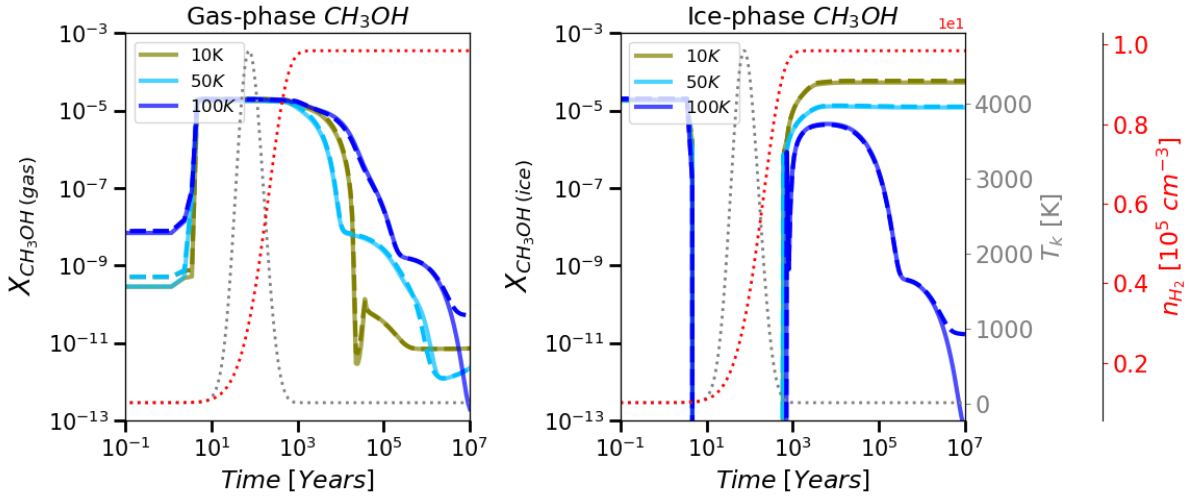

Figure 3-9.: Comparison of methanol abundance over time as a function of $T_{k,init}$ at $10K$ (dark green), $50K$ (light blue) and $100K$ (dark blue) in low-velocity C-shock models with $n_{H_{2\,(init)}} = 10^5\ cm^{-3}$ and $\zeta = \zeta_0$. The dashed and solid lines correspond to the default and current schemes, respectively. The evolution of $T_k\ (t)$ is depicted by the gray dotted line, while the evolution of $n_{H_2}\ (t)$ is represented by the red dotted line.

In low-velocity C-shocks, CH_2OH hydrogenation and CH_3OH sublimation becomes dominant

in the enhancement of gaseous CH_3OH with increasing T_k (t). As the maximum T_k (t) is reached, the preferred formation reactions include the $CH_3OH_2{}^+$ recombination at $n_{H_2\,(init)} = 10^3 - 10^4 cm^{-3}$ and the ion-neutral Rxn.(3-12)[95] at $n_{H_2\,(init)} = 10^5 - 10^6 cm^{-3}$. At the highest gas kinetic temperature point due to the shock heating, Rxn.(3-6) is preferred, except at $n_{H_2\,(init)} = 10^6\ cm^{-3}$ where it is undetectable. The radical-molecule reaction has a minimal impact on gaseous methanol production only at high initial gas volume densities ($n_{H_2\,(init)} = 10^5 - 10^6\,cm^{-3}$), low CRIR ($\zeta = 1 - 10\zeta_0$), and low $T_{k,init}$=10 and 50 K models at the shock's onset.

$$CH_3OH_2{}^+ + NH_3 \longrightarrow CH_3OH + NH_4{}^+. \tag{3-12}$$

There is a fundamental distinction between the two shock-velocity setups concerning the formation of gaseous methanol during the shock. In all of the shock models with v_{shock}=50 km/s, the radical-molecule route appears to play a negligible role or has no observable impact on gaseous CH_3OH formation.

During the shock, the dominant destruction pathways of gaseous methanol vary with v_{shock}. In low-velocity C-shock models that take place at $n_{H_2\,(init)} = 10^3 cm^{-3}$, the primary destructive reaction at the maximum $T_k\,(t)$ due to shock heating is Rxn.(3-3). At $n_{H_2\,(init)} = 10^4\,cm^{-3}$, Rxn.(3-3) is substituted by cosmic ray-induced photoreaction Rxn.(3-4), or neutral-neutral Rxn.(3-13)[42]. At $n_{H_2\,(init)} = 10^5\ cm^{-3}$, an increase in T_k (t) triggers Rxn.(3-10), while Rxn.(3-13) leads at the maximum T_k (t). Finally, at $n_{H_2\,(init)} = 10^6\ cm^{-3}$, Rxn.(3-5) cease, and CH_3OH condensation prevails. At the peak of the shock heating, Rxn.(3-10) takes over.

In high-velocity C-shocks with $n_{H_2\,(init)} = 10^3 - 10^4 cm^{-3}$, the ion-neutral Rxn.(3-10) becomes the dominant pathway of methanol depletion at the maximum T_k (t). At $n_{H_2\,(init)} = 10^5 - 10^6 cm^{-3}$, as $T_k(t)$ increase, the preferential pre-shock reaction is replaced at the maximum by Rxn.(3-10) (first half) and Rxn.(3-11) (second half), although at the shock's onset Rxn.(3-13) is also involved.

$$CH + CH_3OH \longrightarrow CH_3CHO + H. \tag{3-13}$$

As the shock wave propagates, there is a variation of $n_{H_2\,(t)}$ and T_k (t) that leads to different formation and destruction pathways at the beginning and end of the shock. In other words, the chemistry change in each epoch due to the dynamic chemical and thermodynamic processes during the propagation and dissipation of a shock wave.

Upon comparing the formation and destruction pathways in both schemes, it is possible that the abundance stability of gas-phase CH_3OH relies on the the successive formation

and destruction of CH_3CHO [Eqs.(3-6) and (3-13)], during the shock influence. Figure **3-10** illustrate a comparison of CH_3CHO abundance over time as a function of $n_{H_2\,(init)}$ in low-velocity C-shock models with $T_{k,init}$=10 K and $\zeta = 1\zeta_0$. This figure demonstrates that the abundance of CH_3CHO is comparable to that of gaseous CH_3OH (see Fig.**3-7**), albeit at a lower level by approximately one order of magnitude. Therefore, it is plausible that CH_3CHO is a significant reservoir of CH_3OH, particularly for $n_{H_2\,(init)}$ ranging from $10^5 - 10^6\,cm^{-3}$. The above path explains how the abundance of gas-phase methanol remains stable throughout the maximum $T_k\,(t)$ as the C-shock wave propagates.

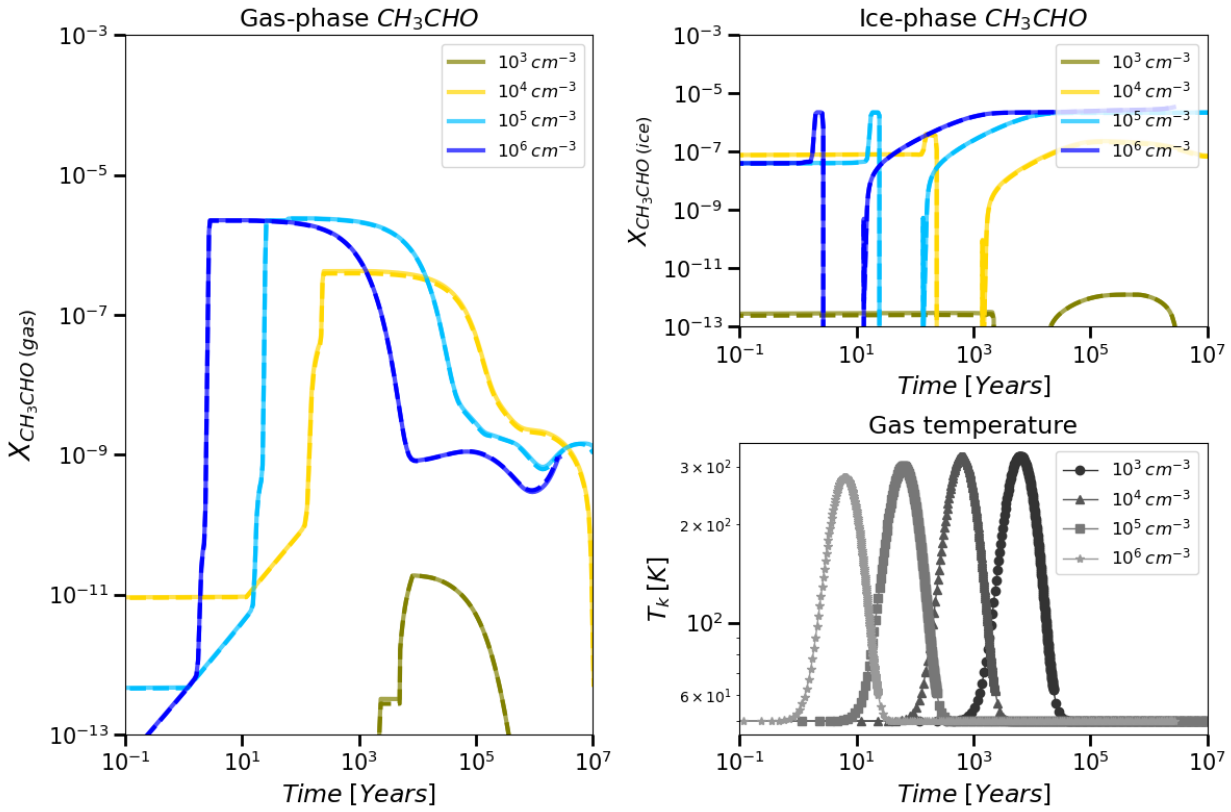

Figure 3-10.: Comparison of CH_3CHO abundance over time as a function of $n_{H_2\,(init)}$ at $n_{H_2\,(init)} = 10^3\ cm^{-3}$ (dark green), $n_{H_2\,(init)} = 10^4\ cm^{-3}$ (yellow), $n_{H_2\,(init)} = 10^5\ cm^{-3}$ (light blue) and $n_{H_2\,(init)} = 10^6\ cm^{-3}$ (dark blue) in low-velocity C-shock models with $T_{k,init}$=10 K and $\zeta = \zeta_0$. The dashed and solid lines correspond to the default and current schemes, respectively. The left panel shows the gas-phase CH_3CHO abundance, while the top right panel displays the ice-phase (grain surface + bulk) CH_3CHO abundance. The gas temperature evolution, $T_k\,(t)$, of each model is illustrated by the gray lines in the bottom right panel.

In summary, our models suggest that gas-phase methanol can track C-type shocks regardless of their velocity because its abundance increases significantly due to sputtering or sublimation of ice-dust grains as the shock wave propagates. In general, the abundance increase

of gaseous CH_3OH in non-shock scenarios is smaller compared to shock scenarios, where the increase ranges from 2 to 6 orders of magnitude depending on $n_{H_2\,(init)}$ and $T_{k,init}$. At each epoch there is a major formation reaction for the modeled gaseous CH_3OH. Therefore, the abundance and synthesis of gaseous CH_3OH is sensitive to shock conditions and shock-induced chemistry.

It is important to note that the primary distinction between the two schemes is the early appearance of the new reaction during the low-velocity C-shock wave and the increased significance of CH_2OH hydrogenation in the current scheme. It is noteworthy that the new reaction does not impact the pathways of gaseous methanol destruction.

3.1.2. Analysis upon reference molecules and the precursors of CH_3OH

Examination of reference molecules (H_2, CO and H_2O)

This section compares schemes using methanol (CH_3OH) and three common molecules: carbon monoxide (CO), hydrogen (H_2), and water (H_2O) in the gas phase. For this case, we use models 11 and 23 (see Table **A-1**), which are characterized by an initial gas volume density of $n_{H_2\,(init)} = 10^5\ cm^{-3}$, a standard CRIR, and an initial gas kinetic temperature, $T_{k,init}$, of 50 K. Models 11 and 23 were employed to illustrate the behavior of molecular species in low (v_{shock}=10 km/s) and high (v_{shock}=50 km/s)-velocity shocks, respectively.

Figure **3-11** shows the abundance evolution of these four molecules in model 11, while Figure **3-12** shows it in model 23. Both figures have brown, orange, and light blue lines corresponding to H_2O, H_2, and CO, respectively. Simultaneously, the dark blue lines depict the CH_3OH evolution considering the current (solid) and the default (dashed) schemes. The gas kinetic temperature evolution, $T_k\,(t)$, is represented by the dotted grey line, and the gas density evolution, $n_{H_2}\,(t)$, is represented by the dotted red line.

Concerning carbon monoxide, the amount of CO increases as $T_k\,(t)$ rises in both non-shock (Fig.**2-1**) and shock scenarios (Figs.**3-11** and **3-12**). As CO sublimation temperature is around ∼29 K [82], nearly all the CO is sublimated in the studied conditions regardless of the model physical scenario. Therefore, comparable maximum abundances are present in both Hot Core and C-shock models, concluding that CO may not function effectively as a C-shock tracer in these circumstances. However, the abundance of H_2 experiences a slight increase ($\sim 1 \times 10^{-1}$) as the shock wave propagates at a velocity of 10 km/s, in contrast to Hot Core models. It is worth noting that the behavior of H_2 is similar to that of CO, albeit the abundance of the two species are at different scales. When observing at v_{shock}=50 km/s, at high gas volume densities such as $n_{H_2\,(init)} = 10^5\ cm^{-3}$, the H_2 abundance greatly reduces to 10^{-9}, strongly indicating a destructive behaviour.

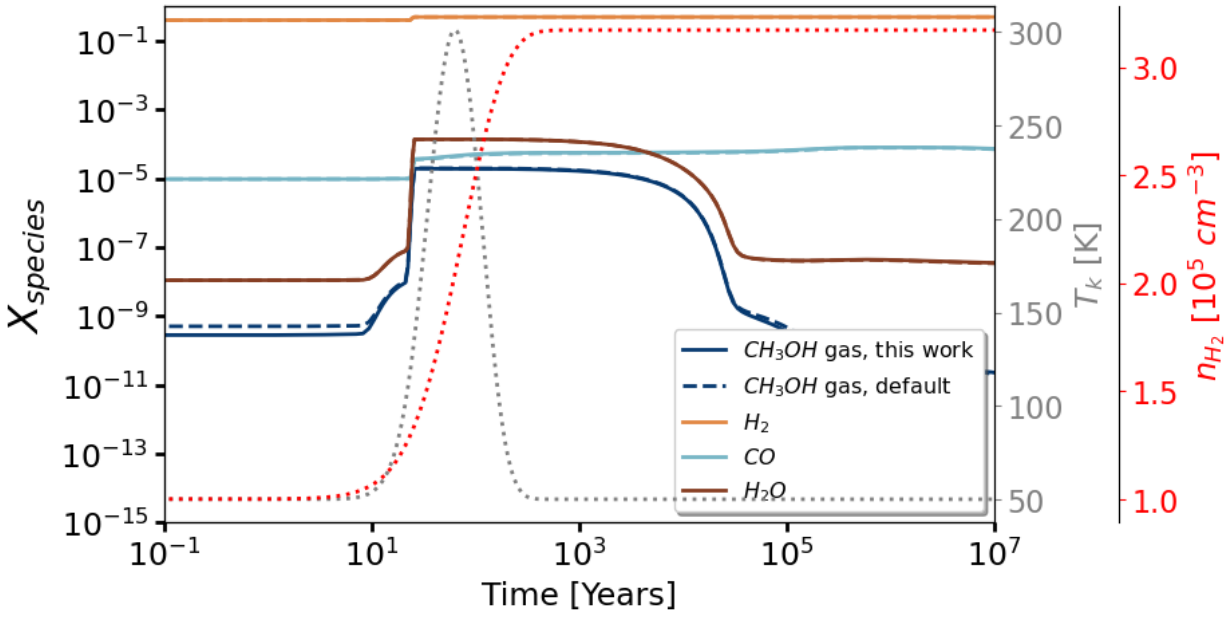

Figure 3-11.: Chemical abundances of H_2 (orange), H_2O (brown), CO (light blue), and CH_3OH (dark blue) in the gas phase over time for Model 11. The dashed and solid lines correspond to the default and current schemes, respectively. Gas temperature evolution, T_k (t), is depicted by the dotted grey line, while gas density evolution, n_{H_2} (t), is illustrated by the dotted red line.

Regarding water, in the Hot Core models (see Fig.**2-1** as an example), the abundance of H_2O remains nearly constant over time, with only minor variations. As mentioned in Section 1, water functions as a full-extension C-shock tracer at a speed of 10 km/s (see Fig.**3-11** as an example), resulting in a rise in abundance as the C-shock wave propagates. However, at v_{shock}=50 km/s (see Fig.**3-12** as an example), water is enhanced initially by the shock but is destroyed as the shock increases the temperature. As noted in Holdship *et al.* (2017) [36], both methanol and water demonstrate comparable capabilities in withstanding low-velocity shock waves without being destroyed in the hot regions of the post-shock gas. However, using UCLCHEM v.3.1[b], methanol remains unharmed at the maximum temperature of high-velocity shocks, which distinguishes it from water.

It is noteworthy that the schemes show no changes in the abundances of the reference molecules. As expected, the newly added radical-molecule route does not significantly affect the abundance evolution of H_2, CO, and H_2O in both c-shock models, at least in a first-order sense.

[b]Refer to online documentation for differences between the UCLCHEM version used in this work and the version used in Holdship *et al.* (2017)[36]

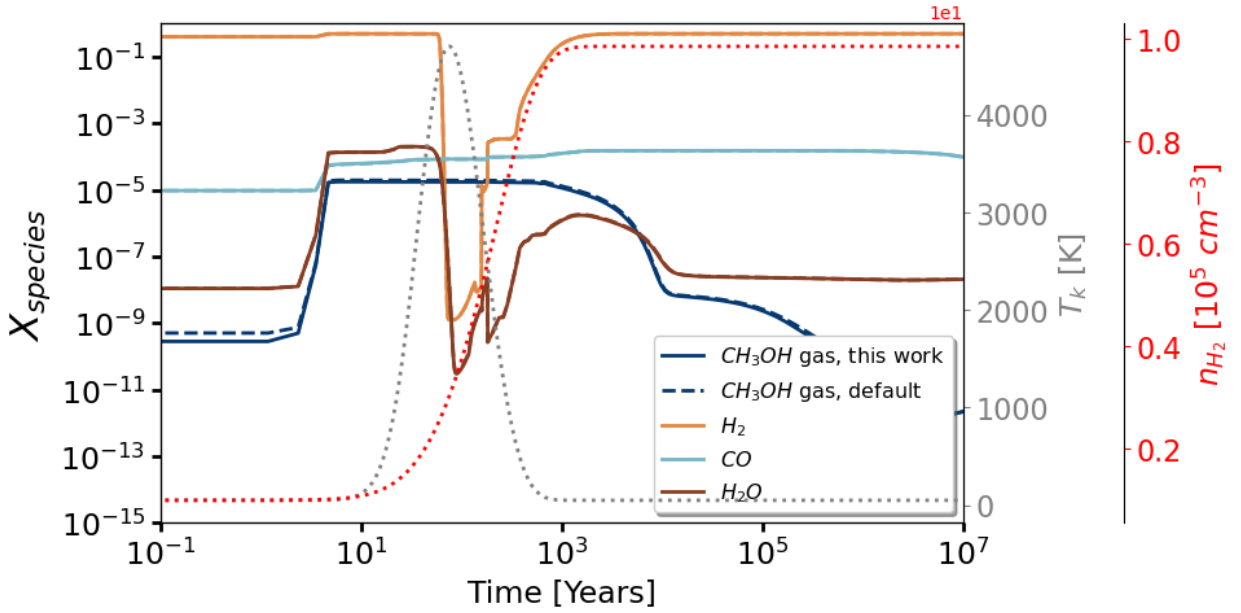

Figure 3-12.: Chemical abundances of H_2 (orange), H_2O (brown), CO (light blue), and CH_3OH (dark blue) in the gas phase over time for Model 23. The dashed and solid lines correspond to the default and current schemes, respectively. Gas temperature evolution, T_k (t), is depicted by the dotted grey line, while gas density evolution, n_{H_2} (t), is illustrated by the dotted red line.

Examination of the precursors to CH_3OH

The chemical analysis shows how sublimation and sputtering removal from the ice-dust grain affect the levels of H_2, CO, and water in the gas phase. Now, it is important to discuss the behavior of the gaseous formyl radical (HCO), formaldehyde (H_2CO) and methoxyl radical (CH_3O) as they are the precursors of CH_3OH in the formation of methanol via the overall CO hydrogenation mechanism.

Formyl radical (HCO) HCO is an intermediate in the overall CO hydrogenation mechanism to form methanol and is also a byproduct in the radical-molecule route. This byproduct can be hydrogenated again to form H_2CO, which replenishes the chemical network [75].

In Figure **3-13** it is shown a comparison of the gaseous formyl radical abundance at different $n_{H_2\,(init)}$ over time in Hot Core models with T_{HC}=50 K and $\zeta = \zeta_0$. This figure illustrates that the prevalence of gaseous formyl radicals in non-shock models is predominantly influenced by $n_{H_2\,(init)}$. At $n_{H_2\,(init)} = 10^3 - 10^4\ cm^{-3}$, the abundance of formaldehyde remains nearly constant. Nevertheless, at $n_{H_2\,(init)} = 10^6\ cm^{-3}$, the abundance of HCO experiences a notable increase from 10^{-14} to 10^{-9} with the rise in T_k (t).

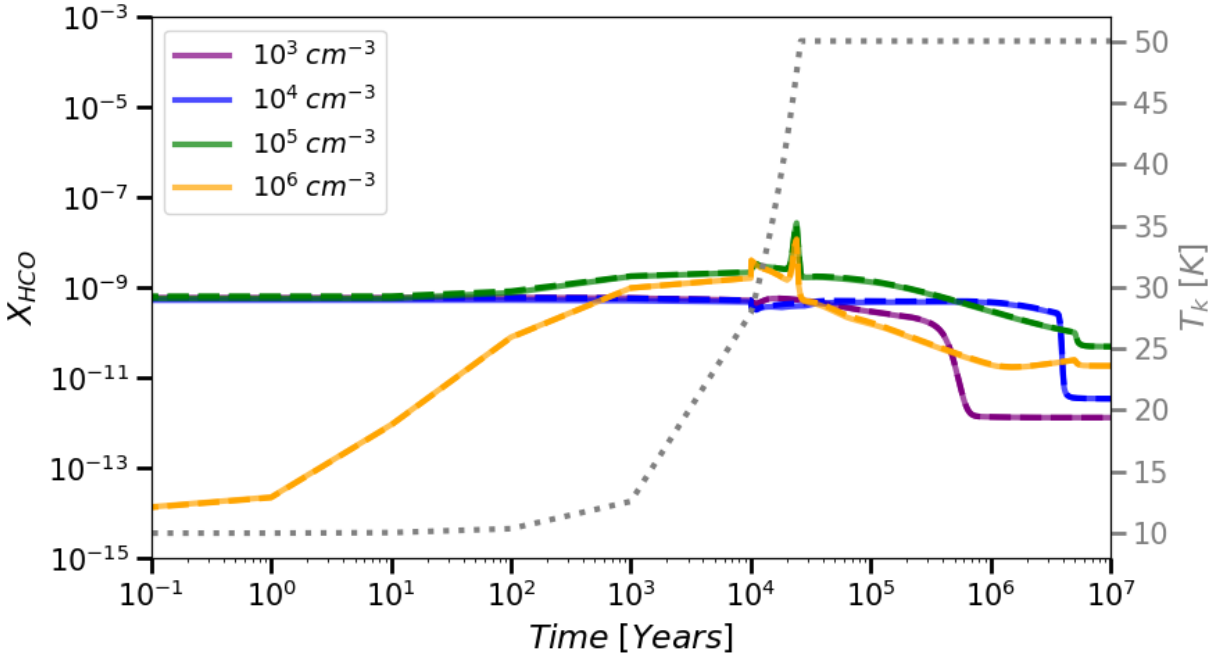

Figure 3-13.: Comparison of the gaseous formyl radical abundance at different $n_{H_{2\,(init)}}$ ($10^3\ cm^{-3}$ in purple, $10^4\ cm^{-3}$ in blue, $10^5\ cm^{-3}$ in green and $10^6\ cm^{-3}$ in yellow) over time in Hot Core models with T_{HC}=50 K and $\zeta = \zeta_0$. The dashed and solid lines correspond to the default and current schemes, respectively. The gas temperature evolution, $T_k\,(t)$, is shown by the dashed gray line.

Figure 3-14 contrasts formyl radical abundance over time among shock and non-shock scenarios using $n_{H_{2\,(init)}} = 10^5\ cm^{-3}$, $T_{k,init}$ (or T_{HC})=50 K, and $\zeta = \zeta_0$ as an example. The behavior of the HCO radical is highly reactive when exposed to shocks. However, as shown in Figure 3-14, the gaseous HCO is initially enhanced by more than two orders of magnitude due to the shock influence, but is subsequently destroyed as the $T_k\,(t)$ increases due to shock heating. The extent of destruction depends on the velocity of the shock wave, decreasing by more than four orders of magnitude at v_{shock} =10 km/s and by more than seven orders of magnitude at v_{shock} =50 km/s. Thus, it possible that the decrease of gas-phase HCO can be an indicator for destruction under different shock conditions based on the above discussion.

Formaldehyde (H_2CO) H_2CO is not only an immediate precursor of methanol in the radical-molecule H-atom abstraction route but also has potential in probing gas temperature [53].

In Figure 3-15 it is shown that the evolution of the gaseous formaldehyde abundance through the non-shock models is also primarily affected by $n_{H_{2\,(init)}}$. The formaldehyde abundance decrease with time at initial low gas volume densities, such as $n_{H_{2\,(init)}} = 10^3\ cm^{-3}$, while

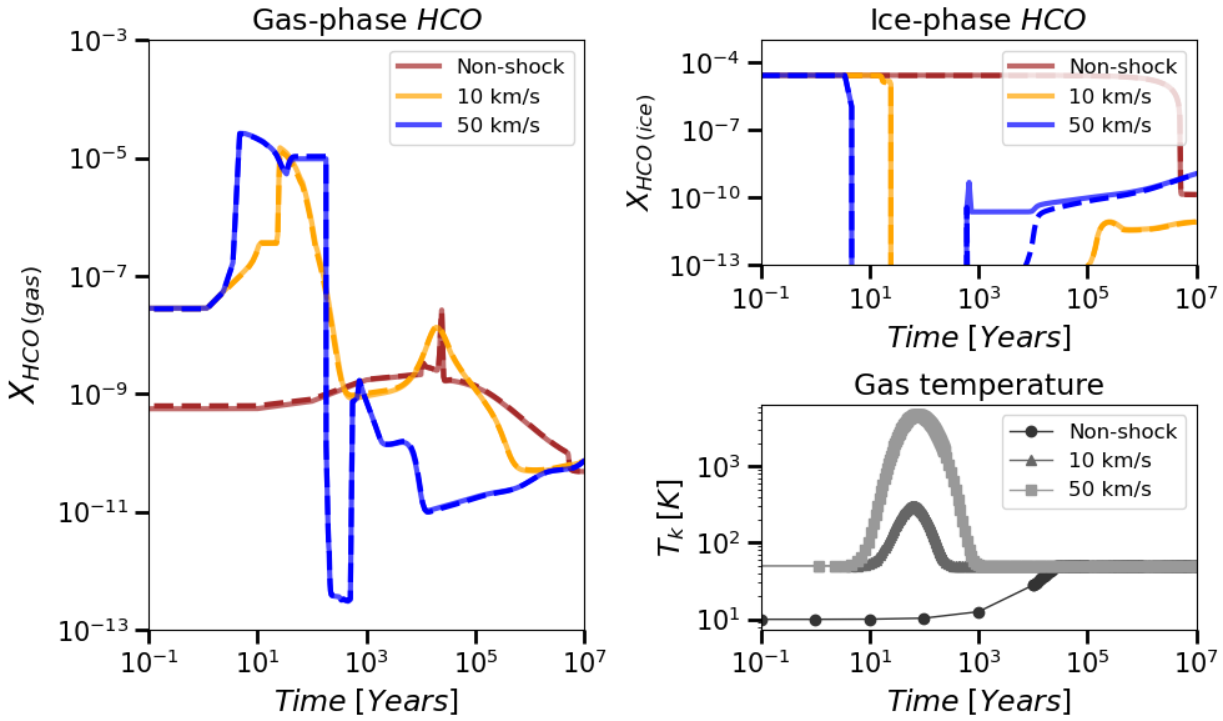

Figure 3-14.: Comparison of formyl radical abundance over time as a function of shock wave velocity in non-shock (red), low-velocity (blue), and high-velocity C-shock (yellow) models with $n_{H_2\,(init)} = 10^5\,cm^{-3}$, $T_{k,init}$ (or T_{HC})=50 K, and $\zeta = \zeta_0$. The dashed and solid lines correspond to the default and current schemes, respectively. The left panel shows the gas-phase methanol abundance, while the top right panel displays the ice-phase (grain surface + bulk) methanol abundance. The gas temperature evolution, $T_k\,(t)$, of each model is illustrated by the gray lines in the bottom right panel.

at high initial volume gas densities, such as $n_{H_2\,(init)} = 10^6\,cm^{-3}$, the H_2CO abundances increase significantly from 10^{-14} to 10^{-7} with increasing $T_k\,(t)$. This is anticipated as gaseous formaldehyde is, in part, produced through the sublimation of H_2CO, wherein the formation of solid-state H_2CO is enhanced in the presence of hydrogen (refer to Section 3.2.2).

Figure **3-16** illustrates a comparison of formaldehyde abundance over time, correlating it with v_{shock} in both non-shock and shock models. The conditions include $n_{H_2\,(init)} = 10^5\,cm^{-3}$, $T_{k,init}$ (or T_{HC})=50 K, and $\zeta = \zeta_0$. At a shock velocity of 10 km/s, gaseous H_2CO is enhanced by the shock and trace its full extent. However, in models with $n_{H_2\,(init)} = 10^3\,cm^{-3}$ and $\zeta = 100\zeta_0$, gaseous H_2CO is enhanced initially by the shock, but destroyed as the shock increases the gas kinetic temperature. When v_{shock}=50 km/s, in all models, formaldehyde is initially enhanced by the shock, but is then destroyed as the shock raises $T_k\,(t)$. Interestingly, we can identify C-shock velocities by examining the behavior of methanol and formaldehyde. Formaldehyde serves as a shock tracer when destroyed at high shock velocities, while

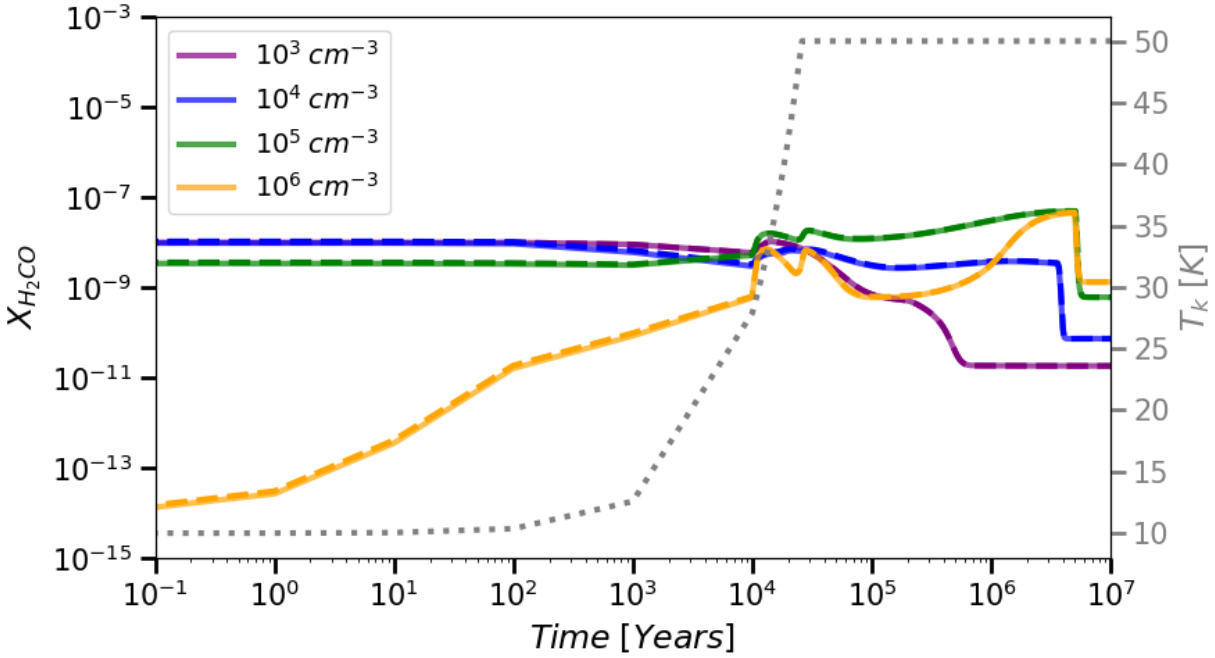

Figure 3-15.: Comparison of the gaseous formaldehyde abundance at different $n_{H_{2\,(init)}}$ ($10^3\ cm^{-3}$ in purple, $10^4\ cm^{-3}$ in blue, $10^5\ cm^{-3}$ in green and $10^6\ cm^{-3}$ in yellow) over time in Hot Core models with T_{HC}=50 K and $\zeta = \zeta_0$. The dashed and solid lines correspond to the default and current schemes, respectively. The gas temperature evolution, $T_k\ (t)$, is shown by the dashed gray line.

methanol is enhanced by the shock and traces its full extent.

Low-velocity C-shock models show significant contrast between the default and current schemes. In particular, the default scheme produces an abundance of two orders of magnitude higher than the current one. The discrepancy is due to the introduction of the radical-molecule H-atom abstraction pathway and changes in the branching ratios associated with each step of the CO hydrogenation mechanism in the solid state (refer to Section 3.2.2). In addition, and of critical importance, the observed abundance ratio of H_2CO/CH_3OH might distinguish between methanol formation pathways in low-velocity shocked environments. The difference in formaldehyde abundance between each scheme is significant enough to determine which formation pathway is predominant under these conditions.

Methoxyl radical (CH_3O) CH_3O is an immediate precursor in both the radical-molecule H-atom abstraction route and the CH_3O hydrogenation reaction to form CH_3OH.

Figure **3-17** exhibits a comparison in gaseous methoxyl radical abundance over time, considering various initial gas volume densities ($n_{H_{2\,(init)}}$) in Hot Core models with T_{HC}=50 K

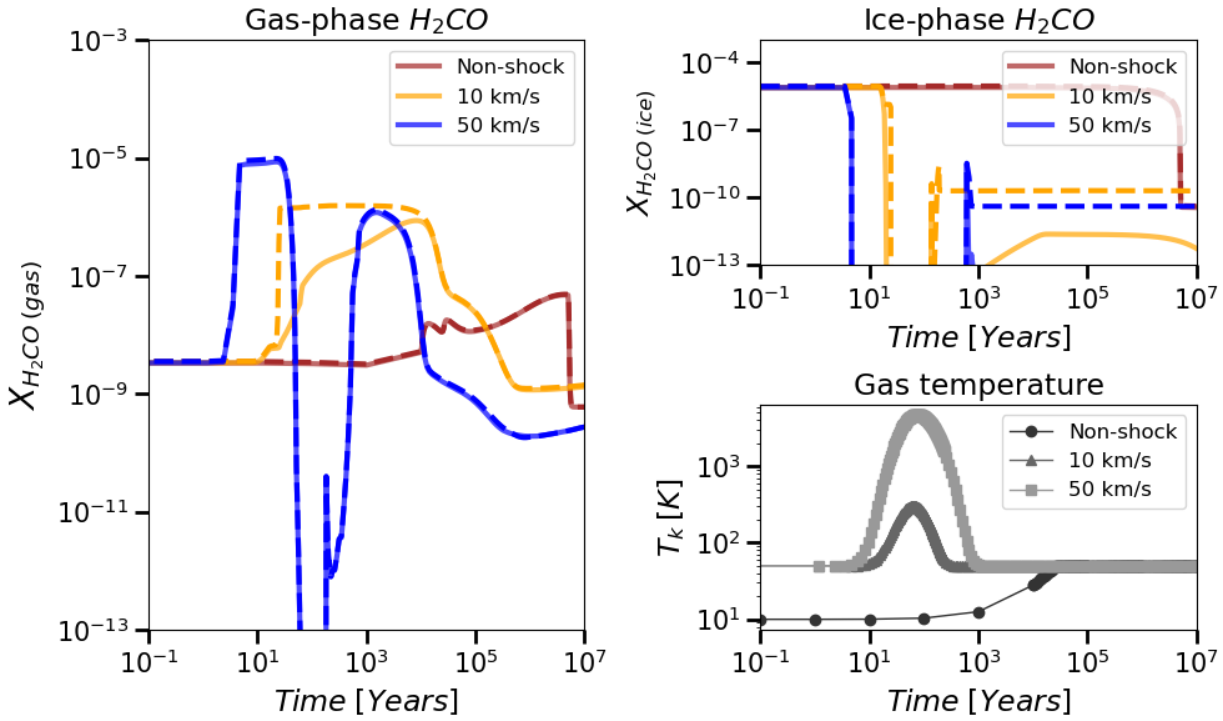

Figure 3-16.: Comparison of formaldehyde abundance over time as a function of shock wave velocity in non-shock (red), low-velocity (blue), and high-velocity C-shock (yellow) models with $n_{H_2\,(init)} = 10^5\,cm^{-3}$, $T_{k,init}$ (or T_{HC})=50 K, and $\zeta = \zeta_0$. The dashed and solid lines correspond to the default and current schemes, respectively. The left panel shows the gas-phase methanol abundance, while the top right panel displays the ice-phase (grain surface + bulk) methanol abundance. The gas temperature evolution, $T_k\,(t)$, of each model is illustrated by the gray lines in the bottom right panel.

and $\zeta = \zeta_0$. In contrast, Figs. 3-18 and 3-19 illustrate the variation in CH_3O abundance over time, correlating it with shock wave velocity in both non-shock and shock models with $n_{H_2\,(init)} = 10^5\,cm^{-3}$, $T_{k,init}$ (or T_{HC})=50 or 100 K, and $\zeta = \zeta_0$. In non-shock scenarios, the abundance of gaseous CH_3O increases with increasing $n_{H_2\,(init)}$ and T_{HC} (see Fig. 3-17). Similarly, the abundance increases as the shock wave propagates at both velocities in C-shock models (see Fig. 3-18). As seen, the highest CH_3O abundance remains similar in both shock and non-shock models, suggesting that the methoxyl radical is not a suitable C-shock tracer.

As shown in Figs.3-18 and 3-19, the difference between schemes is noticeable. Generally, the default scheme exhibits lower levels of CH_3O abundance. However, at $T_{k,init}$ =100 K and $n_{H_2\,(init)} = 10^5 - 10^6\,cm^{-3}$, a notable contrast arises (see Fig. 3-19). In the default scheme, the CH_3O abundance remains constant, while in the current one, the methoxyl radical abundance drops following the shock wave propagation.

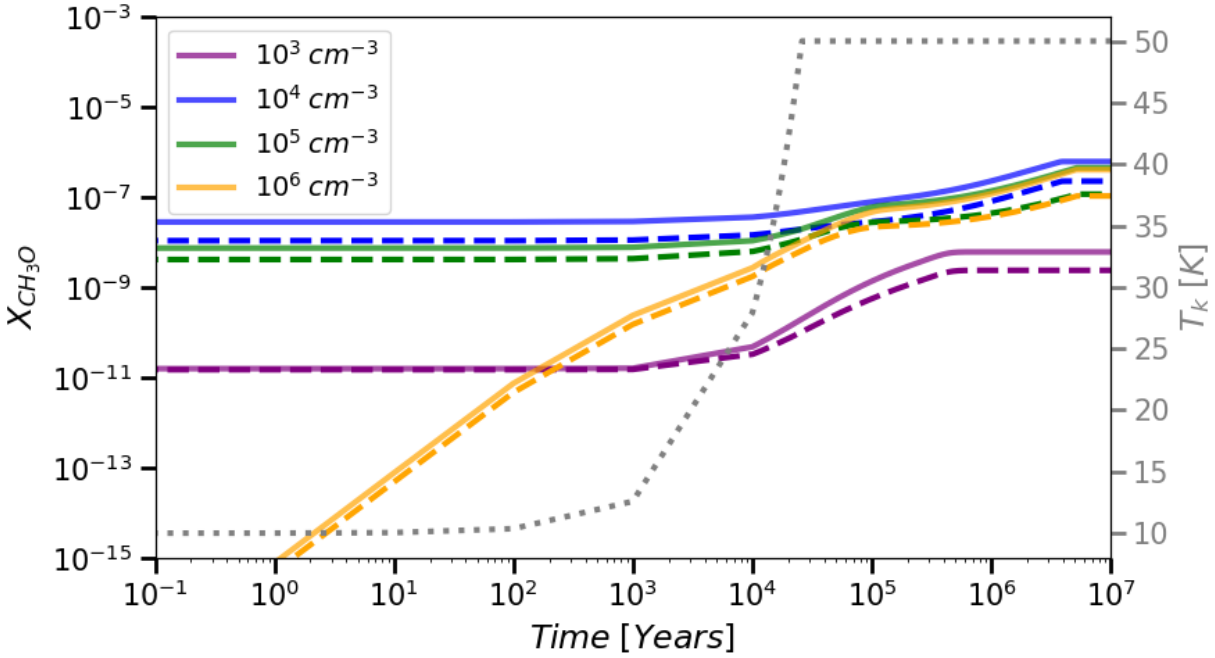

Figure 3-17.: Comparison of the gaseous methoxyl radical abundace at different initial gas volume densities ($n_{H_2\,(init)} = 10^3\ cm^{-3}$ in purple, $n_{H_2\,(init)} = 10^4\ cm^{-3}$ in blue, $n_{H_2\,(init)} = 10^5\ cm^{-3}$ in green and $n_{H_2\,(init)} = 10^6\ cm^{-3}$ in yellow) over time in Hot Core models with T_{HC}=50 K and $\zeta = \zeta_0$. The dashed and solid lines correspond to the default and current schemes, respectively. The gas temperature evolution, $T_k\,(t)$, is shown by the dashed gray line.

The introduction of the radical-molecule route appears to have a stronger influence on the abundance of HCO, H_2CO, and CH_3O than on the abundance of methanol. This will be further discussed in Section 3.2.2, as changes in the chemical network primarily occur in the solid-state phase.

3.1.3. Contrast with ALMA observations

As previously stated in Chapter 1 and Section 2.2, the primary distinction between the gas conditions and CRIR regimes in the CND and SB-ring regions of NGC 1068 is that the gas volume density is higher in the CND ($n_{H_2} = 10^{5-6}\ cm^{-3}$) than in the SB ring ($n_{H_2} = 10^{3-4}\ cm^{-3}$), while the opposite is true for the CRIR - $\zeta = 1 - 10\zeta_0$ for the CND and $\zeta = 1 - 100\zeta_0$ for the SB-ring. In the present Section, we compare our models with the multi-linear molecular study conducted by Huang *et al.* (submitted) [37]. We will assess the consistency between our results and their findings. This comparison aims to determine the physical origin of the observed methanol abundance.

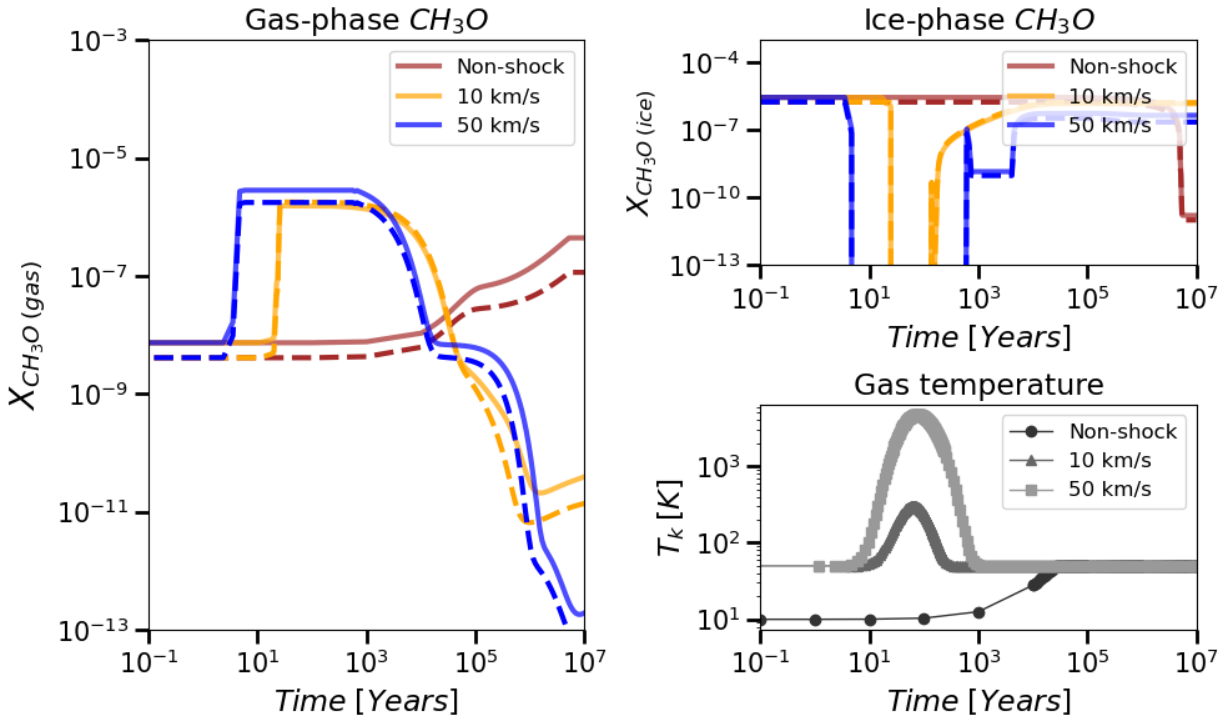

Figure 3-18.: Comparison of methoxyl radical abundance over time as a function of shock wave velocity in non-shock (red), low-velocity (blue), and high-velocity C-shock (yellow) models with $n_{H_2\,(init)} = 10^5\,cm^{-3}$, $T_{k,init}$ (or T_{HC})=50 K, and $\zeta = \zeta_0$. The dashed and solid lines correspond to the default and current schemes, respectively. The left panel shows the gas-phase methanol abundance, while the top right panel displays the ice-phase (grain surface + bulk) methanol abundance. The gas temperature evolution, $T_k\,(t)$, of each model is illustrated by the gray lines in the bottom right panel.

CND of NGC 1068

Huang *et al.* (submitted) [37] conducted high-resolution ALMA observations (0.5-0.8 arcseconds, corresponding to 35-56 parsecs at a distance of 14 megaparsecs) of the CND in NGC 1068, analyzing A- and E- CH_3OH transitions. The authors used non-LTE radiative transfer analysis and Bayesian inference to determine the column density of CH_3OH and the temperature and density of the molecular gas in the CND, utilizing CH_3OH as a tracer.

As previously mentioned, the $T_{k,init}$ (or T_{HC}) and $n_{H_2\,(init)}$ used in all models were derived from their multi-line molecular analysis in NGC 1068 in each regions. The molecular column densities of both A- and E-CH_3OH isomers were deemed to be well constrained within the CND, where the inferred column densities of A- and E-CH_3OH both lie within the range of $10^{15-16}\,cm^{-2}$. We used Eq.(3-14) from Huang & Viti. (2023) [39] to determine the observed CH_3OH abundances, $X_{CH_3OH,obs}$. In this equation, Δz_{cloud} is the line-of-sight dimension of

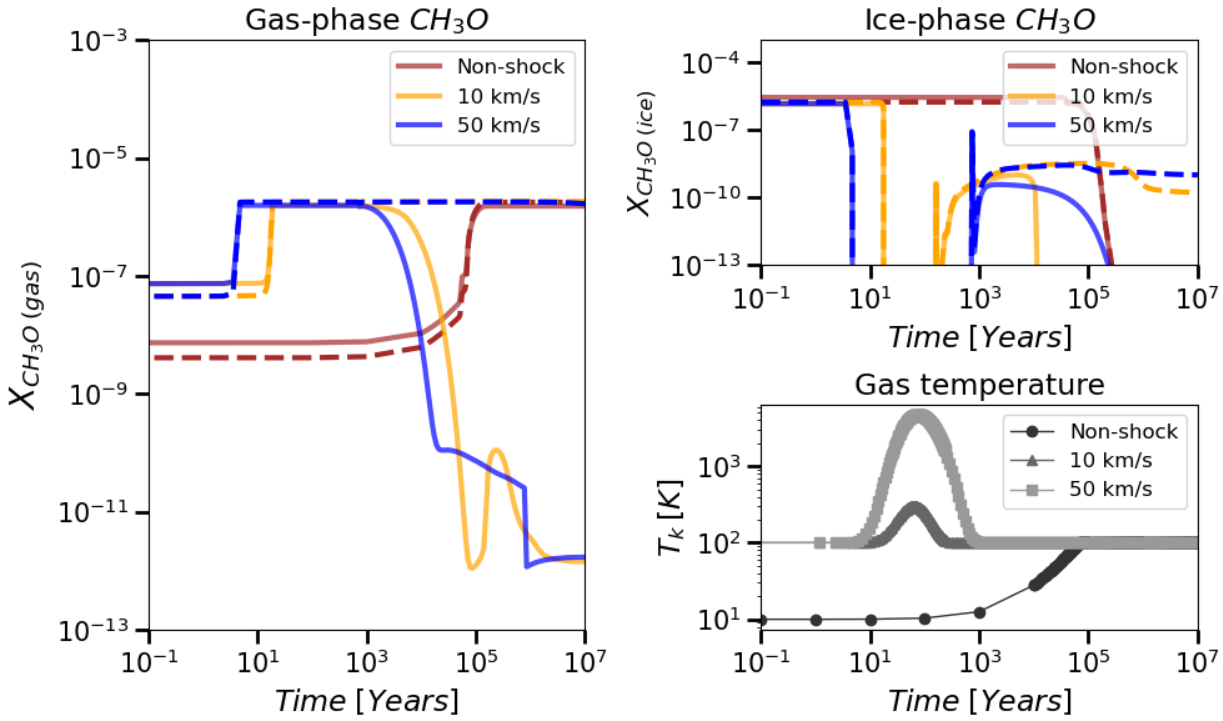

Figure 3-19.: Comparison of methoxyl radical abundance over time as a function of shock wave velocity in non-shock (red), low-velocity (blue), and high-velocity C-shock (yellow) models with $n_{H_2\,(init)} = 10^5\,cm^{-3}$, $T_{k,init}$ (or T_{HC})=100 K, and $\zeta = \zeta_0$. The dashed and solid lines correspond to the default and current schemes, respectively. The left panel shows the gas-phase methanol abundance, while the top right panel displays the ice-phase (grain surface + bulk) methanol abundance. The gas temperature evolution, $T_k\,(t)$, of each model is illustrated by the gray lines in the bottom right panel.

the gas component under consideration, θ_{beam} is the beam size of the observation, and η_{ff} is the beam filling factor, which is a parameter describing the size of the source relative to the beam size. We use the same approximation as Huang & Viti. (2023) [39] where θ_{beam} is used as an estimate of the line-of-sight dimension of the gas component (Δz_{cloud}), and 1.0 as the upper limit for η_{ff}.

$$X_{species,obs} = \frac{N_{species}}{n_{H_2}\,\Delta z_{cloud}\,\eta_{ff}} \sim \frac{N_{species}}{n_{H_2}\,\theta_{beam}\,\eta_{ff}} \geq \frac{N_{species}}{n_{H_2} \times \theta_{beam} \times 1.0}. \tag{3-14}$$

For the E-CH_3OH isomer, the range is from $\geq 2.5 \times 10^{-11}$ for R1, $\geq 1.2 \times 10^{-12}$ for R2, $\geq 2.4 \times 10^{-11}$ for R3, and $\geq 1.1 \times 10^{-11}$ for R4. For the A-CH_3OH isomer, we go from $\geq 1.8 \times 10^{-11}$ for R1, $\geq 1.9 \times 10^{-12}$ for R2, $\geq 1.2 \times 10^{-11}$ for R3, and $\geq 6.8 \times 10^{-12}$ for R4. Given that all inferred gas densities indicate about $10^6\,cm^{-3}$ throughout the entire

CND, which is consistent with indications of low inferred temperatures ($\leq 100K$), albeit not well-constrained, we compared observed abundances with models based on a initial gas volume density of $n_{H_2\,(init)} = 10^6\,cm^{-3}$. It is noteworthy that our models do not allow for the differentiation between A- and E-CH_3OH isomers. Therefore, we made use of the minimum value obtained from both isomers and all the regions studied within the CND.

In Figure **3-20** we present the chemical abundances as a function of time for Hot Core (top panel), slow C-shock (middle panel) and high C-shock (bottom panel) models in the CND ($n_{H_2\,(init)} = 10^6\,cm^{-3}$). The gray dashed curve represents the evolution of $T_k\,(t)$, while the black dotted horizontal line indicates the lower limit of the species fractional abundances derived from Huang *et al.* (submitted) [37]. Although gaseous methanol abundance is increased significantly under the influence of a shock wave, regardless of its velocity, CH_3OH can also be enhanced through the thermal sublimation of ices caused by events as star formation processes, surpassing the observed minimum limit. Therefore, it is important to exercise caution in drawing conclusions regarding CH_3OH abundance origin, as it may increase in a warm gas environment without shocks, particularly in high $n_{H_2\,(init)}$ and low CRIR regimes.

Huang & Viti. (2023) [39] compares their results with those of Huang *et al.* (2022) [38] with respect to SiO (high-shock tracer) and HNCO (slow-shock tracer) observations in the NGC 1068 CND's. Compared to HNCO, which mapped a larger but weaker shocked area, SiO analyzed the gas layer(s) that underwent a more striking shock. With respect to the spatial distribution of CH_3OH, it is concentrated similarly to SiO, as noted by Huang *et al.* (2022) [38]. When analyzing the gas density and temperature, it is apparent that CH_3OH is tracing gas components with similarly gas density and cold temperatures ($T_k < 50K$), much like HNCO. The low measured temperature, $T_k < 100K$, may be attributed to both shocks given that this temperature could result from a complete post-shock cooling of a gaseous component in both scenarios and still leading to a methanol abundance that is consistent with observational data. As a result, the chemical origin of the observed CH_3OH could arise from both fast and slow C-shocks.

SB ring of NGC 1068

The results from Vroom *et al.* (in prep), via private communication, indicate a drop in gas density within the SB ring's arms (SB-S and SB-N regions) when compared to CND, specifically at $n_{H_2} = 10^{3-4}\,cm^{-3}$. This discovery aligns with Scourfield *et al.* (2020) [77] research, which disclosed a comparable gas density ($n_{H_2} \sim 10^4\,cm^{-3}$). We decided to estimate the observed abundance of CH_3OH in these areas based on the initially calculated column densities ($\log N_{CH_3OH} = 15.80^{+0.57}_{-0.83}$ for SB-N and $\log N_{CH_3OH} = 14.85^{+1.18}_{-0.20}$ for SB-S), thus obtaining a range of $X_{CH_3OH,obs}$ between $\geq 3.7 \times 10^{-9}$ for SB-N and $\geq 4.1 \times 10^{-10}$ for SB-S regions, assuming the same beam size as the CND. Similar as in Figure **3-20**, Figure **3-21** present the chemical abundances as a function of time and C-shock velocity, but with a pre-shock gas density of $n_{H_2\,(init)} = 10^4\,cm^{-3}$. The models presented in this Figure are associated

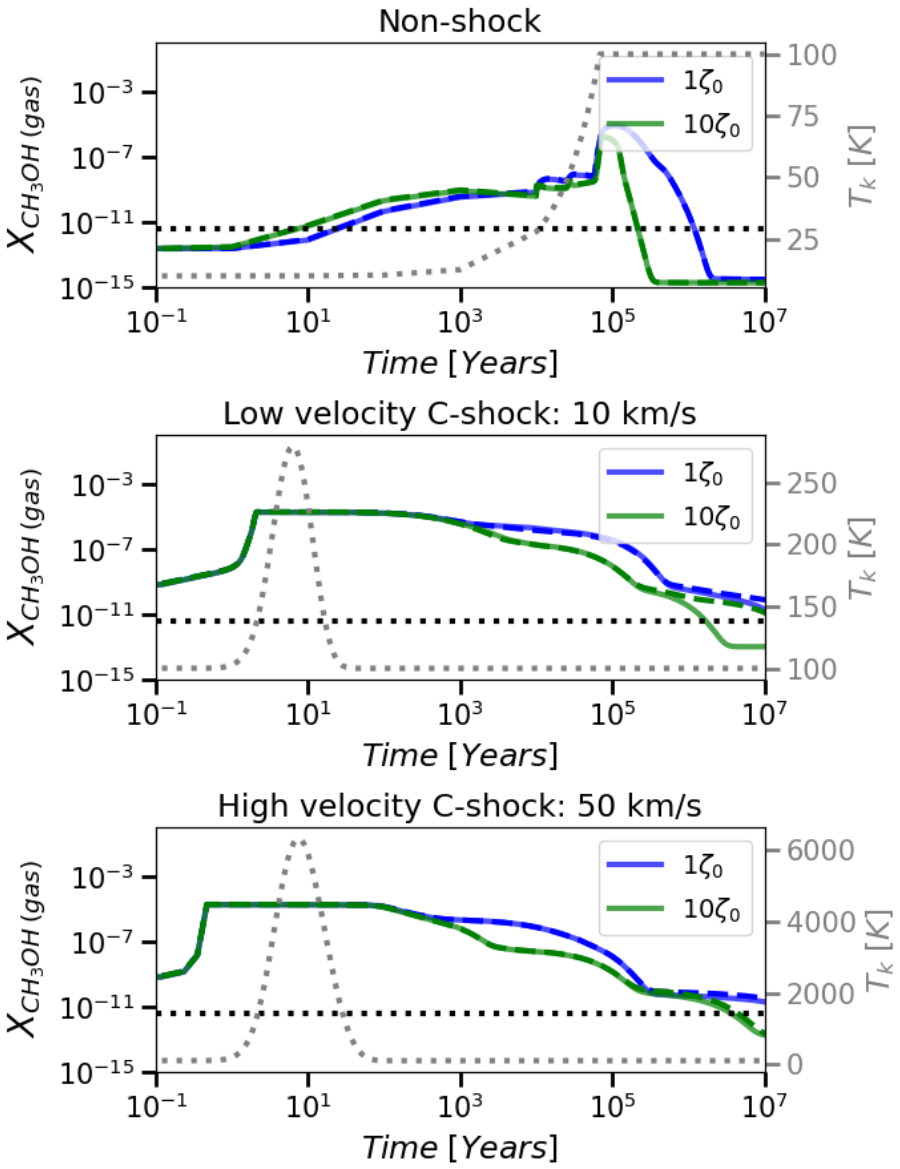

Figure 3-20.: Chemical abundances as a function of time for Hot Core (top panel), slow C-shock (middle panel) and high C-shock (bottom panel) models. The pre-shock gas density, $n_{H_{2\,(init)}}$, in the models is $10^6\ cm^{-3}$. The black dotted horizontal line indicates the lower limit of the species fractional abundances derived from Huang *et al.* (submitted) [37].

with the most representative conditions for the SB-ring regions.

As we mentioned before, Scourfield *et al.* (2020) [77] data reveals that the SB-ring of NGC 1068 exhibits a lower gas kinetic temperature compared to its CND. However, this finding could not be verified due to the lack of enough CH_3OH transitions in both regions. This means gas temperature traced by CH_3OH unfortunately cannot be well constrained. By

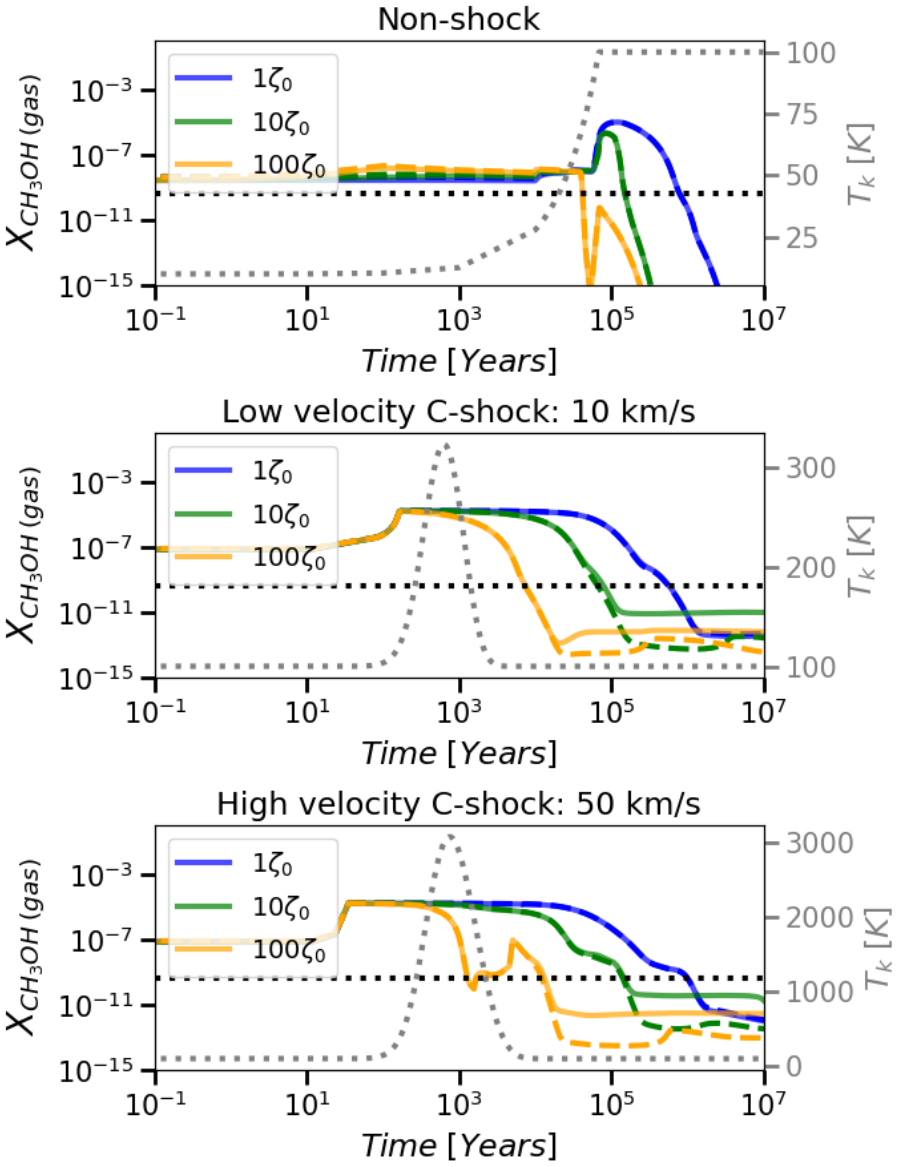

Figure 3-21.: Chemical abundances as a function of time for Hot Core (top panel), slow C-shock (middle panel) and high C-shock (bottom panel) models. The pre-shock gas density, $n_{H_2\,(init)}$, in the models is $10^4\,cm^{-3}$. The lower limit of the species fractional abundances derived from Vroom *et al.* (in prep), via private communication.

only considering $n_{H_2\,(init)}$ and CRIR, Figure **3-21** demonstrates that CRIR levels significantly affect methanol abundance at low $n_{H_2\,(init)}$; where high CRIR values correlate with reduced methanol levels, regardless of shock velocity. In these conditions, it is also noticeable that both shock and non-shock models could account for the minimum observed abundance. However, at low $n_{H_2\,(init)}$, the increase due to thermal desorption is considerable lower, and therefore, in regimes of low gas kinetic temperature and high CRIR, an origin derived from

the presence of a shock is more plausible.

Regarding possible differences in the origins of shock velocities across regions, Huang & Viti. (2023) [39] conducted a study on the outflow velocities of AGN-driven and starburst-driven outflows. The authors concluded that both outflow velocities are relatively similar and can induce fast and slow shocks within their respective spheres of influence. Huang & Viti. (2023) [39] also evaluated multiple chemical modellings, including Holdship *et al.* (2017) work. Their study ultimately concludes that it is uncertain whether CH_3OH solely indicates slow and non-dissociative shocks, or if CH_3OH abundance can be increased in both fast and slow shock scenarios. Our results are consistent with these previous investigations, and it shows that shocks can substantially enhance the gas-phase abundance of CH_3OH, regardless of the C-shock wave velocity and the methanol formation scheme employed. In this sense, the consideration of the radical-molecule route in the chemical network does not affect the ability of CH_3OH to trace C-shocks. This is because in both schemes, the increase in gaseous CH_3OH abundance is achieved by releasing CH_3OH from a solid state into the gas phase through sublimation and sputtering.

Further investigation is necessary to properly determine the gas conditions in the CND and SB ring of NGC 1068 by observing more rotational transitions of C-shock tracer species. The feasibility of measuring precise gas volume density and gas kinetic temperature can be established by implementing formaldehyde as a C-shock tracer. Chemical modeling can be used to compare with observations of CH_3OH, H_2CO, HNCO, and SiO to confirm the existence of shocks, their velocity levels, and duration after the most recent shock episode using each shock tracer. This approach can provide valuable insights into the nature of the shocks and their effects on the surrounding environment.

3.2. Interstellar Methanol Formation in Ice Grains

3.2.1. Methanol abundance and synthesis in solid state

This Section presents a detailed analysis of the behavior and formation pathways of solid-state methanol, both on the surface and in the inner layers (bulk) of the icy-dusty grain, in scenarios with and without the influence of a C-shock wave. The aim of this analysis is to determine the influence of the newly implemented radical-molecule H-atom abstraction route of methanol formation from the chemical point of view using UCLCHEM. We will also investigate how the newly implemented route change the chemistry, specially in shock-influenced environments.

Figure **3-22** show the chemical abundances of ice-phase methanol as a function of time in non-shock and shock models with $n_{H_2\,(init)} = 10^5\ cm^{-3}$ and $T_{HC} = 100K$. As previously stated, in non-shock scenarios, the abundance of methanol in the ice remains stable throughout the

model. Any decrease observed as $T_k\,(t)$ stabilizes is attributed to the incidence of cosmic rays or thermal desorption. However, when a C-shock wave is present regardless of its velocity, there is a significant decrease in the abundance of the ice-phase as the shock wave propagates. The destruction of ice layers during the propagation of the C-shock wave results in the release of methanol from the solid to the gas phase (see Figure **3-4** in Section 3.1.1), leading to a significant decrease in solid-state methanol abundance.

UCLCHEM deals with the surface and inner layers (bulk) of the icy-dusty grain separetely using a three-phase network. The following subsections analyze each layer and the differences between the most important reactions at different time steps.

Grain-surface phase

The grain surface is the outermost layer of a grain and is crucial for various chemical processes. This interphase enables the release of different chemical species into the surrounding gas phase. This is also the part from which gas-phase reactants are also frozen onto.

In Hot Core Models The evolution of surface methanol abundance in non-shock scenarios is depicted in Figure **3-23**. No significant changes in methanol abundance are seen with increasing T_k (t) under SB-Ring conditions (T_{HC}=100 K, $n_{H_2\,(init)}$ = 10^3 cm^{-3} and ζ = $1-100\zeta_0$). However, under CND conditions (T_{HC}=100 K, $n_{H_2\,(init)}$ = 10^6 cm^{-3} and ζ = $1-10\zeta_0$), there is a gradual increase of three to four orders of magnitude until T_{HC} is reached. In both CND and SB-ring conditions, surface methanol is primarily formed through the hydrogenation of CH_3O and CH_2OH, as described in Rxns.(3-15)[78] and (3-16)[78]. These H-atom addition routes are promoted with a higher H-atom flux to the surface, allowing the accreted H-atoms to diffuse and react with both CH_3O and CH_2OH species. Methanol synthesis through CH_3O or CH_2OH hydrogenation is a process that has no barriers [75], making it ideal for enhancing methanol production at such low temperatures. However, the formation of CH_2OH (Rxn (3-17)[78]) has a higher activation barrier than that of CH_3O formation (Rxn (3-18)[78]) (refer to Table **2-1** and Hidaka *et al.* (2009) [34]). As a result, Rxn.3-16 occurs as the gas temperature increases due to protostar core heating when the lifetime of CH_2OH is sufficiently high, even though it is barrierless.

Once $T_k(t) = T_{HC}$, the condensations of gaseous CH_3OH and $CH_3OH_2{}^+$ (Rxn.(3-19)[c]) ascribe to the surface methanol formation as freeze-out is faster than CH_3O hydrogenation at this time period. Regarding destruction, UV rays usually destroy methanol until T_k (t) >30 K, at which point it moves from the surface to the inner layers. CH_3OH_{surf} sublimation occurs once T_k (t) reaches ∼100 K.

[c] See online documentation.

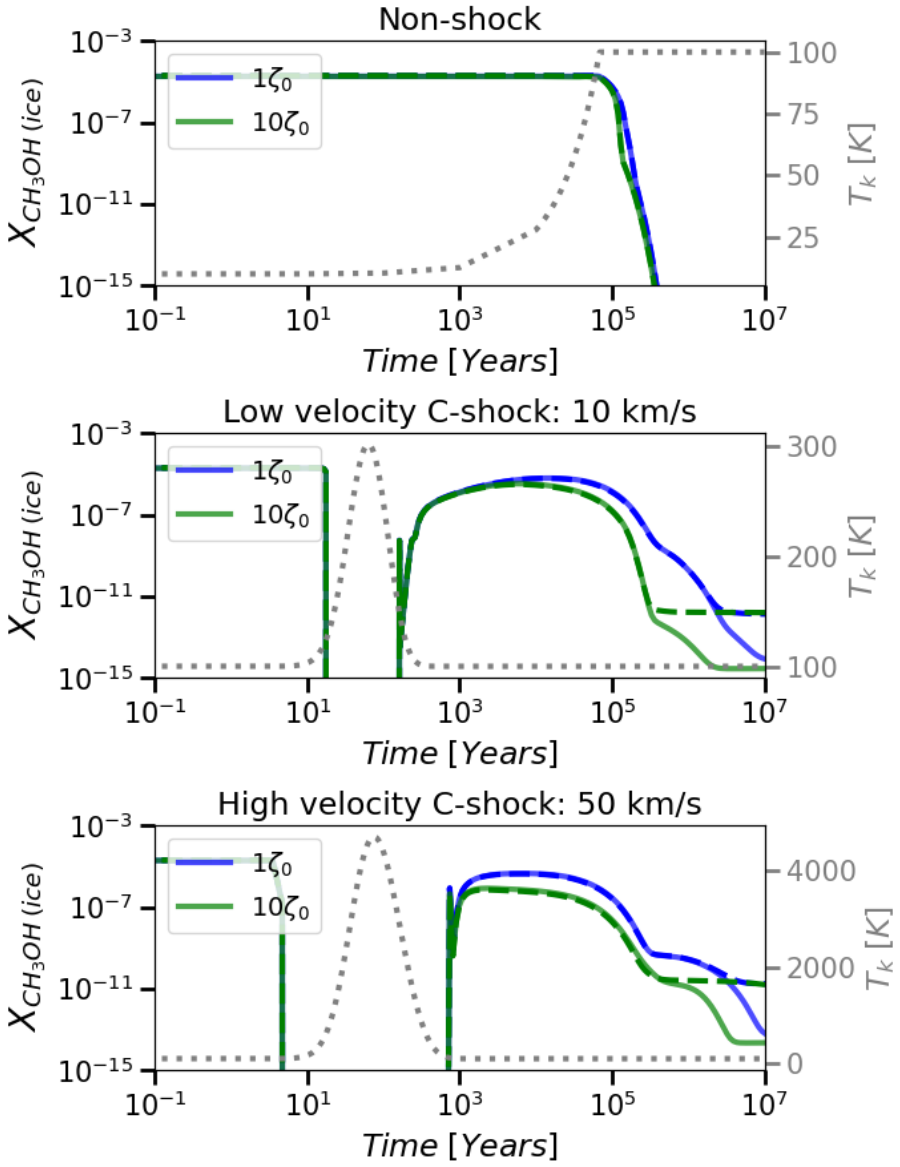

Figure 3-22.: Chemical abundances of ice-phase methanol as a function of time for Hot Core (top panel), slow C-shock (middle panel) and high C-shock (bottom panel) models with a pre-shocked gas density volume of $n_{H_2\,(init)} = 10^5\ cm^{-3}$ and $T_{k,init}$ (or T_{HC})=100 K. The dashed and solid lines correspond to the default and current schemes, respectively. The evolution of gas temperature, $T_k\ (t)$, is depicted by the gray dotted line.

$$CH_3O_{(surf)} + H_{(surf)} \longrightarrow CH_3OH_{(surf)}, \tag{3-15}$$

$$CH_2OH_{(surf)} + H_{(surf)} \longrightarrow CH_3OH_{(surf)}, \tag{3-16}$$

$$H_{(surf)} + H_2CO_{(surf)} \longrightarrow CH_2OH_{(surf)}, \tag{3-17}$$

$$H_{(surf)} + H_2CO_{(surf)} \longrightarrow CH_3O_{(surf)}, \tag{3-18}$$
$$CH_3OH_2{}^+{}_{(g)} \longrightarrow CH_3OH_{(surf)} + H_{(g)}. \tag{3-19}$$

Both schemes, current and default, exhibit nearly identical reactions in each time step, with a few exceptions. For instance, the current scheme suggests that CH_2OH hydrogenation occurs more frequently due to the change in branching ratios.

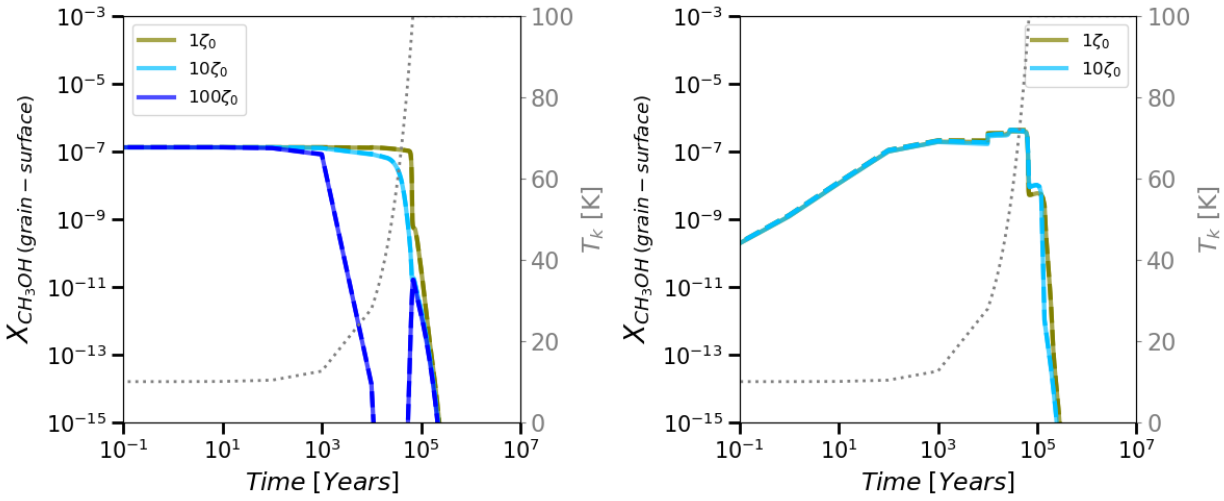

Figure 3-23.: Comparison of surface methanol abundance over time as a function of CRIR at $\zeta = 1\zeta_0$ (dark green) and $\zeta = 10\zeta_0$ (light blue) in non-shock models with T_{HC}=100 K. The panel on the left corresponds to the $n_{H_2\,(init)} = 10^3\ cm^{-3}$ model, while the panel on the right corresponds to the $n_{H_2\,(init)} = 10^6\ cm^{-3}$ model. The dashed and solid lines correspond to the default and current schemes, respectively. The evolution of gas temperature, $T_k\ (t)$, is depicted by the gray dotted line.

In C-shock Models Figures 3-24 and 3-25 shown a contrast of surface methanol abundance evolution as a function of CRIR in low and high-velocy C-shock models, respectively. The methanol abundance on the surface in both C-shock models evolves depending on $n_{H_2\,(init)}$, as demonstrated in Figs. 3-24 and 3-25. For the surface phase, there are no significant differences in the most important reactions between the low- and high-velocity C-shocks at each time step. Therefore, this analysis applies to both C-shock models.

During the pre-shock epoch, surface methanol is primarily formed through the hydrogenation of CH_3O. In certain instances, CH_3OH condensation, CH_2OH hydrogenation, and the radical-molecule H-atom abstraction route (Rxn.(3-20)[78]) also aided the formation process. CH_3OH condensation and CH_2OH hydrogenation primarily occur at $n_{H_2\,(init)} = 10^3\ cm^{-3}$, with the former dominating at $T_{k,init}$=10 K and the latter at $T_{k,init}$=50 and 100 K. The radical-molecule route takes place at high $T_k\ (t)$ in models with $n_{H_2\,(init)} \geq 10^4\ cm^{-3}$.

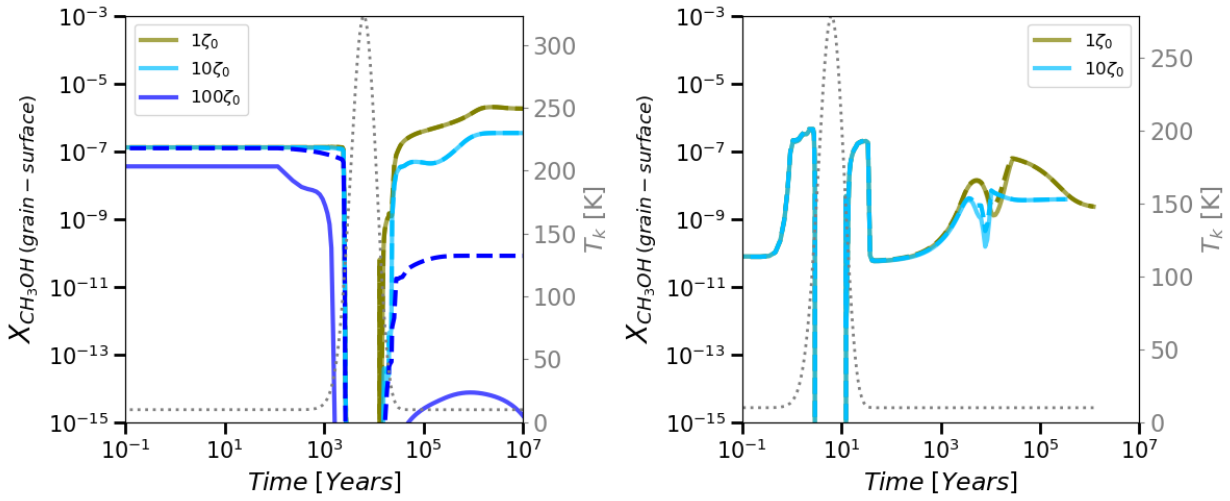

Figure 3-24.: Comparison of surface methanol abundance over time as a function of CRIR at $\zeta = 1\zeta_0$ (dark green) and $\zeta = 10\zeta_0$ (light blue) in low-velocity C-shock models (v_{shock} =10 km/s) with $T_{k,init}$=10K. The panel on the left corresponds to the $n_{H_2\,(init)} = 10^3\,cm^{-3}$ model, while the panel on the right corresponds to the $n_{H_2\,(init)} = 10^6\,cm^{-3}$ model. The dashed and solid lines correspond to the default and current schemes, respectively. The evolution of gas temperature, $T_k\,(t)$, is depicted by the gray dotted line.

$$CH_3O_{(surf)} + H_2CO_{(surf)} \longrightarrow CH_3OH_{(surf)} + H_{(surf)}. \tag{3-20}$$

As the shock wave propagates, there is a significant abundance rise of surface methanol under CND conditions ($n_{H_2\,(init)} = 10^5 - 10^6\,cm^{-3}$ and $\zeta = 1 - 10\zeta_0$), which is not present in the other models. However, the surface methanol abundance decreases drastically below 10^{-15} at the maximum $T_k\,(t)$, regardless of the model settings. The formation of surface methanol during the shock involves a series of reactions. The H-atom addition reactions (Rxns. 3-15 and 3-16) are replaced by the H-abstraction route as $T_k\,(t)$ rises, while bulk-to-surface transfer occurs at the maximum $T_k\,(t)$.

As the shock wave dissipates, the surface methanol abundance increases depending on gas conditions and CRIR. At low gas volume densities ($n_{H_2\,(init)} = 10^3 - 10^4\,cm^{-3}$), $T_{k,init}$ and CRIR exert a more pronounced influence, leading to a decrease in post-shock abundance. At high gas volume densities ($n_{H_2\,(init)} = 10^5 - 10^6\,cm^{-3}$), the post-shock surface methanol abundance remains at the same magnitude as the pre-shocked methanol abundance, regardless of both parameters. In the post-shock epoch, the formation pathways are similar to those in the pre-shock epoch. However, at $n_{H_2\,(init)} = 10^3\,cm^{-3}$, $\zeta = 1 - 10\zeta_0$, and $T_{k,init}$=100 K, the abstraction route also occurs during the post-shock epoch.

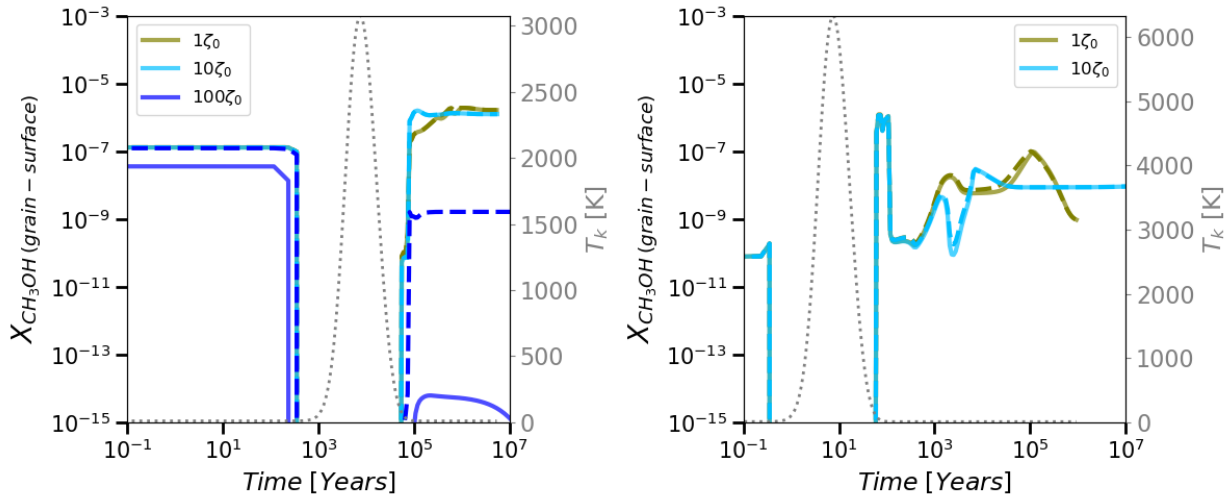

Figure 3-25.: Comparison of surface methanol abundance over time as a function of CRIR at $\zeta = 1\zeta_0$ (dark green) and $\zeta = 10\zeta_0$ (light blue) in high-velocity C-shock models (v_{shock} =50 km/s) with $T_{k,init}$=10K. The panel on the left corresponds to the $n_{H_2\,(init)} = 10^3\,cm^{-3}$ model, while the panel on the right corresponds to the $n_{H_2\,(init)} = 10^6\,cm^{-3}$ model. The dashed and solid lines correspond to the default and current schemes, respectively. The evolution of gas temperature, $T_k\,(t)$, is depicted by the gray dotted line.

The destruction of the surface methanol in both pre- and post-shock epochs is due to the surface-to-bulk transfer, UV desorption, and CH_3OH_{surf} sublimation. On the other hand, the destruction of surface methanol during the shock also involves a series of reactions, such as UV desorption, CH_3OH_{surf} sublimation, and Rxn.(3-21)[26, 58]. This last reaction dominates at the gas kinetic temperature peak.

$$CH_3OH_{(surf)} + CRP \longrightarrow CH_{3(g)} + OH_{(g)}. \tag{3-21}$$

The main difference between the default and current schemes is the prevalence of the radical-molecule H-atom abstraction route as $T_k(t)$ increases. In the current scheme, methoxy radical hydrogenation dominates as the final step in the overall CO hydrogenation mechanism on the grain surface. However, as the temperature rises due to shock heating, the abstraction route replaces radical CH_3O hydrogenation as the final step in CH_3OH formation.

As observed, the methanol yield from both schemes is dependent on the surface temperature, if we assume $T_{surf} = T_k\,(t)$. Santos *et al.* (2022) [75] and Simons *et al.* (2020) [78] have explained that there is a competition between the increase in the diffusion of H atoms and the decrease in their residence time on the ice as a function of temperature. At low temperatures, CH_3O surface radicals undergo hydrogenation. However, as the temperature

increases to above 20-30 K [78], the residence time of H atoms on the surface decreases substantially. At the same time, radicals become mobile, allowing the abstraction reaction to become competitive with CH_3O radical hydrogenation.

In the meantime, the grain surface serves as a boundary between the bulk and the gas-phase. It is the primary site for chemical and thermal adsorption and desorption, and is directly impacted by ultraviolet (UV) radiation and high-energy particles, such as cosmic rays. Additionally, it is the layer where interactions between interstellar grains, such as collisions and agglomeration, occur most frequently. The behavior of grain-surface methanol is much more sensitive than that of ice as a whole. This is demonstrated by comparing Figures **3-23** to **3-25** and Figure **3-22**.

The difference in surface methanol abundance between schemes is presented in Figures **3-23**, **3-24**, and **3-25**. Similar to the gas and ice-phases, the default scheme yields more surface methanol than the current scheme. Additional details on this subject will be discussed in the following subsection, as the bulk is the primary component of the ice-dust grain.

Grain-bulk phase

The bulk corresponds to the inner layers of the grain, everything beneath the surface. Species from the bulk can diffuse onto the surface, but they can also be released into the gas phase or destroyed. The majority of the dust grain is located below the surface.

In Hot Core Models Figure **3-26** illustrates the evolution of bulk methanol abundance in non-shock scenarios. The initial bulk methanol abundance increases as $n_{H_2\,(init)}$ increases. However, there is no significant change observed with increasing T_k (t). This is expected because methanol is dependent on both H_2CO and CH_3O, whose formation also increases with the presence of hydrogen. As T_k (t) in the core increases, methanol is primarily formed through the hydrogenation of CH_3O (Rxn.(3-22)[78]), the radical-molecule route (Rxn.(3-23)[78]), and surface-to-inner layer transfer. The hydrogenation of CH_3O dominates until T_k $(t)\sim$ 60 K at $n_{H_2\,(init)} = 10^3\ cm^{-3}$, after which the abstraction route takes over. At $n_{H_2\,(init)} \geq 10^4 cm^{-3}$, the primary methanol formation routes are the abstraction reaction and surface-to-inner layer transfer. Bulk methanol is destroyed through CH_3OH_{bulk} sublimation, bulk-to-surface transfer, and individual swaps from the inner-grain layers.

$$CH_3O_{(\text{bulk})} + H_{(\text{bulk})} \longrightarrow CH_3OH_{(\text{bulk})}, \tag{3-22}$$

$$CH_3O_{(\text{bulk})} + H_2CO_{(\text{bulk})} \longrightarrow CH_3OH_{(\text{bulk})} + HCO_{(\text{bulk})}. \tag{3-23}$$

The radical-molecule H-atom abstraction route dominates the formation of methanol in the

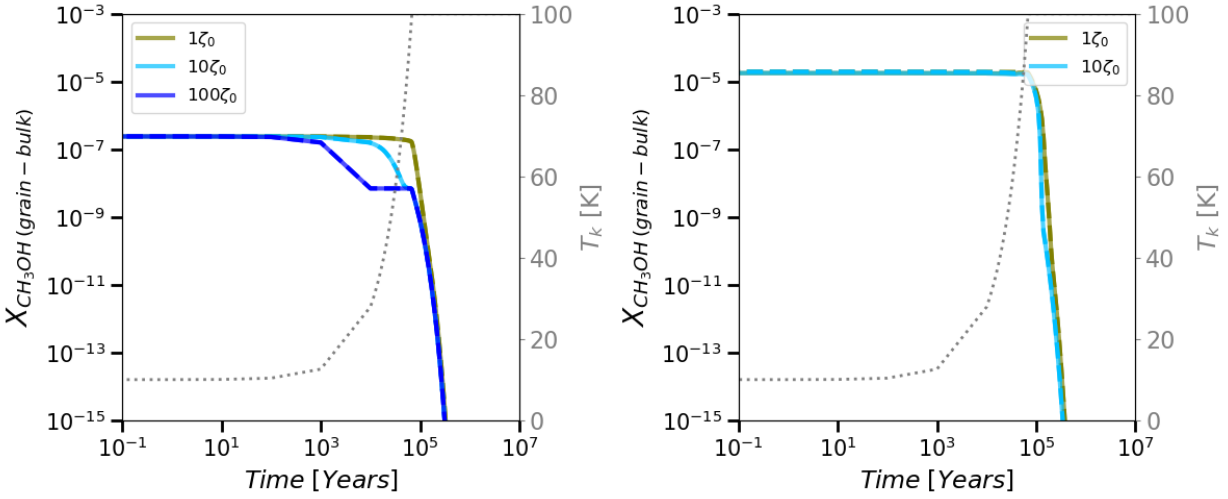

Figure 3-26.: Comparison of bulk methanol abundance over time as a function of CRIR at $\zeta = 1\zeta_0$ (dark green) and $\zeta = 10\zeta_0$ (light blue) in non-shock models with T_{HC}=100K. The panel on the left corresponds to the $n_{H_{2\,(init)}} = 10^3\ cm^{-3}$ model, while the panel on the right corresponds to the $n_{H_{2\,(init)}} = 10^6\ cm^{-3}$ model. The dashed and solid lines correspond to the default and current schemes, respectively. The evolution of gas temperature, $T_k\ (t)$, is depicted by the gray dotted line.

bulk, with $n_{H_{2\,(init)}}$ being the most influential factor. High n_{H_2} favors the formation of H_2 and OH on the grain surface (Rxns.(3-24)[9], (3-25)[78], and (3-26)[95]), which accumulates in the bulk as new surface layers form. Due to its high reactivity, the H atom reacts with CO and O to primarily form H_2O and H_2CO in the bulk grain (Rxns.(3-27)[78], (3-28)[78], and (3-29)[95]). The H atoms must diffuse in order to react with the minor ice component, CH_3O radicals. Therefore, the dominance of the radical-molecule route is likely due to the greater availability of H_2CO in the bulk, compared to H atoms, for reacting with CH_3O [75].

$$\mathrm{H_{(surf)} + H_{(surf)} \longrightarrow H_{2(surf)}}, \tag{3-24}$$

$$\mathrm{CO_{(surf)} \xrightarrow{H_{(surf)}} HCO_{(surf)} \xrightarrow{H_{(surf)}} CO_{(surf)} + H_{2(surf)}}, \tag{3-25}$$

$$\mathrm{H_{(surf)} + O_{(surf)} \longrightarrow OH_{(surf)}}. \tag{3-26}$$

$$\mathrm{CO_{(bulk)} \xrightarrow{H_{(bulk)}} HCO_{(bulk)} \xrightarrow{H_{(bulk)}} CO_{(bulk)} + H_{2(bulk)}}, \tag{3-27}$$

$$\mathrm{CO_{(bulk)} \xrightarrow{H_{(bulk)}} HCO_{(bulk)} \xrightarrow{H_{(bulk)}} H_2CO_{(bulk)}}, \tag{3-28}$$

$$\mathrm{O_{(bulk)} \xrightarrow{H_{(bulk)}} OH_{(bulk)} \xrightarrow{H_{(bulk)}} H_2O_{(bulk)}}. \tag{3-29}$$

Simons *et al.* (2020) [78] performed a series of simulated codepositions of CO+H and H_2CO+H considering different H-atom binding energies (250 K, 420 K, and 670 K). In their simulations, the authors found that the radical-molecule route was the primary pathway for methanol formation. They emphasized the dependence of CH_3OH formation on the H:CO ratio. They also pointed out that the dominance of the H-abstraction reaction was because when two H_2CO molecules were produced nearby, only one H atom was required for hydrogenation to convert CH_3O into CH_3OH and HCO. Subsequently, these species underwent rapid hydrogenation once more [78].

Contrastingly, Santos *et al.* (2022) [75] conducted experiments under ultrahigh vacuum conditions and astronomically relevant temperatures. They employed H:H_2CO (or D_2CO) flux ratios of 10:1 and 30:1. Similar to Simons *et al.* (2020) [78], Santos *et al.* (2022) [75] observed that the radical-molecule route was the predominant pathway for methanol formation in their experiments. They specifically tested a H/H_2CO(D_2CO) ratio of 30 at 10 K and concluded that the CHD_2OH/CH_3OH ratios were negligibly different, considering the detection error. Consequently, Santos *et al.* (2022) [75] suggested that a higher hydrogen flux only slightly affected the contribution of the radical-molecule H-atom abstraction route, even if a potentially higher H flux might favor the atom-addition route, and still governed the formation of CH_3OH [75].

Our results confirm the last statement for the range of $n_{H_2\,(init)} = 10^4 - 10^6 cm^{-3}$. In this range, the abstraction route dominates and produces the same methanol abundance. Therefore, the product yield is limited by the abundance of formaldehyde rather than the abundance of hydrogen atoms, which are in excess. These results also support the findings of Santos *et al.* (2022) [75], where the contribution from each route is determined by the availability of hydrogen, formaldehyde and methoxide radical in the ice. In an abstraction reaction, the probability of the two reactants coming into contact is higher compared to a barrierless hydrogenation reaction [75].

In C-shock Models Figures **3-27** and **3-28** shown a contrast of bulk methanol abundance evolution as a function of CRIR in low and high-velocy C-shock models, respectively. During the pre-shock epoch, bulk methanol formation is primarily dependent on $n_{H_2\,(init)}$, similar to the Hot Core model. At a initial gas volume density of $n_{H_2\,(init)} = 10^3\ cm^{-3}$, CH_3OH_{bulk} is due to the surface-to-bulk transfer, CH_3O hydrogenation, and individual swap from the surface. At a initial gas volume density of $n_{H_2\,(init)} = 10^4\ cm^{-3}$, the formation is a result of the radical-molecule route, mostly observed at $T_{k,init} \geq$50 K, and the transfer of surface layers inwards. At higher hydrogen abundances related to higher initial gas volume densities ($n_{H_2\,(init)} = 10^5 - 10^6\ cm^{-3}$), bulk methanol formation is exclusively due to the abstraction reaction. Methanol destruction at this epoch is caused by CH_3OH_{bulk} sublimation and the transfer of layers to the surface.

In the bulk phase, the radical-molecule route dominates from $T_k\ (t) \geq 10$ K under the CND conditions. At the low temperatures typical of molecular clouds, chemical reactions are

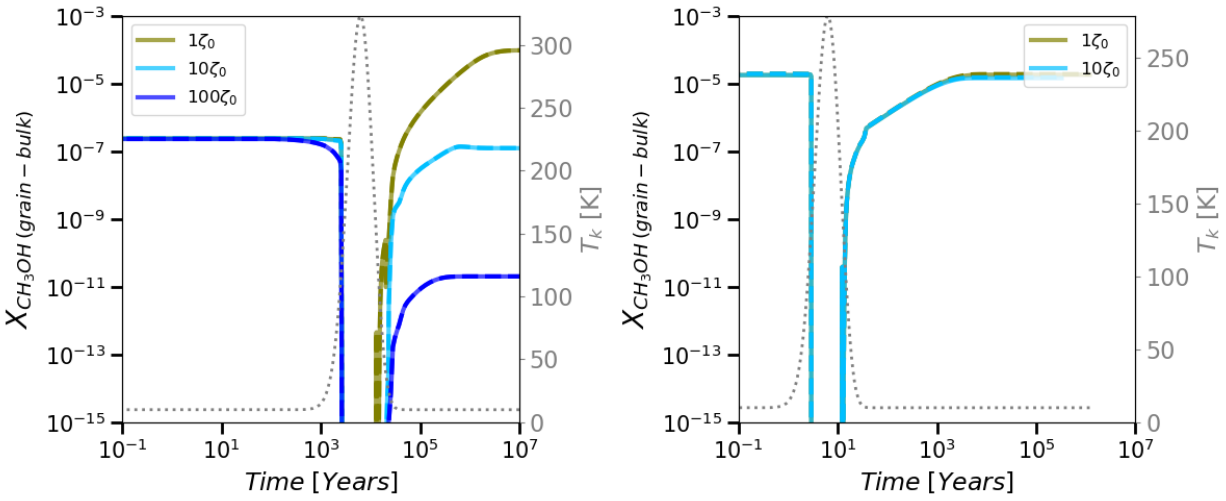

Figure 3-27.: Comparison of bulk methanol abundance over time as a function of CRIR at $\zeta = 1\zeta_0$ (dark green) and $\zeta = 10\zeta_0$ (light blue) in low-velocity C-shock models (v_{shock}=10 km/s) with $T_{k,init}$=10 K. The panel on the left corresponds to the $n_{H_2\,(init)} = 10^3\ cm^{-3}$ model, while the panel on the right corresponds to the $n_{H_2\,(init)} = 10^6\ cm^{-3}$ model. The dashed and solid lines correspond to the default and current schemes, respectively. The evolution of gas temperature, $T_k\,(t)$, is depicted by the gray dotted line.

activated by quantum-mechanical tunneling, making it a key process for chemical evolution [75, 34]. At temperatures as low as 10 K, if the gas and grain temperature are assumed to be equal, the reaction most likely proceeds through quantum-tunneling [75], as the activation barrier for the radical-molecule route is approximately $\Delta E = 2670$K [2]. In our results, hydrogen abstraction from an aldehyde group seems faster than hydrogen addition to the methoxide carbon atom in these low temperatures.

All models exhibit a drop in abundance below 10^{-15} when the temperature increases due to shock heating. The propagation of both C-shock waves leads to the occurrence of the abstraction reaction and CH_3O and CH_2OH hydrogenations (Rxn.(3-30)[78]) near the maximum $T_k\,(t)$. However, $CH_3OH_{(bulk)}$ formation takes place at the peak of the shock due to surface-to-bulk transfer, while $CH_3OH_{(bulk)}$ destruction occurs due to the pre-shocked epoch reactions mentioned earlier.

$$CH_2OH_{(bulk)} + H_{(bulk)} \longrightarrow CH_3OH_{(bulk)}. \tag{3-30}$$

Santos *et al.* (2022) [75] reports that the abstraction route accounts for approximately 80 % of the contributions in the 10-16 K interval, which is consistent with the findings of Simons *et al.* (2020) [75]. In both studies, CH_3OH formation is independent of temperature in the

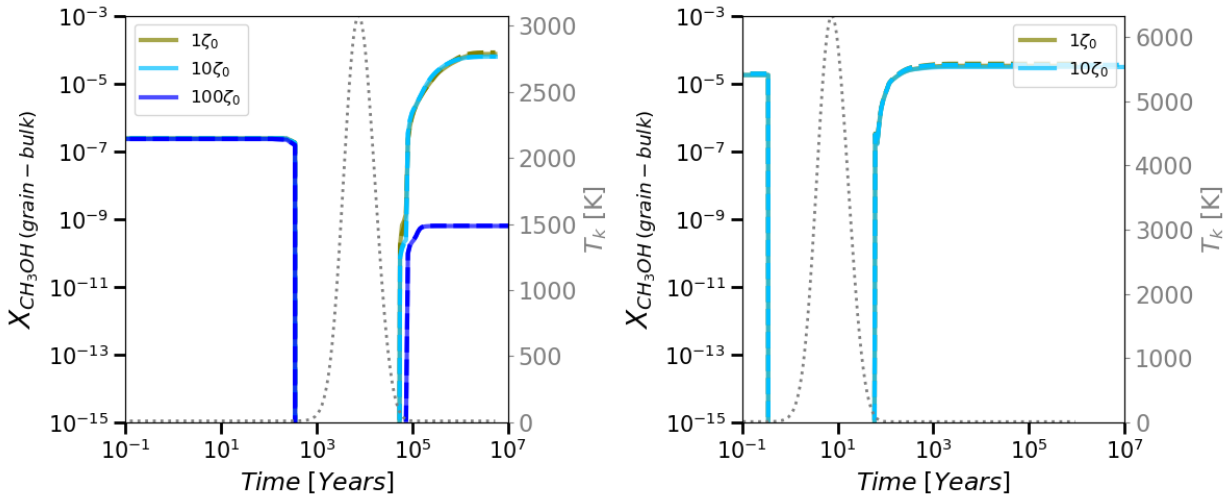

Figure 3-28.: Comparison of bulk methanol abundance over time as a function of CRIR at $\zeta = 1\zeta_0$ (dark green) and $\zeta = 10\zeta_0$ (light blue) in high-velocity C-shock models (v_{shock}=50 km/s) with $T_{k,init}$=10 K. The panel on the left corresponds to the $n_{H_2\,(init)} = 10^3\,cm^{-3}$ model, while the panel on the right corresponds to the $n_{H_2\,(init)} = 10^6\,cm^{-3}$ model. The dashed and solid lines correspond to the default and current schemes, respectively. The evolution of gas temperature, $T_k\,(t)$, is depicted by the gray dotted line.

10-16 K range. However, our results indicate that the abstraction reaction is the dominant final step in the CO hydrogenation to form CH_3OH, both at low gas kinetic temperatures, such as those found in molecular clouds, and at high gas kinetic temperatures, such as those achieved by shock heating, under $n_{H_2\,(init)} = 10^5 - 10^6\,cm^{-3}$. Quantum tunneling is activated at low temperatures, but as the temperature rises, it probably becomes also thermally activated. This last scenario is most commonly observed under low $n_{H_2\,(init)}$, where elevated temperatures may promote the radical-molecule route.

Bulk methanol abundance increases again as the shock wave dissipates. The magnitude of the increase depends on $n_{H_2\,(init)}$, $T_{k,init}$, and CRIR. The effect of $T_{k,init}$ and CRIR is much more pronounced at the SB-ring conditions, where the post-shock abundance decreases dramatically at high $T_{k,init}$ and CRIR. During the post-shock epoch, the bulk methanol formation and destruction pathways are the same as in the pre-shock epoch. With the exception that the radical-molecule pathway is also highlighted at a gas volume density of $n_{H_2\,(init)} = 10^3\,cm^{-3}$.

In terms of CRIR, cosmic ray-induced photons can dissociate H_2CO and CH_3OH, producing functional group radicals such as CH_3 and CH_3O on or within the ice. Our results also suggest that high CRIR ($\zeta = 100\zeta_0$) decreases the abundance of methanol in all phases. However, these rate affects both the radical-molecule route and other possible pathways, as the X-ray field destroys all methanol precursors involved in the overall CO hydrogenation mechanism.

Figure **3-22** show that in general in both non-shock and shock models, methanol is more abundant when using the default scheme compared to the current scheme. The main difference between the two schemes is that the abstraction reaction is the most important pathway for methanol formation in the bulk, while the CH_2OH hydrogenation has become more significant due to changes in branching ratios, especially at higher T_k (t). With the current scheme, we used branching ratios from Simons *et al.* (2020) [78], which considers a more extensive network with reactions that are missing in the UMIST RATE2012 database [56]. Simons *et al.* (2020) [78] results suggest that methanol is strongly overproduced (up to 3×10^{-1}) using rates from the UMIST network, probably because the UMIST network uses a lower effective rate instead of the full hydrogenation or abstraction network [78]. Therefore, it is expected that using the branching ratios proposed by Simons *et al.* (2020) [78], a network based on quantum chemical calculations combined with a microscopic kinetic Monte Carlo simulation, will yield a lower but proper amount of methanol. It should be noted that the predicted difference in bulk methanol abundance between schemes for our case is minimal ($\sim 1 \times 10^{-5}$) because our network does not include other reactions (i.e., HCO + HCO reactions [78]) that could also alter the molecular composition of the grain mantle. Therefore, we encourage the extension of the chemical reaction network for the sake of completeness in future works.

3.2.2. Radical-molecule H-atom abstraction: Impact on precursors in solid state

The addition of the new route in the chemical network has a significant impact on the immediate methanol precursors, CH_3O and H_2CO, as well as the byproduct HCO, particularly in the ice phase. Therefore, we will discuss their shock behavior and how the radical-molecule route affects their overall chemical pathway over time.

In Figures **3-29** to **3-31** we present the chemical abundances of formyl radical (HCO), formaldehyde (H_2CO) and methoxyl radical (CH_3O) as a function of time for non-shock and shock models with an initial gas density of $n_{H_2\,(init)} = 10^5\ cm^{-3}$ and $T_{k,init}$ (or T_{HC}=100K). Ice HCO, H_2CO and CH_3O, like methanol, increases in abundance in non-shock models with increasing $n_{H_2\,(init)}$. However, it remain constant as T_k (t) rises due to core heating. The destruction of each molecule is observed with high CRIR or when T_{HC} is reached.

HCO, H_2CO and CH_3O abundance decreases significantly (below 10^{-15}) as the shock wave propagates. Similar to methanol, their solid abudances increases again once the shock wave dissipates. It is important to note that the scheme used can drastically influence the abundance of the precursors and byproduct obtained. Therefore, we will analyze each of them separately.

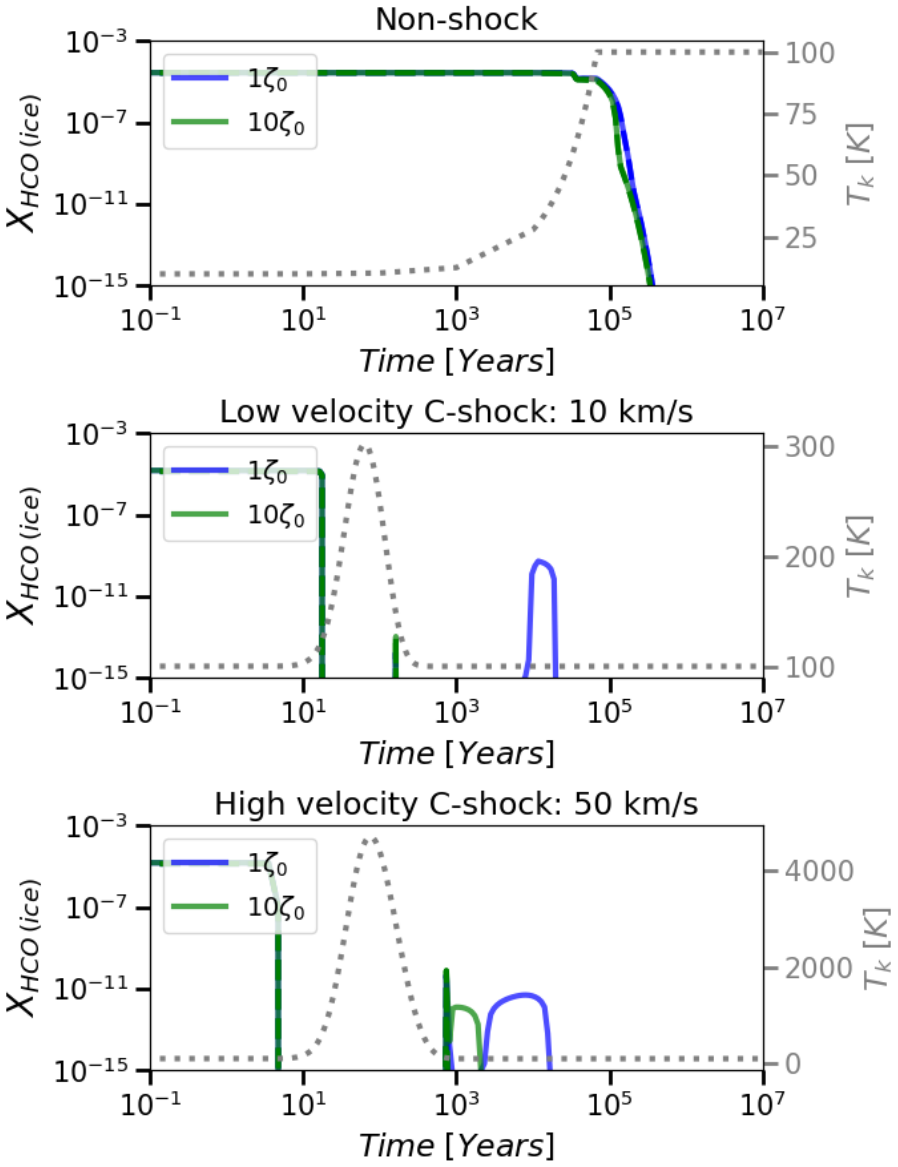

Figure 3-29.: Chemical abundances of ice-phase formyl radical as a function of time for Hot Core (top panel), slow C-shock (middle panel) and high C-shock (bottom panel) models with a pre-shocked gas density of $n_{H_{2\,(init)}} = 10^5\ cm^{-3}$ and $T_{k,init}$ (or T_{HC})=100 K. The dashed and solid lines correspond to the default and current schemes, respectively. The evolution of gas temperature, $T_k\,(t)$, is depicted by the gray dotted line.

Formyl radical (HCO)

In non-shock scenarios, grain-surface HCO formation occurs sporadically via the radical-molecule pathway as $T_k\,(t)$ rises due to core heating in models from an initial gas volume

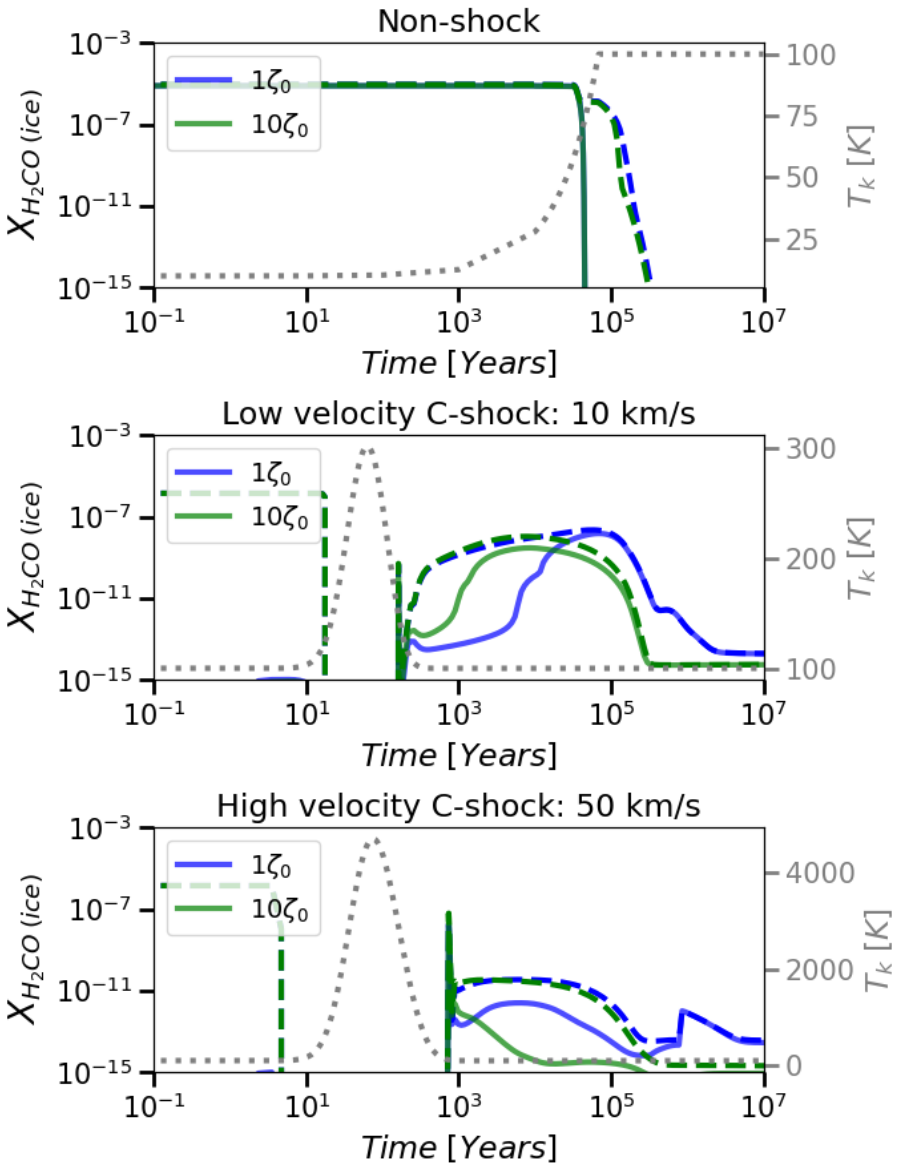

Figure 3-30.: Chemical abundances of ice-phase formaldehyde as a function of time for Hot Core (top panel), slow C-shock (middle panel) and high C-shock (bottom panel) models with a pre-shocked gas density of $n_{H_{2\,(init)}} = 10^5\ cm^{-3}$. The dashed and solid lines correspond to the default and current schemes, respectively. The evolution of gas temperature, $T_k\ (t)$, is depicted by the gray dotted line.

density of $n_{H_{2\,(init)}} = 10^4\ cm^{-3}$ onwards. In shock scenarios, HCO_{surf} formation is strongly influenced by the abstraction reaction. As $T_{k,init}$ increases, its occurrence is much more pronounced in the pre- and post-shock epochs. The main difference from the default scheme is that the radical-molecule pathway is completely replaced by Rxn.(3-31)[18].

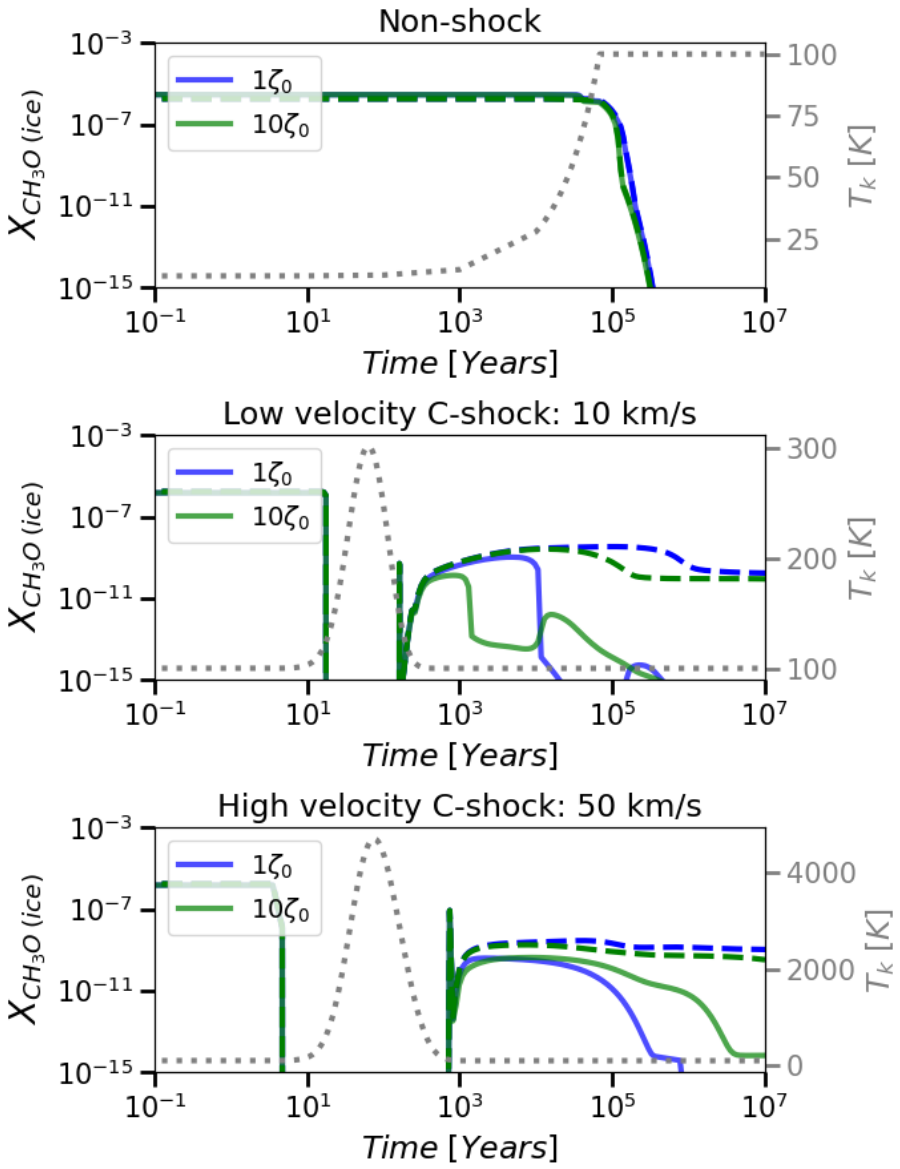

Figure 3-31.: Chemical abundances of ice-phase methoxyl radical as a function of time for Hot Core (top panel), slow C-shock (middle panel) and high C-shock (bottom panel) models with a pre-shocked gas density of $n_{H_2\,(init)} = 10^5 cm^{-3}$ and $T_{k,init}$ (or T_{HC})=100 K. The dashed and solid lines correspond to the default and current schemes, respectively. The evolution of gas temperature, T_k (t), is depicted by the gray dotted line.

$$NH_{2(surf)} + H_2CO_{(surf)} \longrightarrow NH_{3(surf)} + HCO_{(surf)}. \tag{3-31}$$

On the other hand, the formation of HCO in the bulk is also influenced by the insertion of the

H-abstraction route into the chemical network. In scenarios with or without shock, HCO_{bulk} formation is attributed to reactions (3-32)[78] and (3-33)[18], as well as the abstraction reaction. The latter is the preferential reaction at $n_{H_2\,(init)} = 10^4\,cm^{-3}$, while in other models, especially at high n_{H_2}, its importance increases as $T_k\,(t)$ increases. The main distinction from the default scheme is that Rxns.(3-32), (3-33), and (3-34)[78] substitute the radical-molecule route, particularly Rxns.(3-33) and (3-32).

$$H_{(bulk)} + CO_{(bulk)} \longrightarrow HCO_{(bulk)}, \tag{3-32}$$
$$NH_{2(bulk)} + H_2CO_{(bulk)} \longrightarrow NH_{3(bulk)} + HCO_{(bulk)}, \tag{3-33}$$
$$H_{(bulk)} + H_2CO_{(bulk)} \longrightarrow H_{2(bulk)} + HCO_{(bulk)}. \tag{3-34}$$

When comparing the abundance of ice formyl radicals between schemes (see Fig. **3-29**), it is generally observed that the current scheme predicts more HCO abundance. This is because HCO is a byproduct in the radical-molecule route. The HCO radical is an important astrochemical building block due to its ability to synthesize biorelevant complex organic molecules (COMs), such as glycoaldehyde, ethylene glycol, and methyl formate [103, 78, 49, 75]. Therefore, this new reaction must be considered in the overall ice-grain chemical network as it influences the abundance of formyl radical and, hence, the distribution of COMs in the interstellar medium.

Formaldehyde (H_2CO)

In non-shock and shock scenarios, the abstraction reaction dominates in the grain surface and bulk from $n_{H_2\,(init)} = 10^4\,cm^{-3}$ onwards, becoming more prevalent as $T_k\,(t)$ increases.

The main difference with the default scheme is that the abstraction route in the bulk phase is replaced by the displace of bulk particles, Rxn. (3-35)[18] and formaldehyde sublimation. Although at v_{shock}=50 km/s, the dominance of H_2CO hydrogenations (Rxns.(3-36)-(3-38)[78]) is emerging. It is generally shown that as $T_{k,init}$ and $n_{H_2\,(init)}$ increase in the default scheme, there is more formaldehyde in the solid state compare to the current scheme (see Fig. **3-30**). This difference is due to the faster radical-molecule rate, which results in more formaldehyde being used to produce ice methanol and hence providing a lower H_2CO abundance in the current scheme.

$$NH_{2(bulk)} + H_2CO_{(bulk)} \longrightarrow NH_2CHO_{(bulk)} + H_{(bulk)}, \tag{3-35}$$
$$H_2CO_{(bulk)} + H_{(bulk)} \longrightarrow CH_3O_{(bulk)}, \tag{3-36}$$
$$H_2CO_{(bulk)} + H_{(bulk)} \longrightarrow H_{2(bulk)} + HCO_{(bulk)}, \tag{3-37}$$
$$H_2CO_{(bulk)} + H_{(bulk)} \longrightarrow CH_2OH_{(bulk)}. \tag{3-38}$$

Methoxyl radical (CH_3O)

Methoxyl radical destruction in the grain surface through the abstraction route is not seen in Hot Core scenarios but in both low and-high velocity C-shocks. During both the pre-and post-shock epochs, CH_3O_{surf} destruction occurs through the radical methoxyl hydrogenation (Rxn.(3-15)) in $T_{k,init} = 10$ and 50 K models, and through the abstraction route (Rxn.(3-20)) in $T_{k,init} = 100$ K models. As $T_k\ (t)$ increases due to shock heating, the abstraction reaction occurs near the maximum $T_k\ (t)$, but it is not observable at $n_{H_2\,(init)} = 10^6\ cm^{-3}$ in high-velocity shocks. The default model differs from the current in that sublimation or hydrogenation of $CH_3O_{(surf)}$ replaces the hydrogen abstraction reaction near the maximum $T_k\ (t)$.

On the other hand, from $n_{H_2\,(init)} = 10^4 cm^{-3}$ onwards, the radical-molecule route (Rxn.(3-23)) and layer transfer are the primary destruction reactions for CH_3O_{bulk}.

The current scheme produces in general more methoxyl radical in non-shock and shock scenarios, due to the change in branching ratios. However, there are certain time steps (post-shocked epoch at $n_{H_2\,(init)} = 10^{4-6}\ cm^{-3}$, $T_{k,init} = 100$ K and $\zeta = 1 - 100\zeta_0$) where the difference in abundance between the schemes does not follow the expected pattern, i.e. the current scheme predicts higher abundances of methanol and formaldehyde, and lower abundances of HCO and CH_3O radicals. The reason for this is unclear and we leave it open for future research.

4. Conclusions, Recommendations & Contributions

4.1. Conclusions

In summary, this work presents physical models for hot cores and parameterized C-shocks to constrain the behavior of methanol abundance and its formation pathways as a function of shock velocity and gas conditions in the ISM. For this purpose, we implemented the radical molecule H-atom abstraction reaction as the final step in the overall CO hydrogenation mechanism in the UCLCHEM chemical network. We then compared its abundance behavior in gas and solid states in plausible shocked regions, such as the Circumnuclear Disk (CND) near the Active Galactic Nuclei (AGN) and the Starburst Ring (SB) of NGC 1068. Our analysis led us to the following conclusions:

1. Gas-phase methanol can trace C-type shocks, regardless of their velocity, because its abundance increases significantly due to grain sputtering or sublimation as the shock wave propagates. This behaviour is independent of the scheme employed [refer to Section 3.1.1].

2. Formaldehyde as a potential shock tracer may facilitate precise measurements of gas density and temperature and distinguish between shock waves and methanol formation pathways [refer to Section 3.1.2].

3. After comparing our models with the multi-linear molecular study conducted by Huang *et al.* (submitted) [37], we concluded that the observed CH_3OH abundance could arise from C-shock scenarios or through the thermal sublimation of ices caused by events such as star formation processes, as both models surpassed the observed CH_3OH minimum limit. Therefore, it will be critical to use more observations as constraint in drawing conclusions about the origin of CH_3OH abundance [refer to Section 3.1.3].

4. For the first time, we investigate the impact of the radical-molecule H-atom abstraction route in methanol formation under shock-influenced environments, such as NGC 1068. The radical-molecule pathway is the most favored reaction for the final step in the overall CO hydrogenation mechanism leading to CH_3OH formation in the bulk of

interstellar ice-dust grains. This finding is in consistent with Simons *et al.* (2020) [78] and Santos *et al.* (2022)[75]. However, its dominance of dependent on the gas kinetic temperature T_k, gas volume density n_{H_2}, velocity of the C-shock wave v_{shock}, and cosmic ray ionisation rate ζ [refer to Section 3.2.1].

5. The influence of C-shocks in the preference methanol formation pathway is intriguing. Gaseous and grain-surface methanol formation is generally due to the hydrogenation of CH_3O in both non-shock and shock scenarios. However, C-shock waves trigger the abstraction route in both gas and surface phases as $T_k\,(t)$ rises due to shock heating. The abstraction route is the predominant last step to form methanol in the inner layers of the ice grain, regardless of the model scenario [refer to Sections 3.1.1 and 3.2.1].

6. The incorporation of the radical-molecule H-atom abstraction route into the chemical network of UCLCHEM has a substantial impact on the abundance of immediate methanol precursors, CH_3O and H_2CO, as well as the abundance of the byproduct HCO. This influence is particularly pronounced in the abundance of these chemical species compared to the abundance of CH_3OH, especially in the ice phase [refer to Section 3.2.2].

4.2. Recommendations

For those who wish to use this work as a foundation for future modeling or to compare results with other gas-grain chemical codes, we recommend following these guidelines.

1. To achieve greater precision and compare with observations or experimental data, it is advisable to improve the sputtering model in UCLCHEM v.3.1 and use the expanded chemical network employed in this study. We also recommend to incorporated several radical-radical reactions that are beyond the scope of our research.

2. To determine the contribution of the radical-molecule pathway in the final stage of the CO hydrogenation mechanism, it is recommended to compare the results of Simons *et al.* (2020) [78], Santos *et al.* (2022)[75], and the current study with forthcoming observations from NASA's James Webb Space Telescope (JWST) in the infrared, as well as observations in the sub-millimeter and millimeter wavelengths with ALMA, in both molecular clouds and shocked regions.

3. Further observations of the sub-millimeter and millimeter rotational transitions of methanol are necessary to accurately determine the physical conditions of the environment in the CND and SB-ring of NGC 1068 and investigate the origin of the observed abundance. As previously mentioned, for its great potential in probing gas temperature and density, formaldehyde can also work as a shock tracer along with CH_3OH, HNCO,

and SiO base on existing models and observations. This altogether will be critical in further confirming the presence of shocks, their velocity levels, and duration following the most recent shock episode using each shock tracer.

4.3. Contributions

This project is a continuation of the Leiden/ESA Astrophysics Program for Summer Students (LEAPS) 2022 project: "The 'alcoholic' side of extragalactic shocks - chemical modeling of methanol", which was carried out with an Erasmus+ ICM grant of €4050. Additionally, we made a poster contribution at XVII Latin American Regional IAU Meeting (LARIM) and submitted it to the XVII LARIM conference proceedings in the Revista Mexicana de Astronomía y Astrofísica (RevMexAA) Conference Series edition. We have been accepted for a poster contribution at IAU General Assembly 2024. We have submitted for contribution at IV Simposio Bogotano de Ciencias Moleculares Computacioneales (SBCM), and finally, we have two articles in preparation for the Astronomy & Astrophysics (A&A) journal and the Revista eSPECTRA.

Annex A. Models in UCLCHEM for CND & SB ring in NGC 1068

Table A-1.: Models for CND regions in NGC 1068

Model	Physical scenario	Second stage physical conditions			
		v_{shock} $[km/s]$	n_{H_2} $[cm^{-3}]$	T_k $[K]$	ζ_0 $[s^{-1}]$
1	Hot Core	-	10^5	50	1
2	Hot Core	-	10^5	50	10
3	Hot Core	-	10^5	100	1
4	Hot Core	-	10^5	100	10
5	Hot Core	-	10^6	50	1
6	Hot Core	-	10^6	50	10
7	Hot Core	-	10^6	100	1
8	Hot Core	-	10^6	100	10
9	Low-velocity C-shock	10	10^5	10	1
10	Low-velocity C-shock	10	10^5	10	10
11	Low-velocity C-shock	10	10^5	50	1
12	Low-velocity C-shock	10	10^5	50	10
13	Low-velocity C-shock	10	10^5	100	1
14	Low-velocity C-shock	10	10^5	100	10
15	Low-velocity C-shock	10	10^6	10	1
16	Low-velocity C-shock	10	10^6	10	10
17	Low-velocity C-shock	10	10^6	50	1
18	Low-velocity C-shock	10	10^6	50	10
19	Low-velocity C-shock	10	10^6	100	1
20	Low-velocity C-shock	10	10^6	100	10
21	High-velocity C-shock	50	10^5	10	1
22	High-velocity C-shock	50	10^5	10	10
23	High-velocity C-shock	50	10^5	50	1
24	High-velocity C-shock	50	10^5	50	10
25	High-velocity C-shock	50	10^5	100	1
26	High-velocity C-shock	50	10^5	100	10
27	High-velocity C-shock	50	10^6	10	1
28	High-velocity C-shock	50	10^6	10	10

Table A-1 continued from previous page

Model	Physical scenario	Second stage physical conditions			
		v_{shock} $[km/s]$	n_{H_2} $[cm^{-3}]$	T_k $[K]$	ζ_0 $[s^{-1}]$
29	High-velocity C-shock	50	10^6	50	1
30	High-velocity C-shock	50	10^6	50	10
31	High-velocity C-shock	50	10^6	100	1
32	High-velocity C-shock	50	10^6	100	10

Table A-2.: Models for SB-Ring regions in NGC 1068

Model	Physical scenario	Second stage physical conditions			
		v_{shock} $[km/s]$	n_{H_2} $[cm^{-3}]$	T_k $[K]$	ζ_0 $[s^{-1}]$
33	Hot Core	-	10^3	50	1
34	Hot Core	-	10^3	50	10
35	Hot Core	-	10^3	50	100
36	Hot Core	-	10^3	100	1
37	Hot Core	-	10^3	100	10
38	Hot Core	-	10^3	100	100
39	Hot Core	-	10^4	50	1
40	Hot Core	-	10^4	50	10
41	Hot Core	-	10^4	50	100
42	Hot Core	-	10^4	100	1
43	Hot Core	-	10^4	100	10
44	Hot Core	-	10^4	100	100
45	Low-velocity C-shock	10	10^3	10	1
46	Low-velocity C-shock	10	10^3	10	10
47	Low-velocity C-shock	10	10^3	10	100
48	Low-velocity C-shock	10	10^3	50	1
49	Low-velocity C-shock	10	10^3	50	10
50	Low-velocity C-shock	10	10^3	50	100
51	Low-velocity C-shock	10	10^3	100	1
52	Low-velocity C-shock	10	10^3	100	10
53	Low-velocity C-shock	10	10^3	100	100
54	Low-velocity C-shock	10	10^4	10	1
55	Low-velocity C-shock	10	10^4	10	10
56	Low-velocity C-shock	10	10^4	10	100
57	Low-velocity C-shock	10	10^4	50	1
58	Low-velocity C-shock	10	10^4	50	10
59	Low-velocity C-shock	10	10^4	50	100
60	Low-velocity C-shock	10	10^4	100	1
61	Low-velocity C-shock	10	10^4	100	10

Table A-2 continued from previous page

Model	Physical scenario	Second stage physical conditions			
		v_{shock} $[km/s]$	n_{H_2} $[cm^{-3}]$	T_k $[K]$	ζ_0 $[s^{-1}]$
62	Low-velocity C-shock	10	10^4	100	100
63	High-velocity C-shock	50	10^3	10	1
64	High-velocity C-shock	50	10^3	10	10
65	High-velocity C-shock	50	10^3	10	100
66	High-velocity C-shock	50	10^3	50	1
67	High-velocity C-shock	50	10^3	50	10
68	High-velocity C-shock	50	10^3	50	100
69	High-velocity C-shock	50	10^3	100	1
70	High-velocity C-shock	50	10^3	100	10
71	High-velocity C-shock	50	10^3	100	100
72	High-velocity C-shock	50	10^4	10	1
73	High-velocity C-shock	50	10^4	10	10
74	High-velocity C-shock	50	10^4	10	100
75	High-velocity C-shock	50	10^4	50	1
76	High-velocity C-shock	50	10^4	50	10
77	High-velocity C-shock	50	10^4	50	100
78	High-velocity C-shock	50	10^4	100	1
79	High-velocity C-shock	50	10^4	100	10
80	High-velocity C-shock	50	10^4	100	100

Bibliografía

[1] Aikawa, Yuri ; Herbst, Eric ; Roberts, Helen ; Caselli, Paola: Molecular Evolution in Collapsing Prestellar Cores. III. Contraction of a Bonnor-Ebert Sphere. En: *ApJ* 620 (2005), Februar, Nr. 1, p. 330–346

[2] Álvarez-Barcia, S. ; Russ, P. ; Kästner, J. ; Lamberts, T.: Hydrogen transfer reactions of interstellar complex organic molecules. En: *MNRAS* 479 (2018), September, Nr. 2, p. 2007–2015

[3] Anicich, Vincent G.: Evaluated Bimolecular Ion-Molecule Gas Phase Kinetics of Positive Ions for Use in Modeling Planetary Atmospheres, Cometary Comae, and Interstellar Clouds. En: *Journal of Physical and Chemical Reference Data* 22 (1993), November, Nr. 6, p. 1469–1569

[4] Asplund, Martin ; Grevesse, Nicolas ; Sauval, A. J. ; Scott, Pat: The Chemical Composition of the Sun. En: *Annual Review of Astron and Astrophys* 47 (2009), September, Nr. 1, p. 481–522

[5] Awad, Zainab ; Viti, Serena ; Collings, Mark P. ; Williams, David A.: Warm cores around regions of low-mass star formation. En: *MNRAS* 407 (2010), Oktober, Nr. 4, p. 2511–2518

[6] Baxter, R. J. ; Hu, P.: Insight into why the Langmuir-Hinshelwood mechanism is generally preferred. En: *J. Chem. Phys.* 116 (2002), März, Nr. 11, p. 4379–4381

[7] Bland-Hawthorn, J. ; Gallimore, J. F. ; Tacconi, L. J. ; Brinks, E. ; Baum, S. A. ; Antonucci, R. R. J. ; Cecil, G. N.: The Ringberg Standards for NGC 1068. En: *Ap&SS* 248 (1997), Februar, Nr. 1-2, p. 9–19

[8] Brown, Peter N. ; Byrne, George D. ; Hindmarsh, Alan C.: VODE: A Variable-Coefficient ODE Solver. En: *SIAM Journal on Scientific and Statistical Computing* 10 (1989), Nr. 5, p. 1038–1051

[9] Cazaux, S. ; Tielens, A. G. G. M.: H_2 Formation on Grain Surfaces. En: *ApJ* 604 (2004), März, Nr. 1, p. 222–237

[10] Chang, Q. ; Cuppen, H. M. ; Herbst, E.: Gas-grain chemistry in cold interstellar cloud cores with a microscopic Monte Carlo approach to surface chemistry. En: *A&A* 469 (2007), Juli, Nr. 3, p. 973–983

[11] Charnley, S. B. ; Rodgers, S. D. ; Kuan, Y. J. ; Huang, H. C.: Biomolecules in the interstellar medium and in comets. En: *Advances in Space Research* 30 (2002), Januar, Nr. 6, p. 1419–1431

[12] Charnley, S. B. ; Tielens, A. G. G. M. ; Millar, T. J.: On the Molecular Complexity of the Hot Cores in Orion A: Grain Surface Chemistry as "The Last Refuge of the Scoundrel". En: *ApJL* 399 (1992), November, p. L71

[13] Chuang, K. J. ; Fedoseev, G. ; Ioppolo, S. ; van Dishoeck, E. F. ; Linnartz, H.: H-atom addition and abstraction reactions in mixed CO, H_2CO and CH_3OH ices - an extended view on complex organic molecule formation. En: *MNRAS* 455 (2016), Januar, Nr. 2, p. 1702–1712

[14] Chuang, K. J. ; Fedoseev, G. ; Qasim, D. ; Ioppolo, S. ; van Dishoeck, E. F. ; Linnartz, H.: Reactive Desorption of CO Hydrogenation Products under Cold Pre-stellar Core Conditions. En: *ApJ* 853 (2018), Februar, Nr. 2, p. 102

[15] Cordiner, M. A. ; Biver, N. ; Crovisier, J. ; Bockelée-Morvan, D. ; Mumma, M. J. ; Charnley, S. B. ; Villanueva, G. ; Paganini, L. ; Lis, D. C. ; Milam, S. N. ; Remijan, A. J. ; Coulson, I. M. ; Kuan, Y. J. ; Boissier, J.: Thermal Physics of the Inner Coma: ALMA Studies of the Methanol Distribution and Excitation in Comet C/2012 K1 (PanSTARRS). En: *ApJ* 837 (2017), März, Nr. 2, p. 177

[16] de Mijolla, D. ; Viti, S. ; Holdship, J. ; Manolopoulou, I. ; Yates, J.: Incorporating astrochemistry into molecular line modelling via emulation. En: *A&A* 630 (2019), Oktober, p. A117

[17] Drabek-Maunder, E. ; Greaves, J. ; Fraser, H. J. ; Clements, D. L. ; Alconcel, L. N.: Ground-based detection of a cloud of methanol from Enceladus: when is a biomarker not a biomarker? En: *International Journal of Astrobiology* 18 (2019), Februar, Nr. 1, p. 25–32

[18] Fedoseev, G. ; Chuang, K. J. ; van Dishoeck, E. F. ; Ioppolo, S. ; Linnartz, H.: Simultaneous hydrogenation and UV-photolysis experiments of NO in CO-rich interstellar ice analogues; linking HNCO, OCN^-, NH_2CHO, and NH_2OH. En: *MNRAS* 460 (2016), August, Nr. 4, p. 4297–4309

[19] Fiedler, Robert A. ; Mouschovias, Telemachos C.: Ambipolar Diffusion and Star Formation: Formation and Contraction of Axisymmetric Cloud Cores. I. Formulation of the Problem and Method of Solution. En: *ApJ* 391 (1992), Mai, p. 199

[20] Fiedler, Robert A. ; Mouschovias, Telemachos C.: Ambipolar Diffusion and Star Formation: Formation and Contraction of Axisymmetric Cloud Cores. II. Results. En: *ApJ* 415 (1993), Oktober, p. 680

[21] Flower, David ; Rabli, D. ; Pineau des Forêts, G.: Quantum mechanical and astrophysical studies of methanol. En: *European Physical Journal Web of Conferences* Vol. 34, 2012, p. 04001

[22] Fuchs, G. W. ; Cuppen, H. M. ; Ioppolo, S. ; Romanzin, C. ; Bisschop, S. E. ; Andersson, S. ; van Dishoeck, E. F. ; Linnartz, H.: Hydrogenation reactions in interstellar CO ice analogues. A combined experimental/theoretical approach. En: *A&A* 505 (2009), Oktober, Nr. 2, p. 629–639

[23] García-Burillo, S. ; Combes, F. ; Ramos Almeida, C. ; Usero, A. ; Alonso-Herrero, A. ; Hunt, L. K. ; Rouan, D. ; Aalto, S. ; Querejeta, M. ; Viti, S. ; van der Werf, P. P. ; Vives-Arias, H. ; Fuente, A. ; Colina, L. ; Martín-Pintado, J. ; Henkel, C. ; Martín, S. ; Krips, M. ; Gratadour, D. ; Neri, R. ; Tacconi, L. J.: ALMA images the many faces of the <ASTROBJ>NGC 1068</ASTROBJ>torus and its surroundings. En: *A&A* 632 (2019), Dezember, p. A61

[24] García-Burillo, S. ; Combes, F. ; Usero, A. ; Aalto, S. ; Krips, M. ; Viti, S. ; Alonso-Herrero, A. ; Hunt, L. K. ; Schinnerer, E. ; Baker, A. J. ; Boone, F. ; Casasola, V. ; Colina, L. ; Costagliola, F. ; Eckart, A. ; Fuente, A. ; Henkel, C. ; Labiano, A. ; Martín, S. ; Márquez, I. ; Muller, S. ; Planesas, P. ; Ramos Almeida, C. ; Spaans, M. ; Tacconi, L. J. ; van der Werf, P. P.: Molecular line emission in NGC 1068 imaged with ALMA. I. An AGN-driven outflow in the dense molecular gas. En: *A&A* 567 (2014), Juli, p. A125

[25] Garrod, R. T. ; Pauly, T.: On the Formation of CO_2 and Other Interstellar Ices. En: *ApJ* 735 (2011), Juli, Nr. 1, p. 15

[26] Garrod, Robin T. ; Widicus Weaver, Susanna L. ; Herbst, Eric: Complex Chemistry in Star-forming Regions: An Expanded Gas-Grain Warm-up Chemical Model. En: *ApJ* 682 (2008), Juli, Nr. 1, p. 283–302

[27] Geppert, W. D. ; Hamberg, M. ; Thomas, R. D. ; Österdahl, F. ; Hellberg, F. ; Zhaunerchyk, V. ; Ehlerding, A. ; Millar, T. J. ; Roberts, H. ; Semaniak, J. ; Ugglas, M. A. ; Källberg, A. ; Simonsson, A. ; Kaminska, M. ; Larsson, M.: Dissociative recombination of protonated methanol. En: *Faraday Discussions* 133 (2006), Januar, p. 177

[28] Geppert, W. D. ; Hellberg, F. ; Österdahl, F. ; Semaniak, J. ; Millar, T. J. ; Roberts, H. ; Thomas, R. D. ; Hamberg, M. ; Ugglas, M. A. ; Ehlerding, A. ; Zhaunerchyk, V. ; Kaminska, M. ; Larsson, M.: Dissociative Recombination

of CD 3 OD 2 +. En: Lis, Dariusz C. (Ed.) ; Blake, Geoffrey A. (Ed.) ; Herbst, Eric (Ed.): *Astrochemistry: Recent Successes and Current Challenges* Vol. 231, 2005, p. 117–124

[29] Grim, R. J. A. ; Baas, F. ; Geballe, T. R. ; Greenberg, J. M. ; Schutte, W. A.: Detection of solid methanol toward W 33A. En: *A&A* 243 (1991), März, p. 473

[30] Hasegawa, Tatsuhiko I. ; Herbst, Eric ; Leung, Chun M.: Models of Gas-Grain Chemistry in Dense Interstellar Clouds with Complex Organic Molecules. En: *ApJS* 82 (1992), September, p. 167

[31] Hastings, Janna ; Owen, Gareth ; Dekker, Adriano ; Ennis, Marcus ; Kale, Namrata ; Muthukrishnan, Venkatesh ; Turner, Steve ; Swainston, Neil ; Mendes, Pedro ; Steinbeck, Christoph: ChEBI in 2016: Improved services and an expanding collection of metabolites. En: *Nucleic acids research* 44 (2016), January, Nr. D1, p. D1214—9. – ISSN 0305–1048

[32] Heays, A. N. ; Bosman, A. D. ; van Dishoeck, E. F.: Photodissociation and photoionisation of atoms and molecules of astrophysical interest. En: *A&A* 602 (2017), Juni, p. A105

[33] Hernández-Hernández, Vicente ; Kurtz, Stan ; Kalenskii, Sergei ; Golysheva, Polina ; Garay, Guido ; Zapata, Luis ; Bergman, Per: APEX Millimeter Observations of Methanol Emission Toward High-mass Star-forming Cores. En: *AJ* 158 (2019), Juli, Nr. 1, p. 18

[34] Hidaka, H. ; Watanabe, M. ; Kouchi, A. ; Watanabe, N.: Reaction Routes in the CO-H_2CO-d_n -CH_3OH-d_m System Clarified from H(D) Exposure of Solid Formaldehyde at Low Temperatures. En: *ApJ* 702 (2009), September, Nr. 1, p. 291–300

[35] Hiraoka, Kenzo ; Ohashi, Nagayuki ; Kihara, Yosihide ; Yamamoto, Kazuyosi ; Sato, Tetsuya ; Yamashita, Akihiro: Formation of formaldehyde and methanol from the reactions of H atoms with solid CO at 10-20 K. En: *Chemical Physics Letters* 229 (1994), November, Nr. 4, p. 408–414

[36] Holdship, J. ; Viti, S. ; Jiménez-Serra, I. ; Makrymallis, A. ; Priestley, F.: UCLCHEM: A Gas-grain Chemical Code for Clouds, Cores, and C-Shocks. En: *AJ* 154 (2017), Juli, Nr. 1, p. 38

[37] Huang, K.-Y. ; Abbink, D. ; Viti, S. ; García-Burillo, S.: *Multi-transition study of methanol towards NGC 1068 with ALMA*. Submitted to the A&A Journal. Oktober 2023. – Manuscript submitted for publication

[38] Huang, K. Y. ; Viti, S. ; Holdship, J. ; García-Burillo, S. ; Kohno, K. ; Ta-

niguchi, A. ; Martn, S. ; Aladro, R. ; Fuente, A. ; Sánchez-García, M.: The chemical footprint of AGN feedback in the outflowing circumnuclear disk of NGC 1068. En: *A&A* 666 (2022), Oktober, p. A102

[39] Huang, Ko-Yun ; Viti, Serena: Tracing the chemical footprint of shocks in AGN-host and starburst galaxies with ALMA multi-line molecular studies. En: *Faraday Discussions* 245 (2023), September, p. 181–198

[40] James, T. A. ; Viti, S. ; Holdship, J. ; Jiménez-Serra, I.: Tracing shock type with chemical diagnostics. An application to L1157. En: *A&A* 634 (2020), Februar, p. A17

[41] Jiménez-Serra, I. ; Caselli, P. ; Martín-Pintado, J. ; Hartquist, T. W.: Parametrization of C-shocks. Evolution of the sputtering of grains. En: *A&A* 482 (2008), Mai, Nr. 2, p. 549–559

[42] Johnson, D. G. ; Blitz, M. A. ; Seakins, P. W.: The reaction of methylidene (CH) with methanol isotopomers. En: *Physical Chemistry Chemical Physics (Incorporating Faraday Transactions)* 2 (2000), Januar, Nr. 11, p. 2549–2553

[43] Kelly, G. ; Viti, S. ; García-Burillo, S. ; Fuente, A. ; Usero, A. ; Krips, M. ; Neri, R.: Molecular shock tracers in NGC 1068: SiO and HNCO. En: *A&A* 597 (2017), Januar, p. A11

[44] Kim, S. ; Chen, J. ; Cheng, T. ; Gindulyte, A. ; He, J. ; He, S. ; Li, Q. ; Shoemaker, B A. ; Thiessen, P A. ; Yu, B. ; Zaslavsky, L. ; Zhang, J. ; Bolton, E E.: PubChem 2023 update. En: *Nucleic Acids Res* 51 (2023), Nr. D1, p. D1373–D1380

[45] Kormendy, John ; Ho, Luis C.: Coevolution (Or Not) of Supermassive Black Holes and Host Galaxies. En: *Annual Review of Astron and Astrophys* 51 (2013), August, Nr. 1, p. 511–653

[46] Leurini, S. ; Codella, C. ; Gusdorf, A. ; Zapata, L. ; Gómez-Ruiz, A. ; Testi, L. ; Pillai, T.: Evidence of a SiO collimated outflow from a massive YSO in IRAS 17233-3606. En: *A&A* 554 (2013), Juni, p. A35

[47] Leurini, S. ; Gusdorf, A. ; Wyrowski, F. ; Codella, C. ; Csengeri, T. ; van der Tak, F. ; Beuther, H. ; Flower, D. R. ; Comito, C. ; Schilke, P.: Water emission from the high-mass star-forming region IRAS 17233-3606. En: *A&A* 564 (2014), April, p. L11

[48] Levine, I.N.: *Physical chemistry*. 6. New York : McGraw-Hill, 2009

[49] Li, Xiaolong ; Lu, Bo ; Wang, Lina ; Xue, Junfei ; Zhu, Bifeng ; Trabelsi, Tarek ; Francisco, Joseph S. ; Zeng, Xiaoqing: Unraveling sulfur chemistry in interstellar

carbon oxide ices. En: *Nature Communications* 13 (2022), November, p. 7150

[50] Linnartz, Harold ; Ioppolo, Sergio ; Fedoseev, Gleb: Atom addition reactions in interstellar ice analogues. En: *arXiv e-prints* (2015), Juli, p. arXiv:1507.02729

[51] Liszt, H. S. ; Pety, J. ; Lucas, R.: Limits on chemical complexity in diffuse clouds: search for CH_3OH and HC_5N absorption. En: *A&A* 486 (2008), August, Nr. 2, p. 493–496

[52] Luca, A. ; Voulot, D. ; Gerlich, D.: Low temperature reactions between stored ions and condensable gases: formation of protonated methanol via radiative association. En: *WDS'02 Proceedings of Contributed Papers, PART II* (2002), p. 294–300

[53] Mangum, Jeffrey G. ; Ginsburg, Adam G. ; Henkel, Christian ; Menten, Karl M. ; Aalto, Susanne ; van der Werf, Paul: Fire in the Heart: A Characterization of the High Kinetic Temperatures and Heating Sources in the Nucleus of NGC 253. En: *ApJ* 871 (2019), Februar, Nr. 2, p. 170

[54] Mathew, Thomas ; Esteves, Pierre M. ; Prakash, G. K. S.: Methanol in the RNA world: An astrochemical perspective. En: *Frontiers in Astronomy and Space Sciences* 9 (2022), August, p. 809928

[55] McCarthy, Tiege P. ; Ellingsen, Simon P. ; Chen, Xi ; Breen, Shari L. ; Voronkov, Maxim A. ; Qiao, Hai-hua: Detection of 36 GHz Class I Methanol Maser Emission toward NGC 4945. En: *ApJ* 846 (2017), September, Nr. 2, p. 156

[56] McElroy, D. ; Walsh, C. ; Markwick, A. J. ; Cordiner, M. A. ; Smith, K. ; Millar, T. J.: The UMIST database for astrochemistry 2012. En: *A&A* 550 (2013), Februar, p. A36

[57] Millar, T. J. ; Williams, D. A.: *Dust and Chemistry in Astronomy*. 1. Manchester : CRC, 2019

[58] Minissale, M. ; Dulieu, F. ; Cazaux, S. ; Hocuk, S.: Dust as interstellar catalyst. I. Quantifying the chemical desorption process. En: *A&A* 585 (2016), Januar, p. A24

[59] Morisset, S. ; Aguillon, F. ; Sizun, M. ; Sidis, V.: Wave-packet study of H_2 formation on a graphite surface through the Langmuir-Hinshelwood mechanism. En: *J. Chem. Phys.* 122 (2005), Mai, Nr. 19, p. 194702–194702

[60] Nakajima, T. ; Takano, S. ; Kohno, K. ; Harada, N. ; Herbst, E. ; Tamura, Y. ; Izumi, T. ; Taniguchi, A. ; Tosaki, T.: High-Resolution Imaging in 3-mm and 0.8-mm Bands and Abundances of Shock/Dust Related Molecules Toward the Seyfert Galaxy NGC 1068 Observed with ALMA. En: Iono, D. (Ed.) ; Tatematsu, K. (Ed.)

; Wootten, A. (Ed.) ; Testi, L. (Ed.): *Revolution in Astronomy with ALMA: The Third Year* Vol. 499, 2015, p. 109

[61] Nakajima, Taku ; Takano, Shuro ; Kohno, Kotaro ; Harada, Nanase ; Herbst, Eric: A molecular line survey toward the nearby galaxies NGC 1068, NGC 253, and IC 342 at 3 mm with the Nobeyama 45 m radio telescope: Impact of an AGN on 1 kpc scale molecular abundances. En: *PASJ* 70 (2018), Januar, Nr. 1, p. 7

[62] Nakamura, Fumitaka ; Hanawa, Tomoyuki ; Nakano, Takenori: Fragmentation of Filamentary Molecular Clouds with Longitudinal Magnetic Fields: Formation of Disks and Their Collapse. En: *ApJ* 444 (1995), Mai, p. 770

[63] NASA ; ESA ; Filippenko (UC Berkeley), Alex ; Sparks (STScI), William ; Ho (KIAA-PKU), Luis C. ; Malkan (UCLA), Matthew A. ; Capetti (STScI), Alessandro ; Pagan (STScI), Alyssa.: *Black-Hole-Driven Outflow From Active Galaxy NGC 1068. HUBBLESITE.* 2021. – Accessed on 18 November 2023

[64] National Center for Biotechnology Information: *PubChem Compound Summary for CID 887, Methanol*. https://pubchem.ncbi.nlm.nih.gov/compound/Methanol. 2024. – Retrieved January 22, 2024

[65] Peterson, Bradley M.: *An Introduction to Active Galactic Nuclei*. 1997

[66] Prasad, S. S. ; Huntress, Jr.: A model for gas phase chemistry in interstellar clouds: I. The basic model, library of chemical reactions, and chemistry among C, N, and O compounds. En: *ApJS* 43 (1980), Mai, p. 1–35

[67] Priestley, F. D. ; Viti, S. ; Williams, D. A.: An Efficient Method for Determining the Chemical Evolution of Gravitationally Collapsing Prestellar Cores. En: *AJ* 156 (2018), August, Nr. 2, p. 51

[68] Qasim, D. ; Chuang, K. J. ; Fedoseev, G. ; Ioppolo, S. ; Boogert, A. C. A. ; Linnartz, H.: Formation of interstellar methanol ice prior to the heavy CO freeze-out stage. En: *A&A* 612 (2018), April, p. A83

[69] Qiu, Jianjie ; Wang, Junzhi ; Shi, Yong ; Zhang, Jiangshui ; Fang, Min ; Li, Fei: Deep millimeter spectroscopy observations toward NGC 1068. En: *A&A* 613 (2018), Mai, p. A3

[70] Quénard, David ; Jiménez-Serra, Izaskun ; Viti, Serena ; Holdship, Jonathan ; Coutens, Audrey: Chemical modelling of complex organic molecules with peptide-like bonds in star-forming regions. En: *MNRAS* 474 (2018), Februar, Nr. 2, p. 2796–2812

[71] Roberge, W. G. ; Jones, D. ; Lepp, S. ; Dalgarno, A.: Interstellar Photodisso-

ciation and Photoionization Rates. En: *ApJS* 77 (1991), Oktober, p. 287

[72] Ruaud, M. ; Loison, J. C. ; Hickson, K. M. ; Gratier, P. ; Hersant, F. ; Wakelam, V.: Modelling complex organic molecules in dense regions: Eley-Rideal and complex induced reaction. En: *MNRAS* 447 (2015), März, Nr. 4, p. 4004–4017

[73] Ruaud, Maxime ; Wakelam, Valentine ; Hersant, Franck: Gas and grain chemical composition in cold cores as predicted by the Nautilus three-phase model. En: *MNRAS* 459 (2016), Juli, Nr. 4, p. 3756–3767

[74] Sánchez-García, M. ; García-Burillo, S. ; Pereira-Santaella, M. ; Colina, L. ; Usero, A. ; Querejeta, M. ; Alonso-Herrero, A. ; Fuente, A.: Spatially resolved star-formation relations of dense molecular gas in NGC 1068. En: *A&A* 660 (2022), April, p. A83

[75] Santos, Julia C. ; Chuang, Ko-Ju ; Lamberts, Thanja ; Fedoseev, Gleb ; Ioppolo, Sergio ; Linnartz, Harold: First Experimental Confirmation of the $CH_3O + H_2CO \rightarrow CH_3OH + HCO$ Reaction: Expanding the CH_3OH Formation Mechanism in Interstellar Ices. En: *ApJL* 931 (2022), Juni, Nr. 2, p. L33

[76] Schinnerer, E. ; Eckart, A. ; Tacconi, L. J. ; Genzel, R. ; Downes, D.: Bars and Warps Traced by the Molecular Gas in the Seyfert 2 Galaxy NGC 1068. En: *ApJ* 533 (2000), April, Nr. 2, p. 850–868

[77] Scourfield, M. ; Viti, S. ; García-Burillo, S. ; Saintonge, A. ; Combes, F. ; Fuente, A. ; Henkel, C. ; Alonso-Herrero, A. ; Harada, N. ; Takano, S. ; Nakajima, T. ; Martín, S. ; Krips, M. ; van der Werf, P. P. ; Aalto, S. ; Usero, A. ; Kohno, K.: ALMA observations of CS in NGC 1068: chemistry and excitation. En: *MNRAS* 496 (2020), August, Nr. 4, p. 5308–5329

[78] Simons, M. A. J. ; Lamberts, T. ; Cuppen, H. M.: Formation of COMs through CO hydrogenation on interstellar grains. En: *A&A* 634 (2020), Februar, p. A52

[79] Smith, D. ; Adams, N. G.: Binary and ternary reactions of CH_3^+ ions with several molecules at thermal energies. En: *Chemical Physics Letters* 54 (1978), Januar, p. 535–540

[80] Smith, David ; Spanel, Patrik ; Mayhew, Christhopher A.: A selected ion-flow tube study of the reactions of O+, H+ and HeH]+ with several molecular gases at 300 K. En: *International Journal of Mass Spectrometry and Ion Processes* 117 (1992), September, p. 457–473

[81] Smith, I.W.M. ; Cockell, C.S. ; Leach, S.: *Astrochemistry and Astrobiology*. 1. Berlin Heidelberg : Springer, 2013

[82] Smith, Lucas R. ; Gudipati, Murthy S. ; Smith, Rachel L. ; Lewis, Robert D.: Isotope effect on the sublimation curves and binding energies of ^{12}CO and ^{13}CO interstellar ice analogues. En: *A&A* 656 (2021), Dezember, p. A82

[83] Sung Lee, Hack ; Drucker, Mark ; Adams, Nigel G.: Thermal energy reactions of H+3 and H3O+ with a series of small organic molecules. En: *International Journal of Mass Spectrometry and Ion Processes* 117 (1992), September, p. 101–114

[84] Takano, Shuro ; Nakajima, Taku ; Kohno, Kotaro ; Harada, Nanase ; Herbst, Eric ; Tamura, Yoichi ; Izumi, Takuma ; Taniguchi, Akio ; Tosaki, Tomoka: Distributions of molecules in the circumnuclear disk and surrounding starburst ring in the Seyfert galaxy NGC 1068 observed with ALMA. En: *PASJ* 66 (2014), Juli, Nr. 4, p. 75

[85] Tanner, S. D. ; Mackay, G. I. ; Hopkinson, A. C. ; Bohme, D. K.: Proton transfer reactions of HCO+ at 298 K. En: *International Journal of Mass Spectrometry and Ion Processes* 29 (1979), Februar, Nr. 2, p. 153–169

[86] Tielens, A.: *The Physics and Chemistry of the Interstellar Medium*. 1. Cambridge : Cambridge University Press, 2005

[87] Tielens, A. G. G. M. ; Hagen, W.: Model calculations of the molecular composition of interstellar grain mantles. En: *A&A* 114 (1982), Oktober, Nr. 2, p. 245–260

[88] Tosaki, Tomoka ; Kohno, Kotaro ; Harada, Nanase ; Tanaka, Kunihiko ; Egusa, Fumi ; Izumi, Takuma ; Takano, Shuro ; Nakajima, Taku ; Taniguchi, Akio ; Tamura, Yoichi: A statistical study of giant molecular clouds traced by ^{13}CO, C^{18}O, CS, and CH_3OH in the disk of NGC 1068 based on ALMA observations. En: *PASJ* 69 (2017), April, Nr. 2, p. 18

[89] Turner, B. E.: The Physics and Chemistry of Small Translucent Molecular Clouds. XI. Methanol. En: *ApJ* 501 (1998), Juli, Nr. 2, p. 731–748

[90] van der Tak, F. F. S. ; Black, J. H. ; Schöier, F. L. ; Jansen, D. J. ; van Dishoeck, E. F.: A computer program for fast non-LTE analysis of interstellar line spectra. With diagnostic plots to interpret observed line intensity ratios. En: *A&A* 468 (2007), Juni, Nr. 2, p. 627–635

[91] van Dishoeck, E. F. ; Kristensen, L. E. ; Benz, A. O. ; Bergin, E. A. ; Caselli, P. ; Cernicharo, J. ; Herpin, F. ; Hogerheijde, M. R. ; Johnstone, D. ; Liseau, R. ; Nisini, B. ; Shipman, R. ; Tafalla, M. ; van der Tak, F. ; Wyrowski, F. ; Aikawa, Y. ; Bachiller, R. ; Baudry, A. ; Benedettini, M. ; Bjerkeli, P. ; Blake, G. A. ; Bontemps, S. ; Braine, J. ; Brinch, C. ; Bruderer, S. ; Chavarría, L. ; Codella, C. ; Daniel, F. ; de Graauw, Th. ; Deul, E. ; di

Giorgio, A. M. ; Dominik, C. ; Doty, S. D. ; Dubernet, M. L. ; Encrenaz, P. ; Feuchtgruber, H. ; Fich, M. ; Frieswijk, W. ; Fuente, A. ; Giannini, T. ; Goicoechea, J. R. ; Helmich, F. P. ; Herczeg, G. J. ; Jacq, T. ; Jørgensen, J. K. ; Karska, A. ; Kaufman, M. J. ; Keto, E. ; Larsson, B. ; Lefloch, B. ; Lis, D. ; Marseille, M. ; McCoey, C. ; Melnick, G. ; Neufeld, D. ; Olberg, M. ; Pagani, L. ; Panić, O. ; Parise, B. ; Pearson, J. C. ; Plume, R. ; Risacher, C. ; Salter, D. ; Santiago-García, J. ; Saraceno, P. ; Stäuber, P. ; van Kempen, T. A. ; Visser, R. ; Viti, S. ; Walmsley, M. ; Wampfler, S. F. ; Yildiz, U. A.: Water in Star-forming Regions with the Herschel Space Observatory (WISH). I. Overview of Key Program and First Results. En: *PASP* 123 (2011), Februar, Nr. 900, p. 138

[92] van Dishoeck, Ewine F. ; Jonkheid, Bastiaan ; van Hemert, Marc C.: Photoprocesses in protoplanetary disks. En: *Faraday Discussions* 133 (2006), Januar, p. 231

[93] Viti, S. ; García-Burillo, S. ; Fuente, A. ; Hunt, L. K. ; Usero, A. ; Henkel, C. ; Eckart, A. ; Martin, S. ; Spaans, M. ; Muller, S. ; Combes, F. ; Krips, M. ; Schinnerer, E. ; Casasola, V. ; Costagliola, F. ; Marquez, I. ; Planesas, P. ; van der Werf, P. P. ; Aalto, S. ; Baker, A. J. ; Boone, F. ; Tacconi, L. J.: Molecular line emission in NGC 1068 imaged with ALMA. II. The chemistry of the dense molecular gas. En: *A&A* 570 (2014), Oktober, p. A28

[94] Viti, Serena ; Collings, Mark P. ; Dever, John W. ; McCoustra, Martin R. S. ; Williams, David A.: Evaporation of ices near massive stars: models based on laboratory temperature programmed desorption data. En: *MNRAS* 354 (2004), November, Nr. 4, p. 1141–1145

[95] Wakelam, V. ; Herbst, E. ; Loison, J. C. ; Smith, I. W. M. ; Chandrasekaran, V. ; Pavone, B. ; Adams, N. G. ; Bacchus-Montabonel, M. C. ; Bergeat, A. ; Béroff, K. ; Bierbaum, V. M. ; Chabot, M. ; Dalgarno, A. ; van Dishoeck, E. F. ; Faure, A. ; Geppert, W. D. ; Gerlich, D. ; Galli, D. ; Hébrard, E. ; Hersant, F. ; Hickson, K. M. ; Honvault, P. ; Klippenstein, S. J. ; Le Picard, S. ; Nyman, G. ; Pernot, P. ; Schlemmer, S. ; Selsis, F. ; Sims, I. R. ; Talbi, D. ; Tennyson, J. ; Troe, J. ; Wester, R. ; Wiesenfeld, L.: A KInetic Database for Astrochemistry (KIDA). En: *ApJS* 199 (2012), März, Nr. 1, p. 21

[96] Wakelam, V. ; Smith, I. W. M. ; Herbst, E. ; Troe, J. ; Geppert, W. ; Linnartz, H. ; Öberg, K. ; Roueff, E. ; Agúndez, M. ; Pernot, P. ; Cuppen, H. M. ; Loison, J. C. ; Talbi, D.: Reaction Networks for Interstellar Chemical Modelling: Improvements and Challenges. En: *Space Science Reviews* 156 (2010), Oktober, Nr. 1-4, p. 13–72

[97] Walsh, Catherine ; Loomis, Ryan A. ; Öberg, Karin I. ; Kama, Mihkel ; van 't Hoff, Merel L. R. ; Millar, Tom J. ; Aikawa, Yuri ; Herbst, Eric ; Widicus

Weaver, Susanna L. ; Nomura, Hideko: First Detection of Gas-phase Methanol in a Protoplanetary Disk. En: *ApJL* 823 (2016), Mai, Nr. 1, p. L10

[98] Wang, Junzhi ; Zhang, Jiangshui ; Gao, Yu ; Zhang, Zhi-Yu ; Li, Di ; Fang, Min ; Shi, Yong: SiO and CH_3OH mega-masers in NGC 1068. En: *Nature Communications* 5 (2014), November, p. 5449

[99] Watanabe, Naoki ; Kouchi, Akira: Efficient Formation of Formaldehyde and Methanol by the Addition of Hydrogen Atoms to CO in H_2O-CO Ice at 10 K. En: *ApJL* 571 (2002), Juni, Nr. 2, p. L173–L176

[100] Watanabe, Naoki ; Nagaoka, Akihiro ; Shiraki, Takahiro ; Kouchi, Akira: Hydrogenation of CO on Pure Solid CO and CO-H_2O Mixed Ice. En: *ApJ* 616 (2004), November, Nr. 1, p. 638–642

[101] Williams, D.A. ; Hartquist, T.W. ; Rawlings, J.M.C. ; Cecchi-Pestellini, C. ; Viti, S.: *Dynamical Astrochemistry*. 1. London : Royal Society of Chemistry, 2018

[102] Wirström, E. S. ; Geppert, W. D. ; Hjalmarson, Å. ; Persson, C. M. ; Black, J. H. ; Bergman, P. ; Millar, T. J. ; Hamberg, M. ; Vigren, E.: Observational tests of interstellar methanol formation. En: *A&A* 533 (2011), September, p. A24

[103] Woods, Paul M. ; Slater, Ben ; Raza, Zamaan ; Viti, Serena ; Brown, Wendy A. ; Burke, Daren J.: Glycolaldehyde Formation via the Dimerization of the Formyl Radical. En: *ApJ* 777 (2013), November, Nr. 2, p. 90

[104] Yamamoto, Satoshi: *Introduction to Astrochemistry: Chemical Evolution from Interstellar Clouds to Star and Planet Formation*. 1. Japan : Springer Tokyo, 2017